A Robust Model for Integration of Sand-Arch Stability and Fractal Wormhole Network in CHOPS and post-CHOPS Process Simulation

by

Yadong Qin

A thesis submitted in partial fulfillment of the requirements for the degree of

Doctor of Philosophy

In

PETROLEUM ENGINEERING

Department of Civil and Environmental Engineering
University of Alberta

ABSTRACT

Cold heavy-oil production with sand (CHOPS) is a primary recovery process in unconsolidated heavy-oil reservoirs. The recovery factor typically ranges from 5% to 15% of the initial oil in place (OOIP). Approximately 90% of crude oil is left underground with considerable exploitation potential after the CHOPS process. Existing CHOPS simulation models capture many of the key characteristics of CHOPS mechanisms, including foamy oil flow, growth of the wormhole network, and sand production. However, the simulation models are only tested based on the performance of a single CHOPS well; their ability to represent a variety of CHOPS production profiles is rarely examined. This thesis addresses this issue. It provides an improved CHOPS simulation model that is tested against several CHOPS wells with different production profiles. This expands the range of CHOPS wells that can be represented with this improved CHOPS simulation model. As a result, a wider range of reservoir conditions at the end of CHOPS is simulated, enhancing the set of initial conditions available for simulating subsequent post-CHOPS processes.

An improved set of initial conditions for simulating the performance of potential post-CHOPS recovery technologies, such as cyclic solvent processes, would enable the effect of these conditions to be examined in more detail. For example, the impact of the wormhole network distribution on the uncertainties in post-CHOPS performance could be quantified more readily. This thesis extends the CHOPS simulation model developed in a previous study (Yu and Leung, 2020), incorporating dynamic fractal wormhole growth, sand production, and multi-component foamy oil flow. Appropriate modifications have been made to this model to ensure that the simulated production performance, including the oil and sand production profiles, bottom-hole

pressure (BHP), and producing gas-oil ratio (GOR), is reasonable and sufficiently flexible to capture a wide range of CHOPS production profiles.

A field case study was carried out to examine the effectiveness of this improved CHOPS simulation model to capture a variety of CHOPS production profiles. Three CHOPS wells from Dee Valley with different production profiles were simulated. This involved the detailed examination of the relevant model parameters for improved matching against field data, including incorporating a representation of the wormhole network growth rate and density that depended on the oil and sand production profiles. This included the incorporation of different fractal patterns to represent different wormhole network characteristics. As well, the sand production model in the study by Yu and Leung (2020) was adjusted to capture the characteristics typical of the entire sand production profile from CHOPS wells: i.e., a rapid increase in the rate of sand production to a peak, and subsequent decline to a low but persistent level. Similarly, the foamy oil model in the study by Yu and Leung (2020) was refined in order to capture the characteristics typical of gas production from CHOPS wells: a period of relatively low but constant producing GOR followed by a sharp increase in producing GOR as a well ages.

Simulations of a promising post-CHOPS technology, cyclic solvent injection (CSI), were carried out to study the performance of this recovery technology to enhance heavy oil recovery after the CHOPS process. The reservoir conditions at the end of CHOPS from several wells in the CHOPS simulation studies were used to determine the initial conditions for the CSI simulations. For these simulations, pure CO_2 was selected as the solvent to repressurize the reservoir and stimulate further oil production. The simulations explored various mechanisms involved in the dissolution of CO_2 into heavy oil during injection and exsolution of CO_2 from heavy oil during production. In particular, these simulations focused on the nonequilibrium aspects of CO_2

dissolution and exsolution. The simulation results indicated that foamy oil flow (in the form of dispersed bubbles) is beneficial to oil production.

PREFACE

This thesis is an original work by Yadong Qin. Parts of the research work have been submitted or are ready for journal submission.

Chapters 1 and 2 contain original material that has not been published previously.

Chapters 3 and 4 summarize the basic methodologies, materials and model setups from chapters 5 to 7.

Chapter 5 has been submitted for a publication as Qin, Y., Leung, J. Y. and Sawatzky, R. P. A Robust Model for Integration of Sand-Arch Stability and Fractal Wormhole Network in Cold Heavy-Oil Production with Sand (CHOPS) Simulation. I was responsible for the data collection, methodology, and analysis, validation, visualization, and manuscript composition. Leung, J. Y. and Sawatzky, R. P. were the supervisory authors involved in conceptualization, analysis, and manuscript composition.

Chapter 6 will be submitted for a publication as Qin, Y., Leung, J. Y. and Sawatzky, R. P. Integrating Sand-Arch Stability and Fractal Wormhole Network in Cold Heavy-Oil Production with Sand (CHOPS) – A Field Case Study. I was responsible for the data collection, methodology, and analysis, validation, visualization, and manuscript composition. Leung, J. Y. and Sawatzky, R. P. were the supervisory authors involved in conceptualization, analysis, and manuscript composition.

Chapter 7 will be submitted for a publication as Qin, Y., Leung, J. Y. and Sawatzky, R. P. Field-Scale Simulation of Pure CO2 Injection in Cyclic Solvent Injection (CSI) to Enhance Heavy Oil Recovery during Post-CHOPS Process. I was responsible for the data collection, methodology, and analysis, validation, visualization, and manuscript composition. Leung, J. Y. and Sawatzky, R. P. were the supervisory authors involved in conceptualization, analysis, and manuscript composition.

DEDICATION

I dedicate this thesis to my loving family for their endless support and encouragement.

ACKNOWLEDGEMENT

First and foremost, I would like to express my deepest gratitude to my supervisors, Dr. Juliana Y. Leung and Dr. Ronald P. Sawatzky, whose guidance, expertise, and unwavering support were instrumental throughout this research journey. Their mentorship has been invaluable, and I am truly fortunate to have had the opportunity to work under their supervision. I also thank my supervisory and examining committee, Dr. Andy Li, Dr. Apostolos Kantzas and Dr. Japan Trivedi, for attending to my final defense and for their insightful comments regarding my thesis.

I want to thank all my colleagues of Dr. Leung's research group for the stimulating discussions. Most importantly, I want to express my gratitude to my partner Ran and my dear friends for their understanding, company, help and support.

I want to acknowledge my family for their boundless love, support, and understanding. Their patience during my absence and your encouragement during challenging times have been my pillars of strength.

Last but not least, I am profoundly grateful to the China Scholarship Council for their financial support, which has made my academic journey possible. I am deeply appreciative to the University of Alberta for granting access to the Numerical and Statistical Server, and to the Computer Modelling Group Ltd. for the academic license.

TABLE OF CONTENTS

LIST OF TABLES

LIST OF FIGURES

LIST OF SYMBOLS

A & B	=	Non-negative coefficients for division factor
A_{fp}	=	Area of fractal pattern occupied in the disc
$A_{wh}(n)$	=	Area of the wormhole network covered at time step n
$B(x, r_x)$	=	Closed disc of radius r_x and center x
c	=	Kozeny constant
C	=	Concentration of solvent in each phase
C_u	=	Unconfined compressive strength of sand
C_{vi}	=	Initial concentration of solid sand in the void space of a wormhole cell
C_{vn}	=	Solid sand concentration in the void space of a wormhole cell at time step n
d	=	Box-counting dimension
D	=	Dispersion
D_{fp}	=	Density of fractal pattern
D_{ivn}	=	Time-varying division factor
$D_{wh}(n)$	=	Density of wormhole network at time step n
D_{mij}	=	Molecular diffusion coefficient of component i in phase j
exp	=	Positive constant exponent
F	=	Area containing fractals
J_{ijk}	=	Dispersion flux of component i in phase j in direction k
K_{CH4}	=	K-value determining solubility of $CH4s$ in oleic phase
K_{CO2}	=	K-value determining solubility of $CO2s$ in oleic phase
k_i	=	Initial permeability in a wormhole cell
k_n	=	Permeability in a wormhole cell at time step n
k_o	=	Oleic phase permeability
K_{v1}	=	First coefficient in correlation for K_{CH4}
K_{v2}	=	Second coefficient in correlation for K_{CH4}
K_{v3}	=	Third coefficient in correlation for K_{CH4}
K_{v4}	=	Fourth coefficient in correlation for K_{CH4}
K_{v5}	=	Fifth coefficient in correlation for K_{CH4}
N	=	Number of particles in a fractal pattern generated by the DLA model

N_o = Concentration of oleic phase in the void space of a grid block

N_{dbn} = Concentration of *Dispersed Bubble* in oleic phase at time step *n*

N_{fgn} = Concentration of *Free Gas* in gaseous phase at time step *n*

N_{msn} = Concentration of *Mobile Sand* in oleic phase in a wormhole cell at time step *n*

N_{CH4sn} = Concentration of *CH4s* in oleic phase at time step *n*

N_{CO2sn} = Concentration of *CO2s* in oleic phase at time step *n*

N_{CO2gn} = Concentration of *CO2g* in gaseous phase at time step *n*

$N_{CO2bubn}$ = Concentration of *CO2bub* in oleic phase at time step *n*

$N_\varepsilon(F)$ = Number of self-similar structures *F* at scale ε

q_{crit} = Critical oil flow rate

R = Sources or sinks of solvent injected

r_{ms} = Constant factor in pseudo kinetic model for rate of sand mobilization

R_c = Average radius of curvature for the sand arch at the wormhole tip

r_o = Radius of the disc occupied by fractal pattern

$r_o\,(n)$ = Distance between the wellbore and the farthest wormhole cell at time step *n*

r_x = Radius of closed disc

r_{CH4b} = Constant factor in pseudo kinetic model for rate of methane nucleation

r_{CH4g} = Constant factor in pseudo kinetic model for rate of methane coalescence

r_{CH4s} = Constant factor in pseudo kinetic model for rate of methane dissolution

r_{CO2b} = Constant factor in pseudo kinetic model for rate of CO_2 nucleation

r_{CO2g} = Constant factor in pseudo kinetic model for rate of CO_2 coalescence

r_{CO2s} = Constant factor in pseudo kinetic model for rate of CO_2 dissolution

S_j = Saturation of phase *j*

S_{on} = Oil saturation at time step *n*

t = Time

T = Temperature

u = Interstitial velocity of a phase

$|u_j|$ = Magnitude of interstitial velocity of phase *j*

v_n = Oleic phase Darcy velocity at time step *n*

v_{crit} = Critical oleic phase Darcy velocity for sand arch failure at the wormhole tip

v_{eln} = Velocity-dependent factor

v_{ref} = Reference Darcy velocity

x = Center of closed disc

x_i = Mole fraction of component *i* in oleic phase

x'_{in} = Equilibrium mole fraction of component *i* in oleic phase at time step *n*

x_{dbn} = Mole fraction of *Dispersed Bubble* in oleic phase at time step *n*

x_{msn} = Mole fraction of *Mobile Sand* in the oleic phase at time step *n*

x_{sgn} = Mole fraction of *Solution Gas* in oleic phase in oleic phase at time step *n*

x_{CH4bn} = Mole fraction of *CH4b* in oleic phase in oleic phase at time step *n*

x_{CH4sn} = Mole fraction of *CH4s* in oleic phase in oleic phase at time step *n*

x'_{CH4sn} = Equilibrium mole fraction of *CH4s* in oleic phase at time step *n*

x_{CO2bn} = Mole fraction of *CO2b* in oleic phase in oleic phase at time step *n*

x_{CO2sn} = Mole fraction of *CO2s* in oleic phase in oleic phase at time step *n*

x'_{CO2sn} = Equilibrium mole fraction of *CO2s* in oleic phase at time step *n*

y'_{CH4gn} = Equilibrium mole fraction of *CH4g* in gaseous phase at time step *n*

y'_{CO2gn} = Equilibrium mole fraction of $CO2g$ in gaseous phase at time step *n*

dp/dr = Pressure gradient at the wormhole tip

$(dp/dr)_{cr}$ = Critical pressure gradient for sand arch failure at the wormhole tip

dr/dt = Rate of advance of the wormhole tip

∇C = Concentration gradient of component *i* in each direction

$\nabla_k C_{ij}$ = Concentration gradient of component *i* in phase *j* in direction *k*

Greek letters:

α_{ij} = Dispersivity coefficient for phase *j* in direction *k*

τ_{jk} = Tortuosity for phase *j* in direction *k*

ε = Small scale of a self-similar structure

μ_i = Pseudo viscosity of oleic component *i*

μ_o = Viscosity of oleic phase

ρ_c = Molar density of solid

ρ_{on} = Molar density of the oleic phase at time step *n*

φ_f = Fluid porosity

φ_{fi} = Initial fluid porosity

φ_{fn} = Fluid porosity at time step n

φ_v = Void porosity, maximum porosity in a wormhole cell

Acronyms:

BHP = Bottom-hole pressure

CHOPS = Cold heavy-oil production with sand

CMG = Computer Modelling Group

CSI = Cyclic solvent injection

CSS = Cyclic steam stimulation

DLA = Diffusion-Limited Aggregation

EOR = Enhance oil recovery

EOS = Equation of state

GOR = Gas-oil ratio

MRC = More rapid coalescence

MW = Molecular weight

NMR = Nuclear magnetic resonance

OOIP = Initial oil in place

PAW = Probabilistic active walker

PCP = Progressing cavity pump

PVT = Pressure-Volume-Temperature

rrf = Reaction frequency factor

SAGD = Steam-assisted gravity drainage

CHAPTER 1: INTRODUCTION

1.1 Background

Heavy oil reservoirs constitute a substantial portion of hydrocarbon reserves, comprising approximately 70% of the world's total oil resources, estimated at 9 to 13 trillion barrels (Shafiei and Dusseault, 2013). Heavy oil has been defined as any liquid petroleum with an API gravity less than 20° (Dusseault, 2001). Significant heavy-oil deposits are reported in western Canada. Some 80% of heavy oil in place is found in sands less than 5 m thick in the Lloydminster area (Adams, 1982) of central Alberta and Saskatchewan. Thermal methods such as steam flooding, steam-assisted gravity drainage (SAGD) and cyclic steam stimulation (CSS) are the most widely-adopted recovery methods used in heavy oil reservoirs. However, those thermal methods can cause formation damage and are not efficient in some thin reservoirs due to excessive heat loss to the over- or under-burden. Fortunately, many of these reservoirs are also weakly consolidated, and they can be operated under primary recovery with sand production (i.e., cold heavy oil production with sands or CHOPS). Cold heavy-oil production with sand (CHOPS) has become the recovery technology of choice for most heavy oil fields surrounding Lloydminster. It emerged as a viable commercial technology in the mid to late 1980s and was widely adopted by the mid-1990s (Sawatzky et al., 2002).

In the late 1920s, operators learned empirically that wells with sustainable sand production tended to perform the way better (a 10-fold increase in heavy oil production), and sand exclusion with screens led to loss of oil production in the Lloydminster area (Smith, 1988; Loughead and Saltuklaroglu, 1992). The sharp oil price increases in the 1970s and 1980s led to great interest in heavy-oil resources (Bowers and Drummond, 1997). Latest sand exclusion technologies were

introduced, resulting in greatly impaired productivity. In the 1980s, the development of progressive cavity pumps (PCP) that could handle a great amount of sand to be produced along with oil flow changed the nonthermal heavy-oil industry in Canada. This groundbreaking technology guided the maturation of the CHOPS process implemented in western Canada.

The recovery factor at the end of the CHOPS process typically ranges from 5% to 15% of the initial oil in place, with the average of 10%. Two primary physical mechanisms in the CHOPS process include sand production and foamy oil flow. Sand production leading to cavities or wormholes characterized by high-porosity and high-permeability channels are created around the wellbore and extend into the reservoir as a network (Huang et al. 1998; Tremblay 2005). Efforts to incorporate these two fundamental principles into numerical simulation models represent an unwavering pursuit among researchers.

At the end of CHOPS, there is approximately 90% of crude oil is left underground with considerable exploitation potential. A suitable post-CHOPS method is desired to enhance the heavy oil recovery. The traditional waterflooding method would result in early breakthrough and associated bypassing of the remaining oil in the reservoir due to the presence of high-conductivity wormhole network developed in CHOPS process (Chen and Leung, 2021). By contrary, the CSI process can benefit from the presence of the high-conductivity wormhole network that provides access for solvent injection to the reservoir and a larger contact area for solvent dissolution into the oleic phase (Chang and Ivory, 2013; Chen and Leung, 2021). Steam-based processes are uneconomic in thinner formations due to significant heat loss to the over- or under-burden and require thermally completed wells (Coskuner and Huang, 2020a). Solvent-assisted processes, such as cyclic solvent injection (CSI), is often recommended as a follow-up or "post-CHOPS" strategy to increase the ultimate recovery (Dusseault 2002; Chang & Ivory 2013).

1.2 Problem Statement

Increasing the representativeness of future forecasts and narrowing the uncertainties in post-CHOPS render the development of improved and reliable CHOPS model necessary. To build a robust simulation model to describe the CHOPS process and apply it to the post-CHOPS process, characteristics of CHOPS, containing sand production, high-conductivity channels and foamy oil behaviour, should be incorporated into one workflow. Yu and Leung (2020) proposed a novel dynamic wormhole growth model by integrating statistical fractal patterns with realistic sand-arch stability constraints and pressure depletion due to fluid flows, which successfully solved the integration problem.

However, the proposed model by Yu and Leung (2020) cannot obtain a reasonable BHP variation and producing GOR. Besides, a calibration of the proposed model against a range of field histories, including the historical sand rate, is lacking. Appropriate modifications to the proposed model proposed by Yu and Leung (2020) for a further robust and comprehensive model is desired. Foamy oil model is key to be adjusted for a reasonable producing GOR, which holds the significance in the CHOPS process. Parameters in the sand production model should be tuned for a calibration against the field data. The improved model is aiming at increasing the reliability of future forecasts and narrow the uncertainties for the post-CHOPS process.

The second problem is to analyze the effect of anisotropic pressure distribution on wormhole growth. Since the fractal pattern is a 2D formation generated by the DLA model, to investigate the effect of vertical pressure gradient on wormhole growth, the existing model needs to be extended to 3D. The wormhole is inclined to grow in the direction with the weakest cohesive strength or the highest pressure gradient. In western Canada, the depth of most CHOPS reservoirs

is generally greater than 350m, in which the vertical stress is much stronger than horizontal stress. The effect of vertical stress on wormhole growth is thus generally ignored.

The third challenge is to further investigate the robustness and enhance the modelling flexibility of the improved model for simulating a variety of production and flow behaviours associated with CHOPS wells. Aiming to capture different characteristics from different CHOPS wells, parameters in foamy oil model, sand production model and relative permeability system hold the importance to calibrate against the field data. Considerations of fractal patterns for wormholes propagation are taken based on different historical oil and sand production.

The last challenge is to employ the model to the post-CHOPS process for uncertainties quantifying. A cyclic solvent injection (CSI) is generally addressed as a strategy to exploit reservoirs following the CHOPS process. The foamy oil behaviour should be reproduced during CSI process. The foamy oil model needs to be built as several new components are added based on the solvent selection. Wherein, the rate of non-equilibrium processes, such as dissolution, nucleation and coalescence, is key to simulate for a representative oil production forecast. Solvents mixing with oil including dissolution, dispersion and diffusion should be modeled reasonably. In addition, wormholes would stop propagating in post-CHOPS, such that wormhole growth model would be removed. An appropriate and improved CHOPS model can thus be provided for a field-scale CSI simulation.

1.3 Research Objectives

(1) Develop an improved model based on the model proposed by Yu and Leung (2020). Analyze the reasonability of BHP and producing GOR variations. Effectively calibrate against the field data, including oil and sand rates.

(2) Extend the current wormhole network system to 3D to analyze the effects of anisotropic pressure distribution on wormhole growth. The wormhole is inclined to grow in the direction with the weakest cohesive strength or the highest pressure gradient. The method to simulate a 3D system is through a stack of 2D wormhole patterns.

(3) Address sensitivity tests of domain size to reduce computational efforts. It has been observed in the model proposed by Yu and Leung (2020) that pressure depletion is relatively modest beyond the outer envelope of the wormhole network. To reduce the simulation time but allow for finer horizontal grid blocks, the computational domain in the horizontal plane is chosen to be smaller.

(4) Complete the history matching works by the proposed CHOPS model with various production and flow behaviours to further investigate the robustness and enhance the modelling flexibility of the improved model. Corresponding parameters need to be further optimized during the validation process to capture the behaviours of specified wells.

(5) Conduct post-CHOPS process with the initial conditions built at the end of the CHOPS process. Develop kinetic models that can simulate the solvent nonequilibrium behavious, including dissolution and exsolution processes. It is generally believed that the wormhole structure keeps stable in post-CHOPS. Thus, the existing wormhole growth model should be removed in the post-CHOPS process.

(6) Provide insights in parameter selections associated with nonequilibrium processes (solvent dissolution and exsolution) to reproduce the foamy oil flow in the CSI process.

(7) Formulate an improved CHOPS model to scale up solvent-assisted post-CHOPS processes in complex fractal wormhole configurations and quantify the recovery uncertainty.

1.4 Thesis Structure

There are 8 chapters in this thesis that is organized as follows:

Chapter 1 presents a general introduction of this thesis including background, problem statement, research objectives and the thesis structure.

Chapter 2 presents the literature review for the CHOPS and CSI processes.

Chapter 3 introduces the primary methodologies used in this research, including the model development for the CHOPS process and CSI.

Chapter 4 summarizes the important materials, production histories and reservoir settings in this research. A total of four CHOPS wells are modelled, one from Cold Lake and other three from Dee Valley.

Chapter 5 describes appropriate modifications made to the proposed model (Yu and Leung, 2020) to ensure that the simulated production performance, including the oil production profile, BHP, GOR, and sand production, is reasonable.

Chapter 6 presents a further validation for the robustness and the effectiveness of the improved model in Chapter 5 by three CHOPS single wells from Dee Valley with a variety of production and flow behaviours.

Chapter 7 presents a representative forecast for the CSI process following history matching works completed in Chapter 6. Pure CO_2 is selected as the solvent injected into the reservoir. The key parameters in the CSI process are investigated to provide insights in the numerical simulation of the CSI process.

Chapter 8 summarizes the contributions and conclusions of this thesis. The limitations and future works are also discussed in this chapter.

CHAPTER 2: LITERATURE REVIEW

2.1 Mechanisms of the CHOPS Process

Sand is produced during CHOPS because no sand exclusion process is used in the wellbore; in fact, sand is deliberately produced along with liquid to enhance the recovery. As much as a 10-fold increase in heavy oil production rates has been reported after removing sand exclusion devices in the well (Smith, 1988; Loughead and Saltuklaroglu, 1992). As mentioned earlier, the development of progressive cavity pumps (PCP) that could handle a great amount of sand (up to 60-70% sand by weight) to be produced along with oil flow was a critical factor in the improvement of CHOPS (Walin et al., 2000). Although it is possible to maintain limited oil production with small amounts of sand ingress using a reciprocating pump in a vertical or deviated well, the problem of slow rod fall means that production rates are usually limited to no more than 8-12 m^3/day. PCP technology allows rates as high as 25-30 m^3/day, and exceptionally 50 m^3/day for some time in the best wells (Dusseault and El-Sayed, 2000).

Producing sand in order to increase oil rates renders the completion approach and the production equipment challenging to allow successful sand management. Generally, large-diameter (generally 1 in.) entry ports are created for well perforations, enabling sand ingress into the wellbore (McCaffrey and Bowman, 1991; Dusseault and El-Sayed, 2000; Dusseault et al., 2002). To implement CHOPS technology in the Taobao oilfield in Jilin, China, Dusseault et al. (2002) used large PCP, large aperture (i.e., perforation diameter with 25 mm) and high-density perforations (30/2 m) to recomplete old wells and complete newly drilled wells. However, as noted by Wang et al. (2005), the sand and other solid materials (e.g., shale) flowing into the wellbore with crude oil may cause the PC to become clogged, or otherwise get stuck in the wellbore,

requiring frequent workovers. In the study by Wang et al. (2005), a completion strategy was put forward by limiting sand influx, using a screen liner to inhibit 0.5 mm or larger sands flowing into the wellbore. To solve the same issues, Guo et al. (2012) developed a mathematical model to predict the critical oil-production rate required for cleaning sand in the well during CHOPS. In a different approach, cavity-like completions were reported by Palmer et al. (2000) in weak sands. Aiming to increase the productivity of a well, small cavities could be deliberately created around perforations by means of jetting or others. The study by Walin et al. (2000) identifies a number of workover strategies that were tested in Lloydminster-area heavy oil reservoirs to mitigate problems induced by sand production. Some worked.

Cavities or wormholes characterized by high-porosity and high-permeability channels are created around the wellbore and extend into the reservoir as a network, representing one of the main recovery mechanisms (Huang et al. 1998; Tremblay 2005). Previous studies have demonstrated the presence of horizontal wormholes through tracer tests in the field and laboratory experiments (Squires, 1993; Yeung, 1995; Tremblay et al., 1998; Liu and Zhao, 2005). Two steps involved in sand production, failure and fluidization, are the key factors contributing to the growth or propagation of the wormhole network. Sand arch failure occurs when the pressure gradient at the tip of an existing wormhole exceeds a certain threshold, causing the sand grains to detach from the matrix. This is followed by sand fluidization, in that sand flows as a plug together with the heavy oil and other reservoir fluids from the wormhole tip along the network and into the wellbore (Tremblay et al., 1997; Yuan et al., 1999; Sawatzky et al., 2002; Dusseault and El-Sayed, 2000). At the late stage, if the open channel is developed at the top of wormholes, settled sand beneath the channel may be scoured and dragged by heavy oil to the wellbore (Yuan et al., 1999).

Another important physical mechanism is foamy oil flow. The term "foamy oil" originated from observations of stable foams in samples collected at the wellhead from many Canadian and Venezuelan heavy-oil wells produced under solution-gas drive (Maini, 2001). Smith (1988) was the first to analyze the flow behaviour under solution gas drive in CHOPS. The process of gas exsolution involves bubble nucleation and coalescence to a free gas phase when the pressure declines below the bubble point. The high viscosity of the heavy oil postpones the formation of a connected free gas phase and the associated thermodynamical equilibrium state, resulting in gas bubbles being dispersed in the oleic phase (Sheng et al., 1999; Maini, 2001; Lillico et al., 2001; Uddin, 2005; Chen and Maini, 2005; Liu et al., 2016). This behaviour is regarded as a non-equilibrium phenomenon and can be represented by a kinetic model. It is generally accepted that the foamy oil flow behaviour is a complex function of pressure depletion rate, fluid properties, and time (Smith, 1988; Maini, 1996; Kumar et al., 2002). Delaying free gas flow leads to a relatively low producing GOR during the early stage of CHOPS and a gradual increase in producing GOR over the life of the well.

2.2 CHOPS Model

The challenge of CHOPS simulation is the proper incorporation or coupling of all relevant physical mechanisms: a reasonable wormhole network representation that captures the branching characteristics; a dynamic wormhole growth model that captures the tip propagation behaviour; foamy oil flow (i.e., non-equilibrium gas exsolution); and, sand production (failure and fluidization).

Many existing models employ a simplified representation of the wormhole network. Generally, the network structure is horizontal in these models given the field and laboratory observations about wormholes noted in the 2.1. Istchenko and Gates (2012; 2014) modelled the

wormhole network as an extension of the wellbore. Others adopted a similar idea by enhancing the near-wellbore region's permeability to mimic the wormhole network's increased flow capacity (Lebel, 1994; Sawatzky et al., 2002; Rivero et al., 2010). A partial dual-porosity model generally used for modelling fractured reservoirs has also been developed (Rangriz Shokri and Babadagli, 2012a; 2012b). Other methods conceptualize the wormhole network as a fractal pattern.

Yuan et al. (1999) proposed a probabilistic active walker (PAW) model, while Liu and Zhao (2005) used the Diffusion-Limited Aggregation (DLA) model to generate the fractal patterns. In both studies, the wormhole growth is assumed to be uniform in all (horizontal) directions without explicitly considering the asymmetric growth of individual wormhole tips using the sand arch failure criterion. More recent studies, including Fan et al. (2016; 2019) and Yu and Leung (2020), incorporated the sand arch failure criterion to model the dynamic wormhole growth. However, Fan et al. (2016; 2019) did not consider any realizations of branching networks to describe the wormhole network. Yu and Leung (2020) presented a new model integrating statistical fractal patterns with realistic sand arch stability constraints.

2.3 Techniques of Post-CHOPS

As a follow-up to CHOPS, the traditional waterflooding method would result in early breakthrough and associated bypassing of the remaining oil in the reservoir due to the presence of high-conductivity wormhole network developed in the CHOPS process (Chen and Leung, 2021). By contrast, the cyclic solvent injection (CSI) process can benefit from the presence of the high-conductivity wormhole network that provides access for solvent injection to the reservoir and a larger contact area for solvent dissolution into the oleic phase (Chang and Ivory, 2013; Chen and Leung, 2021).

Additionally, steam-based processes are uneconomic in thinner formations due to significant heat loss to the underburden and overburden and require thermally completed wells (Coskuner and Huang, 2020a). The CSI is applicable for thin pays in Lloydminster and can be used in existing non-thermally completed CHOPS wells (Coskuner and Huang, 2020b). Moreover, the CSI process is more environmentally friendly than steam injection methods (e.g., steam-assisted gravity drainage or SAGD and cyclic steam stimulation or CSS) because of no water usage and lower energy requirement.

The typical CSI process is also known as solvent huff-n-puff process, which comprises of an injection cycle, a soaking period and a production cycle (Lim et al., 1996; Dong et al., 2006; Ivory et al., 2010; Jamaloei et al., 2012; Jiang et al., 2013). A solvent or a solvent mixture is injected to the reservoir to re-pressurize the reservoir to the initial reservoir pressure (Coskuner and Huang, 2020b), dissolved into the heavy oil to reduce its viscosity, and exsolved from oil to stimulate and activate the foamy oil drive (Alshmakhy and Maini, 2012) during the pressure depletion process (i.e. the well is put on production). The solvent composition is normally selected to suit the reservoir so that the solvent or solvent mixture is slightly above its dewpoint at the end of injection periods. This is because the solvent in gas form can readily help to pressurize the reservoir and transport in porous medium more efficiently than liquid form (Chang and Ivory, 2013; Coskuner and Huang, 2020b).

2.4 Solvent Selection in the CSI Process

Methane (CH_4), propane (C_3H_8) and carbon dioxide (CO_2) are commonly selected as solvents injected solely or mixed and then injected into the reservoir in the CSI process. In this study, pure CO_2 is selected for the CSI process to enhance oil recovery. The reasons for this decision are described in more detail in Chapter 7.

Many experimental efforts have been made to evaluate the performance of CO_2 compared with other solvents. Bjorndalen et al. (2012) examined the supersaturation of different solvents (CH_4, C_3H_8, and CO_2) during pressure depletion in an etched glass micromodel and suggested that CO_2 saturated oil produces more nucleation sites than CH_4, C_3H_8 and a mixture of CO_2 and C_3H_8, as well as a longer period of persistent supersaturation. With more nucleation sites, more small bubbles are entrained in the oil and persist there, enhancing the recovery of oil under solution gas drive. Furthermore, Bryan et al. (2018) demonstrated that CO_2-saturated heavy oil is less viscous than CH_4-saturated heavy oil, as measured by nuclear magnetic resonance (NMR), since the solubility of CO_2 in heavy oil is significantly greater than the solubility of CH_4 in heavy oil. Although propane is more soluble in heavy oil than CO_2, leading to a greater viscosity reduction, the foamy oil generated by CO_2 is more stable than foamy oil generated by propane (Chen et al., 2020). Therefore, propane is not necessarily a better solvent for CSI than CO_2. Bjorndalen et al. (2023) presented a suite of experiments comparing the performance of CO_2, propane, and a CO_2-propane mixture. These solvents were injected into both dead and live heavy oil sand packs at a constant pressure and temperature. The result implied that propane was dissolved into the live oil more slowly than into dead oil, whereas CO_2 showed a faster rate of uptake in live oil than in dead oil. This indicated that methane interferes with propane sorption into live oil.

In a comprehensive study, Bamzad et al. (2023) experimentally measured solubility, liquid viscosity, liquid density and *K*-values for different solvents (methane, CO_2 and mixtures of these two) in a heavy oil. They investigated these properties over a wide range of temperature (80.65, 129.42, 179.14, and 230.45 °C) and pressure (1,600, 3,100, 4,100, and 5,100 kPa). The experimental results demonstrated that CO_2 showed a greater reduction in bitumen viscosity and an increased solubility compared with methane. However, the range of temperatures Bamzad et al.

(2023) used in their study is well above the temperature in Lloydminster heavy oil reservoirs (approximately 20–25 °C). Ma et al. (2017) measured the PVT properties, including viscosity, of $CH_4/CO_2/C_3H_8$-saturated heavy oils at different equilibrium pressures and a temperature of 21 °C. The heavy oil samples came from the Colony Formation in the Bonnyville area of eastern Alberta, Canada. The dead oil properties are shown in Table 2.1. The experimental results for CH_4-saturated heavy oil and CO_2-saturated heavy oil are shown in Table 2.2 and Table 2.3. As indicated in the tables, the CO_2-saturated heavy oil showed a significantly greater solubility and a greater reduction in viscosity than CH_4-saturated heavy oil. Moreover, Bryan et al. (2018) measured the solubility and viscosity of CH_4/CO_2-saturated heavy oil at 1,600 kPag and 25 °C. They reported that as the composition of CO_2 in the solvent mixture increases, the solubility of the solvent in the heavy oil also increases, and the live oil exhibits a greater reduction in viscosity.

	Density (g/cm^3)	Viscosity (mPa·s)	*MW (g/mole)
Dead oil	0.992	33,876	547.7

Table 2.1 Properties of dead oil in the study by Ma et al. (2017). *MW = molecular weight.

Pressure (kPa)	Solubility (g/100g heavy oil)	Density (g/cm^3)	Viscosity (mPa·s)	Swelling Factor
1007.181	0.264	0.98857	23,533	1.00791
2028.159	0.441	0.98734	18,057	1.00982
3026.142	0.617	0.98512	11,771	1.01430
4014.927	0.793	0.98389	9,407	1.01792

Table 2.2 PVT data for heavy oil saturated methane in the study by Ma et al. (2017).

Pressure (kPa)	Solubility (g/100g heavy oil)	Density (g/cm^3)	Viscosity (mPa·s)	Swelling Factor
1050.372	1.762	0.99163	14,728	1.02076
2100.744	4.449	0.99246	4,901	1.04065
3045.492	6.960	0.99229	1,042	1.07083
3955.032	8.899	0.98610	554	1.10187
4946.724	11.013	0.98593	266	1.12090

Table 2.3 PVT data for heavy oil saturated CO_2 in the study by Ma et al. (2017).

Many sand pack experiments have been conducted to investigate the performance of CO_2 in enhancing heavy oil recovery during CSI processes. Cyclic injection of pure CO_2 was experimentally investigated in a horizontal core with two viscous oils (Shi et al., 2008). The recovery was increased by 10-14% after primary production when CO_2 injection was introduced. Alberta Innovates–Technology Futures (AITF) conducted an experiment in which a 28 vol% C_3H_8 and 72 vol% CO_2 solvent mixture was injected in a large depleted sand pack model with no wormholes (Ivory et al., 2010). The oil recovery after primary production and six solvent cycles was 50.4% of OOIP. The experimental results were history-matched, so that they could be expanded (via field-scale simulations) to predict the performance of the same solvent mixture under post-CHOPS field conditions (Chang and Ivory, 2013). Other studies (Alshmakhy and Maini, 2012; Or et al., 2014; Zhou et al., 2018; Zhou et al., 2019) also reported that CO_2-based solvent mixtures exhibited good performance in enhancing heavy oil recovery in sand packs or core experiments.

2.5 CSI Pilot Tests by Using CO_2

Operator companies such as Husky and Nexen have carried out a few field CSI pilot tests in western Canada and these pilots were reviewed by Coskuner and Huang (2020b). Two pilots

related to CO_2 injection have been tested by Husky at Mervin and Lashburn (Husky Energy, 2011; Coskuner and Huang, 2020b).

The Mervin EOR pilot has three separate reservoirs, one behaving like a single-well pool in the Colony formation. In this pool, the total solvent volume of 100% CO_2 injected was 2,499,000 m^3 in a period of five months, allowed to soak for three months and produced for 11 months. The final production in the first cycle achieved 1,751 m^3, which accounted for 14% of the primary recovery, and the solvent recovery factor was 84.5%. The second cycle in the same well included 14% propane injected, but produced only 10% of the primary recovery. In this case, the addition of small amounts of propane did not improve the CSI performance with only CO_2. Therefore, Husky used only CO_2 in the following three cycles. At the time the paper was published (Coskuner and Huang, 2020b), cumulative oil production from this well has reached 37% of the primary recovery.

The other Colony well performed very well under primary recovery with 51,000 m^3 of cumulative oil produced. The first CSI cycle produced 60% of its primary recovery in the ~ 3 years of production. Similarly, a Waseca well with good performance under primary recovery also performed well in the CSI process with only CO_2 injection. Three cycles of CO_2 injection in Lashburn showed that the oil production rate in the Waseca pool reached peak rates similar to those under primary production. Coskuner and Huang (2020b) stated that the cyclic CO_2 injection process should be able to double primary oil production after seven cycles have been completed. The Husky pilot tests demonstrated that CO_2 injection could be applied as a promising method in CSI to enhance heavy oil recovery.

CHAPTER 3: METHODOLOGY

This research is based on a previous study by Yu and Leung (2020). Therefore, similarities are inevitably taken in this research and the previous study (Yu and Leung, 2020), e.g., the basic workflow. This chapter introduces primary methodologies, including the model development for CHOPS and CSI processes.

3.1 Model Development for CHOPS Processes

During the CHOPS process, physical mechanisms including a reasonable wormhole network representation that captures the branching characteristics, a dynamic wormhole growth model that captures the tip propagation behaviour, foamy oil flow (i.e., non-equilibrium gas exsolution), and sand production (failure and fluidization) need to be adequately taken in numerical simulations. The workflow built by Yu and Leung (2020) is adopted in this research.

3.1.1 Dynamic Fractal Wormhole Growth Workflow

This work extends the methodology previously presented by Yu and Leung (2020). The workflow integrates a sand arch failure and fluidization model and a fractal-based wormhole network growth algorithm. The overall workflow is implemented in MATLAB® (The MathWorks 2019b), with a thermal three-phase multi-component flow simulator STARS® (Computer Modelling Group 2018) serving as the platform for the flow simulations. The structure of the workflow is shown schematically in Figure 3.1.

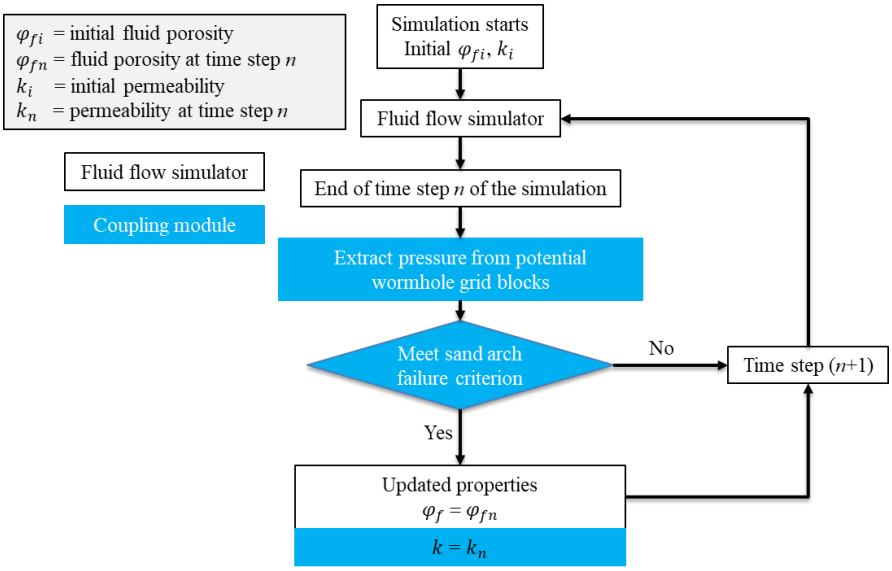

Figure 3.1 Flow chart for the dynamic wormhole growth workflow.

A summary of the workflow is provided here. A 2D fractal pattern for the potential wormhole network is constructed using the well position as the seed location, and it is subsequently superimposed on the simulation mesh for a single horizontal layer within the simulation grid. At the start of the simulation, wormhole properties are assigned to those near-well grid blocks that are part of the fractal pattern. These are the initial active wormhole cells. The remainder of the fractal pattern prescribes the wormhole network's potential (or future) growth paths. The wormhole network grows dynamically by coupling the three-phase multi-component flow simulation with a sand arch failure criterion: each wormhole in the network continues propagating along the prescribed fractal pattern only if the pressure gradient at its tip (i.e., the pressure gradient into the outermost active wormhole cell for each strand in the network) exceeds a threshold specified in the sand arch failure criterion. An explicit coupling scheme is adopted: at the end of each time step, the flow simulation is paused temporarily, and the pressure gradient at the tip of each existing wormhole is computed. If the sand arch failure criterion is met at a given wormhole tip, that wormhole tip will continue to grow along the direction prescribed by the fractal pattern at that

location by advancing one grid block; i.e., the adjacent potential wormhole cell in the fractal pattern is activated to become a wormhole cell. Otherwise, this tip does not grow. The properties of each new active wormhole cell (i.e., the effective porosity φ_{fn} and the permeability k_n) are updated according to the sand fluidization model. Following this procedure for updating the wormhole network, the flow simulation continues by advancing another time step with the updated wormhole network.

3.1.2 DLA Algorithm and Effective Wormhole Cells

A DLA model proposed by Liu and Zhao (2005) is used to create the statistical fractal patterns. In this study, the CHOPS process is simulated with a single well model. However, the approach described here could be extended straightforwardly to handle a multi-well case. The fractal pattern starts from the well at the model's geometrical center, and extends outward from this point in several directions. Figure 3.2 shows a realization of the 2D fractal wormhole pattern used in this chapter. This pattern provides a representation of the trajectory that the wormhole network could take in a simulation. Cells (i.e., grid blocks) that are not part of this pattern cannot be activated to become wormhole cells. In the computational mesh, this principle is implemented by digitizing the fractal pattern into a map of binary indices: cells with a value of "1" are potential wormhole cells, while cells with a value of "0" are part of the matrix. Each potential wormhole cell has a dimension of 0.5 m × 0.5 m. A coarser background mesh of 2.5 m × 2.5 m is used for the matrix cells, to reduce the computational costs. However, this mesh is refined locally (0.5 m × 0.5 m) in regions surrounding the potential wormhole cells. This is shown in Figure 3.3, noting that these images are icons, and are not intended to match the fractal pattern.

Note that with this approach not all potential wormhole cells necessarily become active wormhole cells. A given potential wormhole cell will only become activated if an adjacent

"downstream" wormhole cell becomes activated during the course of the simulation, and if the sand arch failure criterion between the potential wormhole cell and the activated wormhole cell is met later in the simulation (usually the failure criterion is met either at the next time step or not at all). This process is akin to a sequence of falling dominoes.

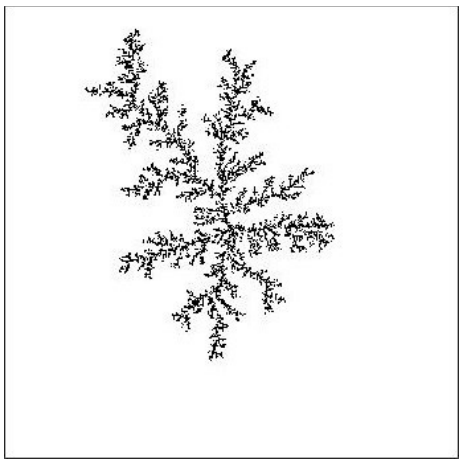

Figure 3.2 The fractal pattern used in Chapter 5.

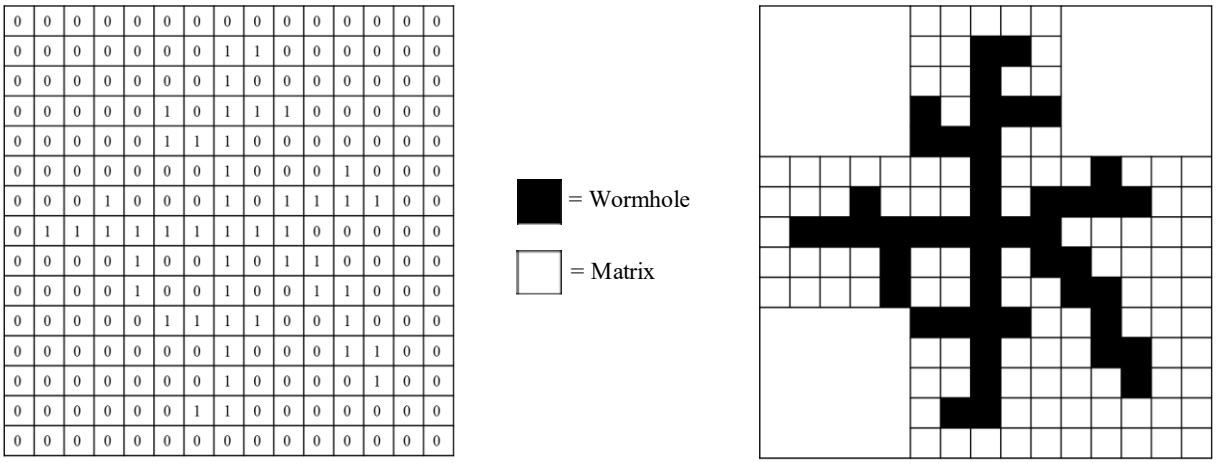

Figure 3.3 (a): Binary representation of a wormhole network (each potential wormhole cell has a dimension of 0.5 m × 0.5 m). (b): Mesh for the flow simulation (note the local grid refinement around the wormhole cells).

Several remarks regarding the physical conditions in wormholes, and how these conditions are represented in the simulated wormhole cells, are warranted here. The internal structure of wormholes has been investigated extensively in a series of laboratory experiments by Tremblay

and colleagues (Tremblay et al., 1997; 1998; Tremblay and Oldakowski, 2002; 2003). In summary, their studies have shown that a wormhole is a stable horizontal tube contained within a compacted sand matrix, growing from its tip longitudinally into the compacted sand. In cross-section (i.e., the cross-section perpendicular to the axis of the tube), it consists of a central region of loose sand surrounded by a relatively narrow annular region of concentric tensile failure bands. The sand does not move in the tensile failure bands, only in the central region containing loose sand. The sand and reservoir fluids (i.e., oil, water, gas) are transported downstream from the failed region just behind the tip along the length of the wormhole toward the well. Initially, while the rate of sand influx into the wormhole is relatively large compared with the rate of heavy oil influx, the central region in the wormhole is filled completely with loose sand. The loose sand flows as a plug together with the heavy oil and other reservoir fluids. Subsequently, the situation often becomes reversed. Over time, the rate of sand influx into the wormhole has a tendency to become relatively small compared with the rate of heavy oil influx, in which case there is a strong likelihood for the heavy oil to erode an open channel at the top of the central region containing loose sand. If this happens, a portion of the loose sand bed below the open channel continues to flow but at a reduced rate compared with the flow of heavy oil in the open channel. As well, unless the heavy oil flow rate in the open channel is sufficiently large, there will also be a layer of sand at the bottom of the sand bed that stops moving altogether.

This picture of the internal structure of wormholes, with their two possible sand-filled states (i.e., completely filled or partially filled with loose sand) as developed by Tremblay, is supported by a range of field evidence from CHOPS developments, both published and anecdotal. The pattern of sand production in CHOPS wells, with very high sand cuts (the ratio of the volume of produced sand to the volume of produced oil) initially, followed by a rapid decline to a low but

persistent sand cut is consistent with the transition in the internal structure of a wormhole described above (Sawatzky et al., 2002). Further, there is considerable evidence that adjacent CHOPS wells can be in communication; i.e., that fluids in one well can be transported to an adjacent well so rapidly that there must be one or more open channels connecting them (Tremblay et al., 1999; Squires, 1993).

However, neither the evidence from laboratory studies or field observations can shed much light on the distribution of the two sand-filled states for all of the wormholes in the wormhole network. Not all adjacent CHOPS wells are in communication with each other (Squires, 1993). Even when adjacent wells are in communication, this does not imply that all the wormholes in the network have an open channel throughout their length; it only implies that at least one wormhole does. Moreover, a given wormhole in the network is not necessarily maintained in one sand-filled state or the other throughout its entire length during the course of the CHOPS process. To be sure, during early stages of CHOPS when the wormhole network is growing relatively rapidly it is likely that all of the wormholes are in a completely sand-filled state, given the relatively large change in volume that occurs when an element of compacted sand is converted to loose sand. However, as the wormhole network begins to grow more slowly, local conditions of heavy oil influx into the network may cause open channels to develop in some of the wormholes (Yuan et al., 1999). It has been conjectured that open channels would develop first at the tips of slowly growing wormholes and subsequently propagate downstream along them toward the well (Yuan et al., 1999), but no information from field observations has been brought forward to provide any confirmation of this point. Further, as to the questions of how fast, how far, and in how many wormholes does this open channel condition propagate, there have been no answers.

The uncertainty in the sand-filled state of an individual wormhole, at any position in the wormhole network and at any time during the evolution of the wormhole network during the course of the CHOPS process, translates directly to uncertainty in the physical properties of each wormhole as a function of position and time; specifically to uncertainty in the porosity and permeability. For wormholes completely filled with loose sand, the results of the series of experiments by Tremblay and colleagues indicate that the porosity tends to be approximately 50% on average, with a relatively small variation of about $\pm$ 3% (Tremblay et al., 1997; 1998; Tremblay and Oldakowski, 2002; 2003). When the wormholes develop open channels, the porosity will depend on the degree of scouring (Yuan et al., 1999); as the size of the open channel increases, so too will the porosity until it reaches 100% if/when the bed of loose sand is removed completely from the wormhole.

There is a similar contrast between the permeability of wormholes completely filled with sand and wormholes containing an open channel. Tremblay estimated the effective permeability to oil in a wormhole completely filled with sand flowing as a plug to be on the order of 2,000 Darcies or more (Tremblay et al., 1997; Yuan et al., 1999). However, once an open channel develops in a wormhole, the effective permeability to oil will be at least three orders of magnitude larger; laminar flow theory predicts that the permeability of a channel with a diameter of 1 cm will be on the order of several million Darcies.

Finally, in addition to the uncertainty in the porosity and effective permeability in an individual wormhole, there is the issue of the wormhole diameter. There is considerable uncertainty in this physical property too. In the series of experiments performed by Tremblay and colleagues, wormholes were generated with diameters ranging from about 5 cm to 20 cm; as the diameter of the experimental cell containing the compacted sand pack increased, so too did the

diameter of the wormholes that were generated. This dependence of the diameter of a wormhole on the size of the drainage volume around the wormhole tip lead Tremblay to postulate that in the field the diameter of individual wormholes could be very much greater than 20 cm (Tremblay and Oldakowski, 2002). However, given the considerable evidence from the results of laboratory experiments and observations of field behaviour that wormholes usually remain stable after they have been generated (Sawatzky et al., 2002), the requirement that wormholes remain stable presents a constraint to the potential diameter of individual wormholes under field conditions. Considerations of the stability of a cylindrical cavity in a compacted oil sand under the forces of gravity and seepage imply that the diameters of wormholes in the field are not likely to be much more than 40-50 cm, and quite possibly considerably less than this (Wong et al., 1994).

Given the large uncertainty in the physical properties (i.e., porosity, permeability and diameter) of individual wormholes at any position in the wormhole network and at any time during the growth of the wormhole network, and modelling constraints imposed by the structure of the flow simulator, several simplifying assumptions are made to represent the physical properties of the wormholes in the network. The key assumption is that what is designated as a wormhole cell (i.e., a potential wormhole cell that has been activated) essentially is an upscaled grid block containing a wormhole. So it should be considered as an effective wormhole cell. This removes the issue of representing the wormhole diameter explicitly in the model. Note that in this thesis, the term wormhole refers to the central region containing loose sand while the surrounding tensile failure bands are treated as part of the intact sand matrix. This is consistent with the approach taken in Tremblay and Oldakowski (2002; 2003).

Further, there is no attempt in the simulation model presented here to represent the other physical properties (i.e., porosity, permeability) of wormholes in both sand-filled states. Rather, a

blended approach is taken in which the porosity and permeability in the activated wormhole cells are based on the levels reported by Tremblay, as noted above, for wormholes that are completely filled with sand. In particular, the choice of an effective permeability to oil in the activated wormhole cells that is on the order of thousands of Darcies, rather than millions of Darcies, is consistent with the approach taken in previous simulation studies (Lebel, 1994; Sawatzky, et al., 2002). Note that the porosity and permeability in these wormhole cells are allowed to increase dynamically during the course of a simulation, to accommodate the effects of sand transport along the wormhole network on these properties. A detailed description of the model used to calculate the dynamic changes in porosity and permeability in the wormhole cells is presented in Section 3.1.5 below. The parameters in this model can be tuned, as necessary, in the simulation model to improve its match to field production performance.

3.1.3 Dimension and Density Measurements of Fractals

The fractal dimension describes the ability of a set to fill the Euclidean space in which it resides, and it is the quantitative description of the fractal characteristics of the investigated objects (Xu et al., 1993; Falconer, 2004). It is usually understood as the classical box-counting dimension that is given by (Falconer, 2004; Fernández-Martínez, 2016):

$$d = \lim_{\varepsilon \to 0} \frac{\log N_\varepsilon(F)}{-\log \varepsilon}, \qquad 3\text{-}1$$

where d is the box-counting dimension; ε relates to different scales of a fractal structure and $N_\varepsilon(F)$ represents the number of self-similar structures F at scale ε. In this thesis, the fractal patterns are generated using an in-house DLA algorithm implemented in MATLAB (Martinez Gamboa and Leung, 2019). A 2-dimensional Euclidean plane is the foundation of fractals composed of small

particles of a specific size. The ε thus can be viewed as the linear size ratio of the particle to the 2-D box in each spatial direction, and Eq. 3-1 can be simplified as:

$$d = \frac{\log N}{-\log \varepsilon}, \tag{3-2}$$

where N is the number of particles in a fractal pattern generated by the DLA model.

The density of a fractal could be explained as the concentration of fractals about typical points or local densities and the directional distribution of fractals around points (Falconer, 2004). Therefore, the density of a fractal pattern at point x is:

$$\lim_{r_x \to 0} \frac{area(F \cap B(x, r_x))}{area(B(x, r_x))} = \lim_{r_x \to 0} \frac{area(F \cap B(x, r_x))}{\pi r_x^2}, \tag{3-3}$$

where F is the area containing fractals and $B(x, r_x)$ is the closed disc of radius r_x and center x. In this thesis, point x is located in the geometrical center of the reservoir domain as the origin and seed of the fractal pattern. The disc $B(x, r_x)$ changes over r_x to measure the density variation away from the center of the domain. Besides, the disc is bounded by the box containing the fractal pattern. The dimensionless fractal density D_{fp} can be defined as:

$$D_{fp} = \frac{A_{fp}}{\pi r_o^2}, \tag{3-4}$$

where A_{fp} is the area of fractal pattern occupied in the disc with a certain radius r_o away from the origin (in m^2), which is the location of the wellbore; it is measured by the summation of the area of all particles within the distance r_o. The fractal pattern generated by the DLA model is composed of identical particles.

Wormholes dynamically propagate along the fractal pattern as a designated path. The density of a wormhole network is determined at different times during the CHOPS process, given by:

$$D_{wh}(n) = \frac{A_{wh}(n)}{\pi(r_o(n))^2}, \quad 3\text{-}5$$

where $D_{wh}(n)$ is the dimensionless density of wormhole network at time step n; $r_o(n)$is the distance between the wellbore and the farthest wormhole cell at time step n (in m) and $A_{wh}(n)$ is the area of the wormhole network covered with the radius $r_o(n)$ at time step n (in m^2). Eq. 3-5 can be used to plot the density of the wormhole network over time or radius.

3.1.4 Sand Arch Failure Criterion and Wormhole Propagation Rate

The mechanisms underlying the failure of an unconsolidated sand matrix adjacent to an open perforation in a well bore were described in detail, and quantitatively, by Bratli and Risnes (1981). Resistance to failure is provided by the presence of a hemispherical arch that forms in the (initially) undisturbed sand matrix surrounding the perforation. Obviously, the arch will fail if the force exerted on it is greater than the arch's resistance to failure. In the analysis by Bratli and Risnes (1981), based on an idealized model of the geomechanical conditions, the predominant destabilizing force exerted on the arch is caused by the fluid flow (i.e., seepage) through it; i.e., by the drag force exerted by the flowing fluids on the sand grains in the arch (Yuan et al., 1999). Thus, the destabilizing force exerted on the arch is proportional to the fluid pressure gradient across it. If this force exceeds a critical threshold, the sand will fail, first in shear and then in tension according to the analysis of Bratli and Risnes (1981). Following tensile failure, the sand in the arch will be fluidized. This analysis leads directly to a sand arch failure criterion that is defined by a critical pressure gradient $(dp/dr)_{cr}$. This critical pressure gradient can be represented as

$$(dp/dr)_{cr} = 2C_u/R_c, \qquad 3\text{-}6$$

where C_u is the unconfined compressive strength of the sand arch after it has yielded (i.e., failed in shear) and R_c is the average radius of curvature of the sand arch. It is interesting to note that the critical pressure gradient is independent of the far-field stresses. This would not be so if the shear strength of the sand arch was not exceeded prior to tensile failure and fluidization (Wong et al., 1994).

Following failure and fluidization of the arch in the sand around a perforation, a new arch will form adjacent to it. This arch will fail too, if the local pressure gradient across it exceeds the critical pressure gradient. And so on. Thus, a cylindrical wormhole will form, emanating from the perforation and extending into the reservoir, with an arch in the (as yet to be) undisturbed sand matrix at its hemispherical tip. This depiction of the conditions required for sand arch failure at the tip of a wormhole, based solely on theoretical considerations, is supported by the results of a series of laboratory experiments conducted by Tremblay and colleagues (Tremblay et al., 1997; 1998; Tremblay and Oldakowski, 2002; 2003; Sawatzky et al., 2002). It is clear from these experiments that a criterion for wormhole growth (i.e., failure of the arch in the sand matrix at the tip of the wormhole) can be constructed solely in terms of a critical pressure gradient.

Eq. 3-6 is not used directly in the simulation model for CHOPS presented here. There are two reasons for this. The first is the uncertainty in the value of the unconfined compressive strength of the sand arch C_u in Eq. 3-6. Typically, sand strength in unconsolidated oil-saturated sands is measured on samples that are prepared to represent, as much as possible, an intact sand matrix under reservoir conditions, not on sand samples that have yielded. Therefore, the value of C_u that should be used in Eq. 3-6 is likely much lower than the values for C_u that are generally reported

in the literature. In the experiments reported by Tremblay and Oldakowski (2002; 2003), it is inferred from estimates of the critical pressure gradient required for the onset of massive sand production that the effective value of C_u that should be employed in Eq. 3-6 is approximately two to ten times smaller than the value of C_u measured on intact sand samples. The heterogeneity that exists in reservoir sands, even unconsolidated ones, will only exacerbate the uncertainty in the appropriate value for C_u to use in Eq. 3-6.

The second reason that it is difficult to use Eq. 3-6 directly in a simulation model for CHOPS is the considerable uncertainty in the wormhole diameter, as articulated in Section 3.1.2. Obviously, the radius of curvature R_c at the tip of a wormhole is determined directly by the diameter/radius of the wormhole.

Given the uncertainty in both of the parameters that appear in Eq. 3-6, an alternative approach is taken. The critical pressure gradient $(dp/dr)_{cr}$ is set at a fixed value in the simulation model, and tuned as necessary to allow for adequate growth of the wormhole network in the simulations. A similar approach has been adopted successfully in previous simulation studies of CHOPS (Sawatzky et al., 2002). Note that this value is approximately two orders of magnitude smaller than the value(s) of the critical pressure gradient reported by Tremblay and Oldakowski (2002; 2003) from their experiments. In the papers by Tremblay and Oldakowski (2002; 2003), the critical pressure gradient is estimated locally at the tip of a wormhole with an initial diameter of 2.5 cm. In the simulation model employed here, the value of the critical pressure gradient is a macroscopic one for a wormhole cell with horizontal dimensions 0.5 m × 0.5 m that is essentially an upscaled grid block containing a wormhole (see the discussion in Section 3.1.2).

Next, we discuss the treatment of the wormhole propagation rate in the simulation model. Tremblay developed an equation to represent the rate of advancement of the tip of a wormhole (Tremblay and Oldakowski, 2002; 2003). He derived the equation theoretically, based on a material balance of the fluidized sand and oil entering the wormhole from its tip. The equation follows below:

$$dr/dt = \frac{1-\varphi_v}{\varphi_v-\varphi_{fi}} \frac{dp}{dr} \frac{k_o}{\mu_o}, \quad 3\text{-}7$$

where dr is the incremental advancement of the wormhole tip in the direction perpendicular to its surface, dt is the increment in time, φ_v is the porosity in the wormhole after the sand in the arch has been fluidized (i.e., when the wormhole is filled with loose sand), φ_{fi} is the initial porosity in the (undisturbed) sand matrix at the tip of the wormhole, k_o is the permeability of the oleic phase (in Darcy), and μ_o is the viscosity of the oleic phase (in mPa·s). Tremblay tested this equation against the results of several laboratory experiments on wormhole growth, using a wormhole growth model that he had developed, and found good agreement between model and experiment (Tremblay and Oldakowski, 2003). Thus, Eq. 3-7 provides a good starting point for estimating the rate of wormhole advancement under field conditions, and offers a useful foundation for setting parameters in the numerical model used in this thesis.

However, Eq. 3-7 cannot be used explicitly in this simulation study to determine the rate of wormhole advancement. The rate of wormhole advancement in the numerical model is constrained by the discretized nature of the model, both in space and time. As noted in Section 3.1.1, the structure of the simulation model is such that a given wormhole tip within the branched fractal pattern (i.e., the outermost activated wormhole cell along a given branch of the fractal pattern) will advance one grid block (in the direction prescribed by the fractal pattern at that

location) at the end of any given time step if the pressure gradient at that wormhole tip exceeds the critical pressure gradient. As the size of every potential wormhole cell in the simulation grid is fixed at 0.5 m in each horizontal direction, this means that the rate of wormhole advancement at any position in the wormhole network and at any time during the simulation is determined by the size of the time step at that time. Thus, the time step size can serve as a useful tuning parameter in controlling the rate of wormhole advancement during the course of a simulation.

During early stages of CHOPS, the rate of wormhole network growth is fairly rapid since the pressure gradient at the tips of the wormholes in the network is fairly high during this period (Tremblay, 1999). A previous simulation study (Sawatzky et al., 2002) estimated the rate of wormhole network growth to be on the order of 1 metre per day for the CHOPS wells analysed in that study. Thereafter, the pressure gradient at the wormhole tips tends to decline gradually as the reservoir pressure beyond the wormhole network depletes. Consequently, as per Eq. 3-7, the rate of wormhole network growth becomes slower gradually; the study by Sawatzky et al. (2002) estimated that the rate of wormhole growth could drop to a level below 10 cm per day.

3.1.5 Sand Fluidization Model

The sand production profile for a typical CHOPS well can be divided approximately into two stages (Tremblay, 1999; Yuan et al., 1999; Sawatzky et al., 2002). Early in the life of most CHOPS wells, for the first three to six months, the sand production rate (or alternatively, the sand cut) is quite high. This first stage corresponds to a period of rapid growth of the wormhole network, in which most (if not all) of the wormholes in the network are filled with loose sand that flows as a plug with the heavy oil (Yuan et al., 1999; Sawatzky et al. 2002). Subsequently, the sand production rate drops rapidly as the oil production rate matures, eventually reaching a low but persistent level. This second stage corresponds to a period in which the rate of wormhole growth

slows down, and there is a shift to an increasing population of wormholes that are being scoured (i.e., they are being eroded by an open channel of heavy oil at the top). As the wormholes are being scoured, the sand flows through them at a much lower rate than the heavy oil.

As noted in Section 3.1.2, there is no attempt in the sand fluidization model presented here to represent the porosity and permeability of wormholes in both sand-filled states. Rather, a blended approach is taken using representative levels for porosity and permeability that are based on the results reported by Tremblay and Oldakowski (2002; 2003) for wormholes that are completely filled with sand. In this model, dynamic changes to the porosity and permeability in the wormhole network are designed to induce, in an average sense, the transport of sand and fluids through the network to the well that reflects the trends in production behaviour observed in CHOPS wells.

To this end, a pair of porosities is defined in the wormhole cells in the model, using a formulation that is available in CMG STARS®, the commercial flow simulator that serves as a platform for the flow simulations in this study. The first porosity is the void porosity, φ_v. This porosity is fixed, apart from changes that occur as a function of pressure and temperature; i.e., changes to the void porosity φ_v occur only via compressibility. In most applications (i.e., for simulating oil recovery processes other than CHOPS), the void porosity φ_v would be defined as the initial matrix porosity. However, it is advantageous in this application to define it as the porosity in the wormhole when it is completely filled with loose sand. Note that the notation used here for the void porosity is consistent with the notation used in Eq. 3-7.

The second porosity is called the fluid porosity φ_f. Its purpose is to represent the pore volume in a grid block available for fluid storage and transport. Since the fluid porosity φ_f is

allowed to change explicitly as a function of time, it is denoted here as φ_{fn} where *n* refers to the *nth* time step in a simulation. The initial fluid porosity φ_{fi} in a wormhole cell is set as the initial porosity in the (undisturbed) sand matrix at the tip of the wormhole. Again, the notation used here for the initial fluid porosity is consistent with the notation used in Eq. 3-7.

The void porosity φ_v and the fluid porosity φ_{fn} are connected in STARS® via the following relationship:

$$\varphi_{fn} = \varphi_v[1 - C_{vn}/\rho_c], \tag{3-8}$$

where C_{vn} is the (molar) concentration of the solid phase (i.e., *solid sand*) in the void space of the wormhole cell (i.e., in the pore volume of the cell as defined by φ_v) at time step *n*, in units of gmole/m^3, and ρ_c is the (molar) density of the sand in units of gmole/m^3. Thus, the ratio C_{vn}/ρ_c simply represents the volume concentration of solid sand in the void space of the wormhole cell at time step *n*.

The purpose of this rather elaborate formulation is to enable some of the sand that is initially part of the solid phase (i.e., the *Solid Sand*) to be converted into a component of one of the fluid phases, so that it can be fluidized (i.e., transported from one cell to the next). The sand in this fluidized state is referred to as *Mobile Sand*. Neither the structure of STARS®, nor that of other commercial flow simulators, permits changes to occur in the concentration of that part of the solid phase in a grid block as represented by the void porosity φ_v. Hence, the fluid porosity φ_f is introduced as an intermediary in the process of sand fluidization (i.e., mobilization).

With the use of Eq. 3-8, the initial concentration of solid sand C_{vi} in a wormhole cell can be set at a value that results in the desired value for the initial fluid porosity φ_{fi} in the wormhole

cell; i.e., the initial porosity in the (undisturbed) sand matrix at the tip of the wormhole. As a simulation unfolds, some of the *Solid Sand* is converted to *Mobile Sand*; in this state it is a component in the oleic phase. This conversion can be represented symbolically as:

Solid Sand (solid phase) → *Mobile Sand (oleic phase)* 3-9

The sand that has been converted to a component in the oleic phase is transported with this phase, from one wormhole cell in the wormhole network to the next one downstream until it reaches the well.

To execute the conversion from solid sand to mobile sand, at each time step n the concentration of solid sand C_{vn} is reduced from its value $C_{v(n-1)}$ at the previous time step (n-1), resulting in a corresponding increase in the fluid porosity φ_{fn}, as calculated from Eq. 3-8. Quantitatively, the process of sand fluidization is implemented using a pseudo kinetic model representing the rate of change with time of N_{msn}, the (molar) concentration of sand in the oleic phase in the void space of the wormhole cell at time step n, also in units of gmole/m^3. Evidently, N_{msn} is the counterpart in the oleic phase to the quantity C_{vn} in the solid phase. With this pseudo kinetic model, the rate of change with time of N_{msn} is defined as

$$(dN_{ms}/dt)_n = D_{ivn} \cdot v_{eln} \cdot r_{ms} \cdot \varphi_v \cdot C_{vn}, \quad 3\text{-}10$$

where $(dN_{ms}/dt)_n$ is in units of gmole/m^3/day, v_{eln} is a dimensionless velocity-dependent factor (so it depends on the time step n), r_{ms} is a constant factor in units of day^{-1} (sometimes referred to as a frequency factor), D_{ivn} is the time-varying dimensionless division factor available in STARS, given by

$$D_{ivn} = 1/(1 + A \cdot x_{msn})^B, \quad 3\text{-}11$$

where A and B are non-negative values that can be tuning parameters and x_{msn} is the mole fraction of *Mobile Sand* in the oleic phase at time step n. The time-varying division factor, D_{ivn}, ranging between 0 and 1, is particularly employed in Chapter 6 to adjust sand production at different times. As D_{ivn} is inversely proportional to x_{msn}, for a given set of coefficients A and B, it declines from 1 (only occurs at the first time step when x_{msn} = 0) to a low level over time as x_{msn} increases. Therefore, given certain constant values of A and B, D_{ivn} is close to 1 initially and does not overly suppress sand fluidization because x_{msn} is low during the initial stage of the production. However, as x_{msn} increases at the middle and late times, D_{ivn} and sand production $(dN_{ms}/dt)_n$ would become lower, according to Eqs. 3-10 and 3-11. If D_{ivn} = 1 at all times (i.e., ignoring Eq. 3-11), there could be too much sand being produced early on and the sand rate drops dramatically. However, adjusting the coefficients A and B offers the flexibility to model a wide range of sand production characteristics. The two parameters can be tuned such that less sand is produced during the early stages, reducing the amount of solid sand (C_{vn}) in the void space and allowing for a more sustained sand production throughout the middle and late times.

The dimensionless velocity-dependent factor v_{eln} in Eq. 3-10 is defined by the expression

$$v_{eln} = \begin{bmatrix} \left(\frac{v_n - v_{crit}}{v_{ref}}\right)^{exp} & \text{when } v_n > v_{crit} \\ 0 & \text{otherwise} \end{bmatrix}, \qquad 3\text{-}12$$

where v_n is the oleic phase Darcy velocity (in m/day) at time step n, v_{crit} is the critical oleic phase Darcy velocity (in m/day) for sand arch failure at the tip of the wormhole corresponding to the failure criterion given in Eq. 3-6, v_{ref} is a reference Darcy velocity (in m/day), and *exp* is a dimensionless exponent ≥1.

The pseudo kinetic model presented in Eq. 3-10 allows the concentration of mobile sand N_{msn} to be updated (i.e., increased) to its value $N_{ms(n+1)}$ at the next time step ($n+1$). From this conversion of solid sand to mobile sand, the concentration of solid sand C_{vn} can be updated (i.e., reduced) to its value $C_{v(n+1)}$ at the next time step ($n+1$) using the principle of mass balance.

Based on the analysis of Bratli and Risnes (1981), Tremblay et al. (1997) observed that the sand arch failure criterion at the tip of a wormhole can be recast, with the use of Darcy's law, from an expression for the critical pressure gradient to an expression for the critical flow rate q_{crit}. The result is

$$q_{crit} = 4\pi k_o R_c C_u / \mu_o, \qquad 3\text{-}13$$

assuming that the surface of the wormhole tip can be approximated by a hemisphere (see the brief discussion of the growth of a wormhole in Section 3.1.4, following Eq. 3-6). Note that the parameters on the right hand side of Eq. 3-13 are the same as they were defined for Eq. 3-6 and Eq. 3-7. In the experiments reported in Tremblay et al. (1997), the estimated critical flow rate required for the onset of massive sand production was considerably larger, by a factor of six, than the critical flow rate predicted using Eq. 3-13. This trend is opposite to the observations reported in subsequent experiments (Tremblay and Oldakowski, 2002; 2003), where the critical pressure gradient required for the onset of massive sand production was considerably smaller than the predicted critical pressure gradient. Likely, this is a consequence of the uncertainty in the value of the unconfined compressive strength of the sand arch C_u to be used in the expressions for the predicted critical pressure gradient / flow rate.

Given this uncertainty, Eq. 3-13 is not used directly in the simulation model to estimate the critical flow rate q_{crit}. Rather, the critical flow rate is treated as a tuning parameter to allow for

adequate sand transport between active wormhole cells in the simulations (i.e., to allow for adequate sand production at the well). This is similar to the treatment of the critical pressure gradient for wormhole network growth, as discussed following Eq. 3-6 in Section 3.1.4. As a starting point, q_{crit} is assigned the value reported from the experiments by Tremblay et al. (1997), 0.60 cm^3/min, and tuned slightly from there.

Note that the value of v_{crit}, the critical oleic phase Darcy velocity, used in Eq. 3-12 is calculated from the value of q_{crit} by treating the associated cross-sectional flow area as the area of the face of a wormhole cell perpendicular to the direction of the horizontal flow entering the cell (i.e., given the horizontal dimensions of a wormhole cell in this study, the cross-sectional flow area is 1.75 m^2).

The treatment of permeability in the wormhole cells is much simpler to describe. When a potential wormhole cell in the network is activated, the permeability k in that cell is modified from its value in the (undisturbed) sand matrix to a level on the order of thousands of Darcies to represent the effects of the transformation from undisturbed sand to failed (i.e., loose) sand. Subsequently, the permeability is increased further (but to a much lesser extent than in its initial jump) as the fluid porosity φ_{fn} increases. Although the Carman-Kozeny correlation describing the relationship between porosity and permeability does not apply, strictly speaking, to this case where the sand is loose, nevertheless it is a convenient vehicle for updating the permeability in an active wormhole cell in response to increases in the fluid porosity φ_{fn}. Thus, the permeability k_n at time step n (in Darcy) is represented by the formula

$$k_n = \frac{\varphi_{fn}^3}{c(1-\varphi_{fn})^2}, \qquad 3\text{-}14$$

where c is the Kozeny constant in units of Darcy^{-1}. The starting point of selection of c is based on an initial estimation of permeability within wormholes (k_i), on the order of 1,000 Darcies (Sawatzky et al., 2002). Given the φ_{fi} (0.348) and the initial estimation of k_i noted above, the initial c is calculated by Eq. 3-14. Subsequently, the initial choice for c is tuned by performing a set of simulations investigating how the oil production rate changes with changes in c. In light of Darcy's law, the oil production rate is affected by permeability and pressure gradient. So, the magnitude of k_i within the wormholes needs to be large enough to generate a sufficient level of the rate of oil production, as well as the rate of sand production (affected by the oleic phase Darcy velocity). Since the well is primarily constrained by the historical oil rate in this research (details seen in Section 4.1.3), an excessively large k_i may lead to a higher level of BHP (the secondary well constraint) to achieve the historical oil production rate. This would be unfavourable to the gas production rate.

3.1.6 Foamy Oil Model

If equilibrium conditions between the liquid phase and the gas phase are reached rapidly as the pressure declines below the bubble point, solution gas exsolving from the liquid phase forms a continuous free gas phase almost immediately. However, for a highly viscous liquid phase (e.g., heavy oil), there is a significant delay before equilibrium is reached between the liquid phase and the exsolved gas phase. Initially, as the pressure declines below the bubble point, not all of the gas that could exsolve (under equilibrium conditions) does exsolve – the oil is in a supersaturated state. Further, the gas that exsolves tends to be trapped in the liquid as a dispersed component (i.e., as bubbles). Eventually, with time and/or continuing pressure decline, the state of supersaturation disappears and the dispersed bubbles coalesce to form a continuous gas phase in equilibrium with the liquid phase (Lillico et al. 2001). The depressed pressure (with respect to the bubble point) at

which a continuous free gas phase begins to form is often called the pseudo bubble point. The pseudo bubble point is sensitive to the rate of pressure depletion and to the liquid phase viscosity.

The process by which dispersed gas bubbles nucleate, coalesce, and form a continuous free gas phase is complex. Dispersed bubbles are much smaller than the pore throats initially, but with time and/or continuing pressure decline they grow into larger bubbles that are trapped temporarily by the pore throats, forming bubble clusters (Sawatzky et al., 2002). These bubble clusters eventually coalesce to form a continuous free gas phase.

The complex non-equilibrium gas exsolution behaviour that occurs when the pressure in a heavy oil falls below the bubble point is called simply "foamy oil" behaviour typically, as noted in the Chapter 2. In this study, a (pseudo) kinetic model is employed to capture the changes in the state of the exsolved gas in the heavy oil, and the treatment of gas-liquid relative permeability is modified to account for the transport of exsolved gas in its different states. Together, the kinetic model and the modified gas-liquid relative permeability treatment constitute the foamy oil model for the simulations presented here.

The kinetic model put forward by Uddin (2005) is used in this research, with some simplifications. A total of five components are introduced to represent the behaviour of the fluids in this model: *Water* in the aqueous phase; *Dead Oil*, *CH4s*, and *CH4b* in the oleic phase; and *CH4g* in the gaseous phase. The key components in the kinetic model are *CH4s*, *CH4b*, and *CH4g*, as it is these components that describe the state of the gas in the system. The *CH4b* component is assumed to flow with the liquid (oleic) phase, but to possess a compressibility that is identical to the compressibility of the *CH4g* component in the gaseous phase. The physical properties of these three components (e.g., molecular weight, compressibility) are taken to be those of methane, as

methane is the predominant constituent of the gas present in western Canadian heavy-oil reservoirs that are exploited by CHOPS.

Two sets of pseudo reactions are implemented to describe the evolution of *CH4s* to *CH4g*.

Nucleation of dispersed bubbles from solution gas:

$$CH4s\ (Oleic) \rightarrow CH4b\ (Oleic) \qquad 3\text{-}15$$

Coalescence of dispersed bubbles to free gas:

$$CH4b\ (Oleic) \rightarrow CH4g\ (Gaseous) \qquad 3\text{-}16$$

The kinetic model presented by Uddin (2005) contains a second pseudo reaction to represent nucleation and a second pseudo reaction to represent coalescence. Each of these additional reactions are autocatalytic, intended to accelerate the rate of nucleation of dispersed bubbles from solution gas and the rate of coalescence of dispersed bubbles to free gas. In this study, it was found that the autocatalytic reactions were not needed to capture the non-equilibrium behaviour between the exsolved gas and the heavy oil under field conditions for CHOPS; the reactions presented in Eq. 3-15 and Eq. 3-16 are sufficient to capture the non-equilibrium response to pressure depletion. Anecdotally, it appears that the acceleration of nucleation and coalescence rates provided by autocatalytic reactions is necessary to capture the nonequilibrium behaviour observed in laboratory-scale experiments where the pressure depletion rates are often relatively high, but unnecessary in simulations of CHOPS behaviour under field conditions where the pressure depletion rates are generally much smaller than in laboratory experiments.

Quantitatively, the rate of nucleation of dispersed bubbles from solution gas and the rate of coalescence of dispersed bubbles to free gas are defined by the following expressions:

$$\begin{cases}(dN_{CH4b}/dt)_n = r_{CH4b} \cdot N_o \cdot (x_{CH4sn} - x'_{CH4sn}) \\ (dN_{CH4g}/dt)_n = r_{CH4g} \cdot N_o \cdot x_{CH4bn}\end{cases}, \quad 3\text{-}17$$

where $(dN_{CH4b}/dt)_n$ and $(dN_{CH4g}/dt)_n$ are the rate of methane bubble nucleation and the rate of methane bubble coalescence (in gmole/m^3/day) at time step n, respectively, N_{CH4b} is the (molar) concentration of *CH4b* in the oleic phase (in gmole/m^3) at time step n, N_{CH4g} is the (molar) concentration of *CH4g* in the gaseous phase (in gmole/m^3) at time step n, r_{CH4b} and r_{CH4g} are each constant factors in units of day^{-1} (sometimes referred to as frequency factors, similar to the constant factor r_{ms} in Eq. 3-10), x_{CH4sn} refers to the mole fraction of *CH4s* in the oleic phase at time step n with x'_{CH4sn} representing the value of this quantity under equilibrium conditions, x_{CH4bn} refers to the mole fraction of *CH4b* in the oleic phase at time step n, and finally, $N_o = \varphi_{fn} S_{on} \rho_{on}$ is the (molar) concentration of the oleic phase in the void space of a grid block in units of gmole/m^3, with φ_{fn} as the fluid porosity defined in Section 3.1.5, S_{on} as the oil saturation, and ρ_{on} as the molar density of the oleic phase (in gmole/m^3) at time step n.

3.1.7 Equilibrium Composition for Methane

The equilibrium mole fraction of *CH4s* in the oleic phase at time step n, x'_{CH4sn}, can be calculated from y'_n, the equilibrium mole fraction of *CH4g* in the gaseous phase at time step n, and the *K*-value connecting these quantities, K_{CH4}:

$$x'_{CH4sn} = y'_{CH4gn}/K_{CH4}. \quad 3\text{-}18$$

Here, *K*-values are used in the CMG STARS simulator to model the fluid PVT (Pressure-Volume-Temperature) properties, rather than equations of state (EOS). The primary advantage is that the *K*-value method is simpler and computationally faster than EOS. Further, it has been shown experimentally that for the type of solvent-heavy oil mixtures considered in this study (methane-

heavy oil, CO_2-heavy oil), the measured K-values are independent of composition and are functions only of temperature and pressure (Ma et al., 2023). This implies that the heavy oil interacts with solvents such as methane and CO_2 as a single component.

During the CHOPS process, it is assumed that methane is the single constituent of the three gaseous components that appear in the simulation model. Therefore, the gaseous phase consists of only a single component, *CH4g*, implying that $y'_{CH4gn} = 1$. Consequently, Eq. 3-18 can be simplified to become

$$x'_{CH4sn} = 1/K_{CH4}, \tag{3-19}$$

A modified version of the "Antoine Equation" is used as a correlation for the dependence of K_{sg} on pressure and temperature:

$$K_{CH4} = (K_{v1}/p + K_{v2} \cdot p + K_{v3}) \cdot e^{\frac{K_{v4}}{(T - K_{v5})}}, \tag{3-20}$$

where p is the pressure (in kPa); T is the temperature (in °C); and K_{v1}, K_{v2}, K_{v3}, K_{v4}, and K_{v5} refer to the correlation coefficients. The values selected for the correlation coefficients in the simulation studies for CHOPS are shown in Table 3.1.

Coefficient	Value
K_{v1} (kPa)	418990.7
K_{v2} (1/kPa)	0.005483
K_{v3}	-9.28995
K_{v4} (°C)	-885.8
K_{v5} (°C)	-267.12

Table 3.1 Correlation coefficients for K_{CH4}.

3.1.8 Gas/Oil Mixture Viscosity

The default logarithmic phase mixing rule in the STARS is used to determine the oleic phase viscosity.

$$ln(\mu_o) = \sum[x_i \cdot ln(\mu_i)], \quad 3\text{-}21$$

where μ_o is the viscosity of gas/oil mixture; x_i is the mole fraction of component *i* in the oleic phase; and μ_i is the pseudo viscosity of component *i*.

3.2 Model Development for CSI processes

In this research work, the reservoir condition at the end of CHOPS (e.g., pressure, porosity, fluid saturations, and gas and oil composition) is established as the initial reservoir condition for subsequent CSI processes. Nevertheless, given the fact that barely sand is produced at the late stage of the CHOPS, and mobile sand tends to settle down during the injection and soaking periods in the CSI due to the negligible oleic phase Darcy velocity in the reservoir, it is assumed that the permeability of wormhole cells is decreased by a factor of ten during CSI processes compared to that at the end of CHOPS. Additionally, the CSI process initiates from $t = 0$. In the following discussions, any reference to time refers to $t \geq 0$.

The model is implemented in a thermal three-phase multi-component flow simulator STARS® (Computer Modelling Group 2018) serving as the platform for the flow simulations. Restart files are built for the CSI processes based on the CHOPS model. In the CSI process, many important mechanisms should be taken into consideration to develop a simulation model, such as non-equilibrium solubility of solvents, foamy oil flow, oil swelling, oil viscosity reduction, dispersion, gas expansion and relative permeability hysteresis (Chang and Ivory, 2013). The

relative permeability hysteresis is neglected here as only one set of relative permeability curves is adopted in both injection and production processes.

3.2.1 Gas Dissolution

In CSI processes of this research, pure CO_2 is injected into the reservoir to enhance the heavy oil recovery. Generally, CO_2 exhibits more solubility in water than in heavy oil at given pressure and temperature conditions (Young and Stephenson, 1983; Chang et al., 1996). However, CO_2 dissolution into an aqueous phase is not considered in this research. Primarily, this is because there is much less water in heavy oil reservoirs than heavy oil. For example, the water saturation at the end of the CHOPS process is only one-third of oil saturation. Further, the water is distributed in thin films and pendicular rings, making it much less accessible to the injected CO_2 than heavy oil is. Therefore, the amount of CO_2 that dissolves in the aqueous phase is expected to be much smaller than the amount of CO_2 that dissolves in the oleic phase.

Kinetic reactions in STARS are used to represent the delay in a solvent dissolving into heavy oil. In the CSI process, a total of eight components are introduced to represent nonequilibrium processes in the model: *Water*, *Oil*, *CH4g*, *CH4s*, *CH4b*, *CO2g*, *CO2s* and *CO2b*. The last three new components related to CO_2 represent CO_2 free gas, dissolved CO_2 and CO_2 dispersed bubbles, respectively. Note that methane dispersed bubbles remain in bubble state during the pressurization process, rather than re-dissolving in the heavy oil. The non-equilibrium behaviour of dissolution in the CSI process is represented by:

$$\begin{cases} CH4g\ (Gaseous) \rightarrow CH4s\ (Oleic) \\ CO2g\ (Gaseous) \rightarrow CO2s\ (Oleic) \end{cases} \qquad 3\text{-}22$$

The rate of dissolution for methane and CO_2 from free gas to dissolved gas during the pressurization process in CSI is expressed as:

$$\begin{cases}(dN_{CH4s}/dt)_n = r_{CH4s} \cdot N_o \cdot (x'_{CH4sn} - x_{CH4sn}) \\ (dN_{CO2s}/dt)_n = r_{CO2s} \cdot N_o \cdot (x'_{CO2sn} - x_{CO2sn})\end{cases}, \quad 3\text{-}23$$

where $(dN_{CH4s}/dt)_n$ and $(dN_{CO2s}/dt)_n$ are dissolving rates for methane and CO_2 (in gmole/m^3/day) at time step *n*, respectively; N_{CH4sn} and N_{CO2sn} represent molar concentrations of *CH4s* and *CO2s* in the oleic phase (in gmole/m^3) at time step *n*; r_{CH4s} and r_{CO2s} are the reaction frequency factor (*rrf*) for methane and CO_2 dissolution (in day^{-1}); *t* is time (in days); x_{CH4sn} and x_{CO2sn} refer to the mole fraction of *CH4s* and *CO2s* in the oleic phase at time step *n*, and x'_{CH4sn} and x'_{CO2sn} represent the equilibrium mole fraction of *CH4s* and *CO2s* in the oleic phase at time step *n*; and finally, $N_o = \varphi_{fn} S_{on} \rho_{on}$ is the molar concentration of the oleic phase in each grid block (including matrix and wormhole cells) in units of gmole/m^3, with φ_{fn} as the fluid porosity defined in Section 3.1.5, S_{on} is the oil saturation and ρ_{on} is the molar density of the oleic phase (in gmole/m^3) at time step *n*.

3.2.2 Gas Exsolution

Similarly, pseudo kinetic reactions are used to simulate the non-equilibrium exsolution process to represent foamy oil behaviour. The kinetic model developed by Uddin (2005) is used in this study, with some simplifications, as the treatment is taken from Section 3.1.6. Additionally, the kinetic model does not represent the transport behaviour. A modified relative permeability approach is adopted to capture the trapped behaviour of large bubbles; i.e., a delay of free gas flowing led by non-zero critical gas saturation is used to describe the behaviour of large bubbles (Section 4.2.3). The pseudo reactions of the non-equilibrium gas exsolution for methane is seen in Section 3.1.6, and for CO_2 is defined as follows:

$$\begin{cases} CO2s\ (Oleic) \rightarrow CO2b\ (Oleic) \\ CO2b\ (Oleic) \rightarrow CO2g\ (Gaseous) \end{cases} \quad 3\text{-}24$$

Similar to methane exsolution in Eq. 3-17, the rate of nucleation of CO_2 dispersed bubbles from solution gas and the rate of coalescence of CO_2 dispersed bubbles to free gas are defined by the following expressions:

$$\begin{cases} (dN_{CO2b}/dt)_n = r_{CO2b} \cdot N_o \cdot (x_{CO2sn} - x'_{CO2sn}) \\ (dN_{CO2g}/dt)_n = r_{CO2g} \cdot N_o \cdot x_{CO2bn} \end{cases}, \quad 3\text{-}25$$

where $(dN_{CO2b}/dt)_n$ and $(dN_{CO2g}/dt)_n$ are the rate of bubble nucleation and the rate of bubble coalescence (in gmole/m^3/day) for CO_2 at time step n, respectively; N_{CO2bn} is the molar concentration of *CO2b* in the oleic phase (in gmole/m^3) at time step n; N_{CO2gn} is molar concentration of *CO2g* in the gaseous phase (in gmole/m^3) at time step n; r_{CO2b} and r_{CO2g} are reaction frequency factors (*rrf*s) in units of day^{-1}; x_{CO2sn} refers to the mole fraction of *CO2s* in the oleic phase at time step n; x'_{CO2sn} represents the equilibrium mole fraction of *CO2s* in the oleic phase at time step n; and x_{CO2bn} refers to the mole fraction of *CO2b* in the oleic phase at time step n.

3.2.3 Equilibrium Composition for CO_2

Solvent dissolution and exsolution rates depend on how far the solvent mole fraction in the oil is from its equilibrium value. The latter is determined from its *K*-value at the particular temperature and pressure representing the equilibrium pressure/volume/temperature behaviour for each component (e.g., *CH4s*, *CO2s*). The mole fraction for methane under an equilibrium condition is determined by Eq. 3-18 during both CHOPS and CSI. *K*-value for CO_2 is given by

$$K_{CO2} = y'_{CO2gn}/x'_{CO2sn}, \quad 3\text{-}26$$

where x'_{CO2sn} is the equilibrium mole fraction of *CO2s* in the oleic phase and y'_{CO2gn} is the equilibrium mole fraction of *CO2g* in the gaseous phase at time step *n*.

K-values for CO_2 shown in Table 3.2 are input as a form of a table into the simulator. Since few publications precisely document the PVT data of CO_2 with the heavy oil from the selected Dee Valley wells in Chapter 7, the *K*-values obtained for CO_2 in this thesis are determined from the CMG WINPROP simulator based on several studies that experimentally examined the solubility of CO_2 in Lloydminster heavy oil (Quail et al., 1988; Tharanivasan et al., 2006; Wang et al., 2020; Ganapathi et al., 2022).

Pressure, kPa	100	600	1100	1600	2100	2600	3100	3600
K_{CO2}	75.98	13.06	7.35	5.21	4.10	3.41	2.96	2.63

Table 3.2 *K*-values for CO_2 at different pressure and 20 °C.

3.2.4 Gas/Oil Mixing Process

The process of gas mixing with heavy oil is affected by the mechanisms of advection, dissolution and dispersion, as schematically shown in Figure 3.4. Advection is the primary mechanism that depicts the transportation of the gas by bulk motion in the reservoir, the wormhole system in particular, after the injection. The nonequilibrium dissolution and exsolution processes are modeled as kinetic reactions, as discussed in previous subsections. Dispersion, composed of two parts: molecular diffusion and mechanical dispersion, allows a component to spread or scatter within a phase. Additionally, the solvent adsorption on solid phase is not considered in the schematic or in simulations.

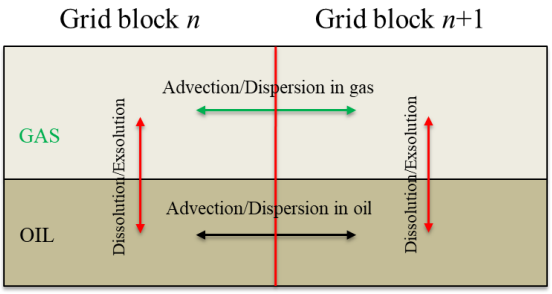

Figure 3.4 Gas/oil mixing mechanisms (Chang and Ivory, 2015).

In each phase, the advection–dispersion equation (Fried and Combarnous, 1971) is represented by:

$$\frac{\partial C}{\partial t} = \nabla(D\nabla C) - \nabla(uC) + R, \qquad 3\text{-}27$$

where C is the concentration of solvent in each phase (in gmole/pore m^3); $D\nabla C$ is the dispersion term; ∇C is the concentration gradient for solvent in each direction (in gmole/pore m^3/m); $-\nabla(uC)$ is the advection term; u is the phase interstitial velocity (in m/day); R is the sources or sinks of the solvent (in gmole/pore m^3/day), which refers to the solvent injection rate in the gaseous phase and to the solvent dissolution rate in the oleic phase; and D is the dispersion (in m^2/day), given by the STARS simulator:

$$D = D_{mij}/\tau_{jk} + \alpha_{jk}|u_j|, \qquad 3\text{-}28$$

where D_{mij} is the molecular diffusion coefficient (in m^2/day) of component i in phase j; τ_{jk} is the tortuosity for phase j in direction k, defined as the ratio of the true path length traveled by a particle flowing through the medium to the macroscopic distance traveled; α_{jk} is the dispersivity coefficient (in m) for phase j in direction k; and $|u_j|$ is the magnitude of interstitial velocity (in m/day) of phase j.

The term D_{mij}/τ_{jk} is called the apparent or effective molecular diffusion coefficient. In the STARS simulator, the dispersion flux is governed by:

$$J_{ijk} = -\varphi_f S_j (D_{mij}/\tau_{jk} + \alpha_{jk} \cdot |u_j|) \nabla_k C_{ij}, \quad 3\text{-}29$$

where J_{ijk} is the dispersion flux of component i in phase j in direction k (in gmole/m^2/day); φ_f is the fluid porosity available for reservoir liquids transportation and storage; S_j is the saturation of phase j; $\nabla_k C_{ij}$ is the concentration of component i in phase j in direction k (in gmole/pore m^3/m).

A few publications (Wang, et al., 2020; 2022) reported laboratory measurements of molecular diffusion coefficient of CO_2 in heavy oil from Plover Lake (dead-oil viscosity of 1,500 mPa·s at 20 °C), variations of 3~27×10^{-9} m^2/s under different pressure conditions. The other study (Tharanivasan, et al., 2006) experimentally tested the molecular diffusion coefficient of CO_2 in heavy oil from the Lloydminster area (dead-oil viscosity of 20,267 mPa·s at 23.9 °C) at the magnitude of 0.49~0.94×10^{-9} m^2/s at different boundary condition. Chang and Ivory (2013) used the coefficient of 4.32×10^{-5} m^2/day for oleic components in heavy oil from the Lloydminster area (dead-oil viscosity of 18,755 mPa·s at 23.4 °C), which was equal to 0.5×10^{-9} m^2/s, the same order of magnitude as the study by Tharanivasan, et al. (2006). The higher viscosity of the heavy oil would negatively affect the diffusivity of a component spreading within the oleic phase (Okazawa, 2009). A diffusion coefficient of 0.0144 m^2/day for gaseous components in the gas phase and a mechanical dispersion coefficient of 0.005 m for both gas and oil phases were used in the study by Chang and Ivory (2013). These settings are also used in this thesis.

CHAPTER 4: PRODUCTION DATA AND MODEL SETUPS

There are three steps included in this research. The first step of this research is to develop an improved model by making appropriate modifications to the proposed model (Yu and Leung, 2020). The production data employed for the improved model is derived from a Cold Lake heavy oil deposit in western Canada as the previous study did (Yu and Leung, 2020). The second step of this research involves applying the improved model from the first step to CHOPS wells located in the Lloydminster area of western Canada. The third step of this research is to conduct CSI processes following the predictions from the second step of this research. Naturally, production data are consistent with the second step. The primary objective of this chapter is to summarize the collections of field production data, reservoir properties and the basic model setups of this research.

4.1 Reservoir Data and Model Setup for the CHOPS Well from Cold Lake

A single CHOPS well in a Cold Lake heavy oil deposit in western Canada is used to illustrate the validation of the improved CHOPS simulation model presented in Chapter 5. This well was introduced in the CHOPS simulation paper by Istchenko and Gates (2012), as an example serving to demonstrate the capability of their simulation model to history match production from a CHOPS well. Publicly-available production data for the well (i.e., daily oil, water and sand production rates averaged over each month), along with average reservoir properties for the producing formation, are provided in Istchenko and Gates (2012).

4.1.1 Reservoir Settings

This data forms the basis for the information on the historical production rates and average reservoir properties used in this research. A description of the average reservoir properties and the

simulation grid used in modelling CHOPS production from this well is presented in Table 4.1. Previous simulation studies of CHOPS showed that pressure depletion is relatively modest beyond the outer envelope of the wormhole network (Sawatzky et al., 2002; Yu and Leung, 2020). Therefore, to reduce the simulation time but allow for finer horizontal grid blocks, the computational domain in the horizontal plane was chosen to be smaller in this simulation study than in the study by Istchenko and Gates (2012). Here, the size of the horizontal domain is 250 m × 250 m (see Figure 4.1), whereas it was 400 m × 400 m in the study by Istchenko and Gates (2012). In Section 5.4, a sensitivity analysis of the effects of the horizontal domain size on the simulation results is presented. Another consideration is that, as discussed in Section 3.1.2, the uncertainty in the diameter of wormholes renders a wormhole cell with horizontal dimensions 0.5 m × 0.5 m that is essentially an upscaled grid block containing a wormhole. Further refinement of the mesh representing wormhole cells smaller than 0.5 m is certainly possible, but that would demand substantial computational cost. A smaller diameter of wormholes than 0.5 m is thus not inclined to model in this research.

Property	Values
Model size (m)	250 × 250 × 6.5
Number of grid cells	100 × 100 × 3
Grid cell sizes ($\Delta x \times \Delta y \times \Delta z$) (m)	Top layer: 2.5 × 2.5 × 1.5 Middle layer: 2.5 × 2.5 × 3.5 Bottom layer: 2.5 × 2.5 × 1.5
Locally refined cell size ($\Delta x \times \Delta y \times \Delta z$) (m)	Middle layer only: 0.5 × 0.5 × 3.5
Depth, True Vertical Depth (TVD) (m)	423.5
Pay thickness (m)	3.5
Homogeneous case fluid porosity (fraction)	0.348
Homogeneous case permeability in all directions (Darcy)	3
Upper-bound of the wormhole porosity (fraction)	0.53
Initial oil saturation (fraction)	0.72
Dead-oil viscosity (mPa·s)	41,790 @ 20°C
Solution Gas-Oil Ratio (GOR) (m^3/m^3)	10
Mole fraction of CH_4 at initial reservoir conditions (fraction)	0.18
Initial reservoir pressure (kPa)	2600

Table 4.1 Description of the average reservoir properties and simulation grid used in this study for a Cold Lake CHOPS well.

Note as well that the computational grid in the vertical direction is chosen differently for this simulation study than in the study by Istchenko and Gates (2012). The vertical grid blocks are coarser in this study. Here, the reservoir pay is represented by a single layer that is 3.5 m thick; it is assumed to contain the wormhole network. Above and below this layer, two thinner layers have been added, a top layer and a bottom layer, each 1.5 m thick, to represent, conceptually, layers in the reservoir containing heavy oil that are not of adequate quality to be considered pay. As these layers are absent in the geological model presented by Istchenko and Gates (2012), for convenience they are populated with the same average reservoir properties as the middle layer containing the pay.

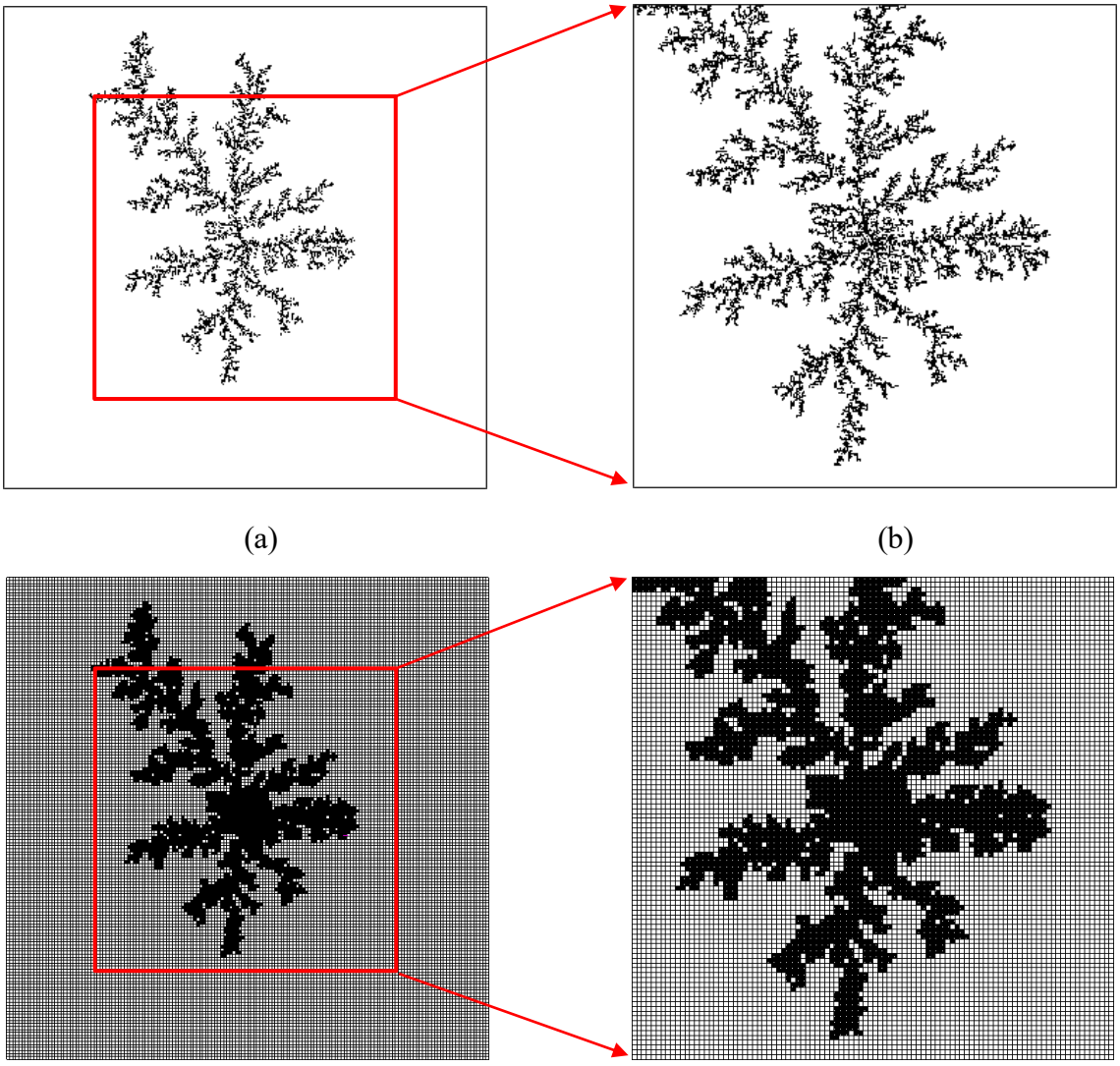

Figure 4.1 (a) Original fractal pattern, as generated by the DLA algorithm; (b) middle portion of the original fractal pattern; (c) computational grid for the original fractal wormhole pattern; (d) computational grid for the portion shown in (b).

4.1.2 Relative Permeability Model

The oil-water and gas-liquid relative permeability curves shown in Figure 4.2 are based on several other studies of CHOPS wells in the same Cold Lake area (e.g., Istchenko and Gates (2012) and Fan et al. (2019)). As in the former studies, a non-zero critical gas saturation was adopted to model the effects on gas transport caused by the trapping of large gas bubbles at the pore throats. The

critical gas saturation serves as a tuning parameter in the simulations; here, a final critical gas saturation of 0.05 was selected.

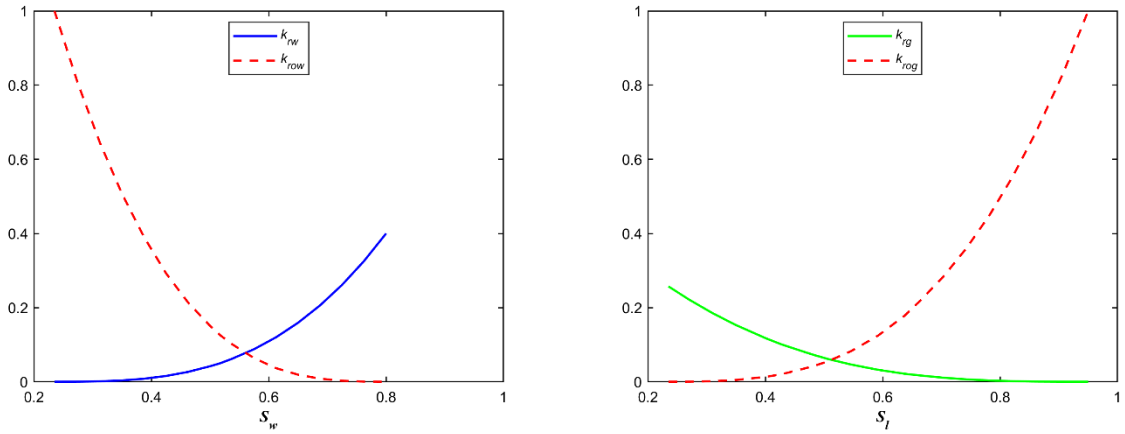

(a) (b)

Figure 4.2 Relative permeability curves in the simulation model: (a) oil-water system; (b) gas-liquid system.

4.1.3 Field Data Conditioning

As noted in Section 4.1.1, historical production data for a single CHOPS well, such as daily oil, water and sand production rates (averaged over each month), was extracted from Istchenko and Gates (2012) for this simulation study. The historical oil and sand production data for the well is shown in Figure 4.3.

The simulations of CHOPS production were performed using the oil production rate at surface conditions as the primary constraint. For this well, it is the only viable option. Other data associated with production from the well (e.g., BHP) is not provided by Istchenko and Gates (2012). In fact, such data is unlikely to exist. Direct measurement of BHP is an expense that is rarely, if ever, undertaken by CHOPS operators. Measurements of the fluid level in the annulus between the tubing and the casing provide a proxy for estimating the BHP (frequency of measurement varies widely, depending on the operator and the age of the well), but operators are

not required to transfer this information to the public domain. Consequently, we are left with oil production rate as the primary constraint.

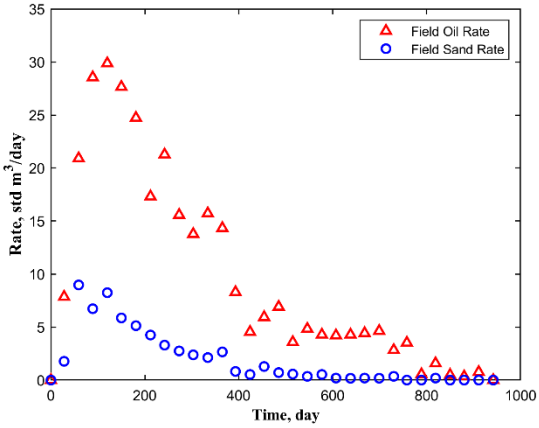

Figure 4.3 The historical oil and sand production rates for the Cold Lake CHOPS well.

There is one small problem with this. Given the structure of STARS®, the rate constraint must be applied to the production rate of the oleic phase. There are two components in the oleic phase under surface conditions in the simulations – *Dead Oil* and *Mobile Sand* (Section 3.1). Thus, it is the total production rate of oil and sand that is constrained in the simulations, not simply the oil production rate. Consequently, the historical sand production rate for the well must be added to the historical oil production rate in order to construct an appropriate target for the simulated rate constraint. Fortunately, as cumulative sand production over the life of a CHOPS well is generally a small fraction of the cumulative oil production (e.g., see Figure 4.3), any errors induced by this discrepancy should be small.

In applying production rate as the primary constraint in the simulations, some conditioning (i.e., smoothing) of the data is preferable. For example, if the daily oil production rate averaged over each month is assigned directly to each day in the month, there will be an abrupt change in the oil production rate profile at the end of each month. During the early months of production (as

shown in Figure 4.3), the jump in rate at the end of each month will be significant. This can (and does) lead to various convergence problems. To mitigate this, one option is to smooth the field data with a moving average over a period of several months. This option is taken up in this study, where the moving average is applied over a window of three months. In other words, instead of using the field data as it is supplied, with a daily production rate averaged over each month, the assigned daily production rate in a given month is averaged over 3 months – previous month, current month, and next month. To further facilitate a more gradual ramp-up and decline in the rate constraint, it is assigned on a weekly (1/4 of a month) basis, where the production rate for a particular week in a month is linearly interpolated between the average daily rates for the current month and the next month. Figure 4.4 illustrates the field oil production rate as it was supplied initially, compared with a smoothed version.

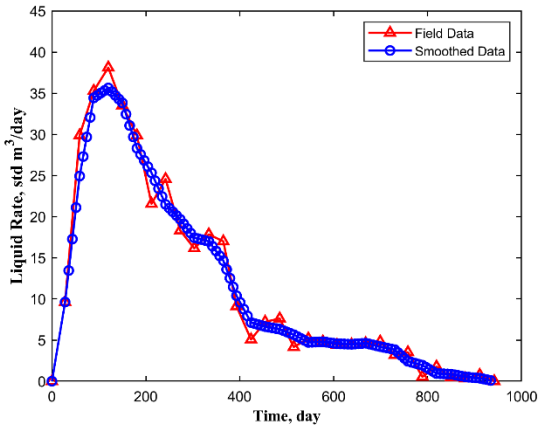

Figure 4.4 Producing oil rate – daily rate averaged monthly and a smoothed version.

4.2 Reservoir Data and Model Setup for the CHOPS Wells from Dee Valley

Three CHOPS wells drilled in the Waseca formation in the Mannville Group of Lower Cretaceous age and located in the Dee Valley in the Lloydminster area of western Canada, are modelled (Wong et al., 2005) in Chapters 6 and 7. They reported that the Waseca formation was separated by a shale barrier. The pool was thus segregated into upper and lower layers with different reservoir quality.

Moreover, a gas cap was identified in the upper formation. However, each well's perforation layer and corresponding reservoir quality are unknown. Thus, a basic assumption is that these three wells' reservoir properties and lithology are identical.

4.2.1 Production histories

The oil, water, sand, and gas production data for these three wells are extracted from Wong et al. (2005), and they are compared against the profile used in the study by Yu and Leung (2020) and introduced in Section 4.1 in Figure 4.5, which was extracted from the study by Istchenko and Gates (2012). The primary analyses of production behaviours of the CHOPS wells modelled in Chapter 5 with Chapters 6 and 7 are listed as follows.

- The oil production from the Cold Lake CHOPS well (introduced in Section 4.1 and modelled in Chapter 5) in Figure 4.5 (a) and (b) is reaching its peak rapidly and dropping to an uncommercial level quickly. The three new oil production profiles show a more sustained and steadier trend, with minor fluctuations in well-2 and well-3.

- The cumulative sand production at the end of CHOPS for these three wells in Figure 4.5 (c) is much less than in Section 4.1 shown in Figure 4.5 (d). A large amount of sand is produced at the initial stage in the CHOPS well from Cold Lake (modelled in Chapter 5), followed by a rapid decline to a negligible level at the late stage. Instead, the sand production performs different behaviours in the three new CHOPS wells. Cumulative sand production steadily increases over time, with neither a large amount of sand produced at the initial stage nor negligible sand production at the late stage. Even significant sand production can be observed only in the middle to late stages in well-3. Due to such great

differences compared to the CHOPS well from Cold Lake, the sand production model needs to be improved to capture the characteristics.

- The water production profiles are compared in Figure 4.5 (e). There appears to be some correlation between water and oil production profiles in some instances. For example, the sharp rise in water production near 800 and 1200 days in well-1 coincides with the increasing oil rate, suggesting that there could be sudden drops in the flowing BHP. However, the cumulative water production from Cold Lake did not observe the correlation as water production can be attributed to an aquifer. On the other hand, oil production in well-3 is less than well-2, whereas its water production is greater than well-2.

- The dramatic elevation in producing GOR at later times in Figure 4.5 (f) indicates that gas from the gas cap may enter the wormholes and break through to the wellbore. No gas production data for this CHOPS well from Cold Lake was available or presented in previous studies in the literature.

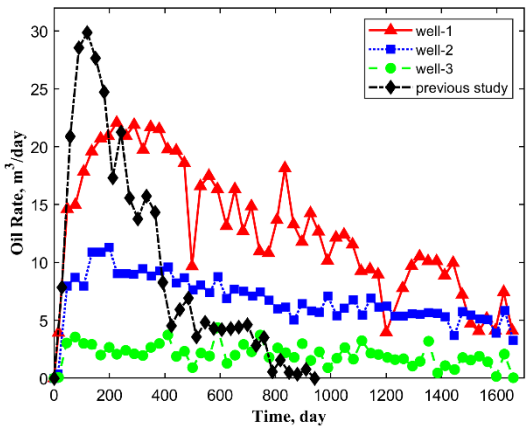

(a)

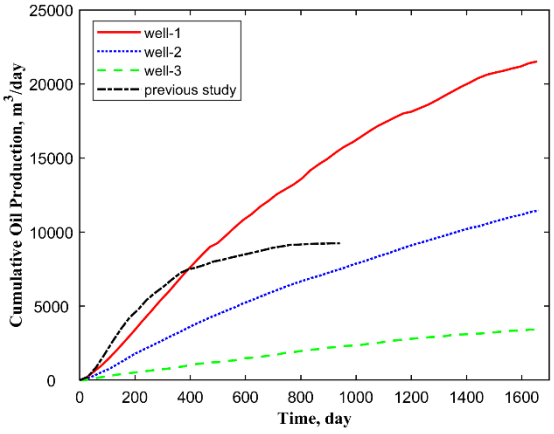

(b)

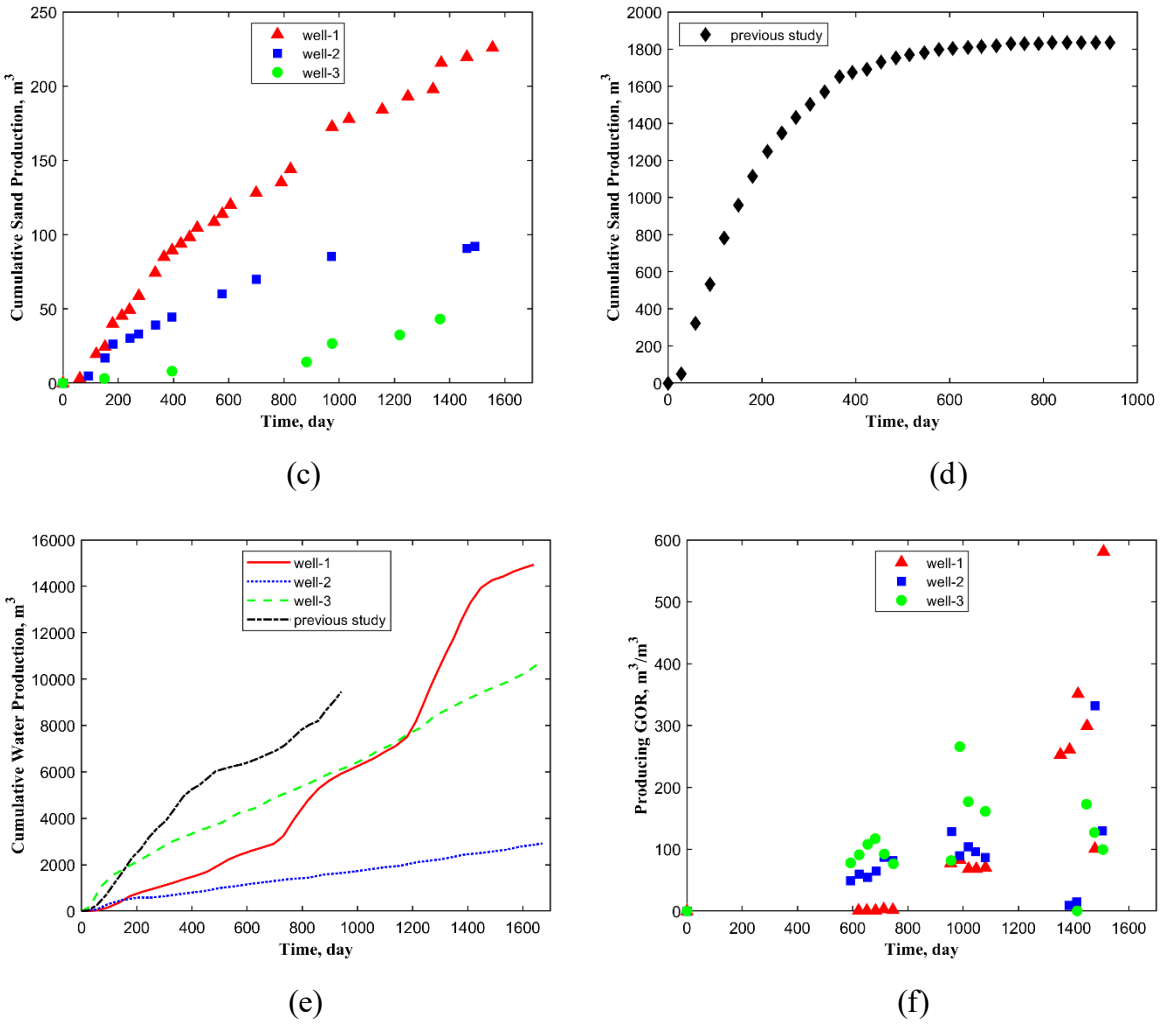

Figure 4.5 Historical data for two studies: (a) oil rate; (b) cumulative oil production; (c) sand production in this chapter; (d) sand production in Chapter 3; (e) cumulative water production and (f) producing GOR.

4.2.2 Reservoir Settings

Three CHOPS wells presented in Section 4.2.1 located in the Dee Valley in the Lloydminster area of western Canada are modelled (Wong et al., 2005). Since limited publications revealed the field information, the parameters for these wells are extracted from several studies in the literature (Wong, 2001; Meza-Díaz et al., 2011; Meza-Díaz et al., 2012; Coskuner et al., 2015; Riazi and Russell, 2014; Freitag, 2018). The model parameters are summarized in Table 4.2. The domain size is 400 m × 400 m × 6.5 m, and it is discretized using a 160 × 160 × 3 mesh. It is further assumed that the wormholes exist only in the middle layer.

Property	Values
Model size (m)	400 × 400 × 6.5
Number of grid cells	160 × 160 × 3
Grid cell sizes ($\Delta x \times \Delta y \times \Delta z$) (m)	Top layer: 2.5 × 2.5 × 1.5 Middle layer: 2.5 × 2.5 × 3.5 Bottom layer: 2.5 × 2.5 × 1.5
Locally refined cell size ($\Delta x \times \Delta y \times \Delta z$) (m)	Middle layer only: 0.5 × 0.5 × 3.5
True Vertical Depth (TVD) (m)	423.5
Pay thickness (m)	3.5
Homogeneous case fluid porosity (fraction)	0.348
Homogeneous case permeability in all directions (Darcy)	1.25
Upper-bound of the wormhole porosity (fraction)	0.53
Initial oil saturation (fraction)	0.72
Dead-oil viscosity (mPa·s)	5,000 @ 20°C
Solution Gas-Oil Ratio (GOR) (m^3/m^3)	8
Mole fraction of CH_4 at initial reservoir conditions (fraction)	0.149
Initial reservoir pressure (kPa)	3000
Unconfined compressive strength (kPa)	30.5

Table 4.2 Simulation model parameters for the Cold Lake CHOPS well for this chapter.

The dead-oil viscosity at 20 °C is 5,000 mPa·s (provided in Table 4.2). Few publications report the dead-oil viscosity from the selected Dee Valley wells perforated in the Waseca formation (Wong et al., 2005). Studies (Coskuner et al., 2013; Riazi et al., 2014) reported the dead oil viscosity from the Sparky formation in Dee Valley, 14,000 mPa·s at 20 °C. Meza-Díaz et al. (2011; 2012) provided the dead oil viscosity from the pools operated by Husky in Dee Valley, approximately 5,000 mPa·s at 20 °C. The latter was verified by Sawatzky who has been supervising this research and participated in Husky's petroleum programs in Dee Valley.

Prescribed fractal patterns used for three wells are shown in Figure 4.6. Fractal patterns with different densities are employed in different wells corresponding to their production characteristics. Yu and Leung (2020) reported that different fractal patterns could result in different simulating results, and the lower production case is often associated with fractal patterns consisting of fewer branches and reduced wormhole intensity around the wellbore. On the other hand, more densely populated branches may be associated with higher oil and sand production. As a result, the visually densest fractal pattern (Figure 4.6 (a) with the most branches) is adopted in well-1. The fractal pattern density (D_{fp}) over a distance away from the wellbore r_o is shown in Figure 4.6 (d), with fractal dimensions of 1.7337, 1.6982 and 1.6656 for well-1, well-2 and well-3, respectively.

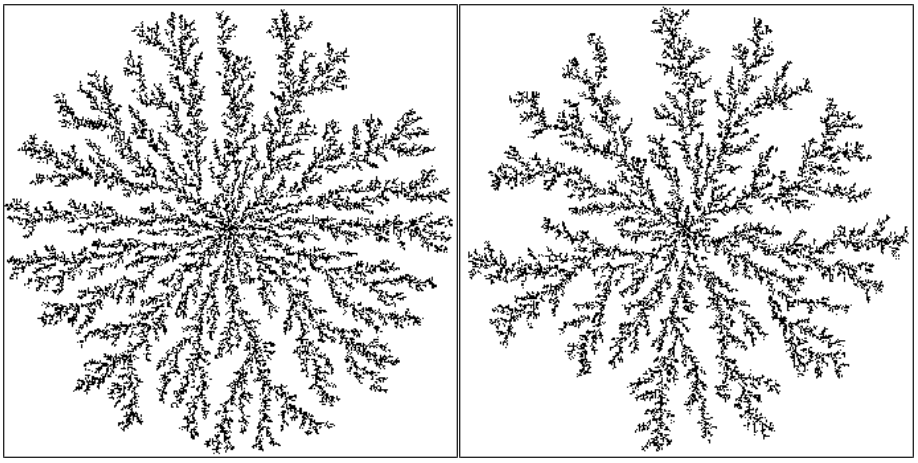

(a) (b)

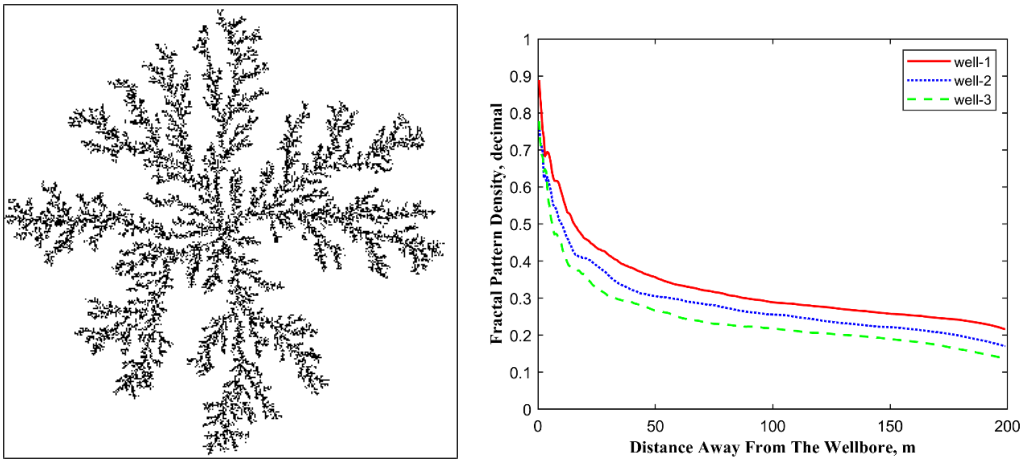

(c) (d)

Figure 4.6 Fractal patterns for (a) well-1, (b) well-2, (c) well-3 and (d) density of fractal patterns for three wells.

4.2.3 Relative Permeability Model

The three-phase relative permeability curves for three wells are formulated, and the curves for the three wells, are shown in Figure 4.7. Given the uncertainty in the perforation layer and reservoir quality for each well, the relative permeability curves are adjusted based on production histories. Irreducible water saturation S_{wi} is tuned to match the water production, while S_{gc} is used as a tuning parameter for matching the producing GOR.

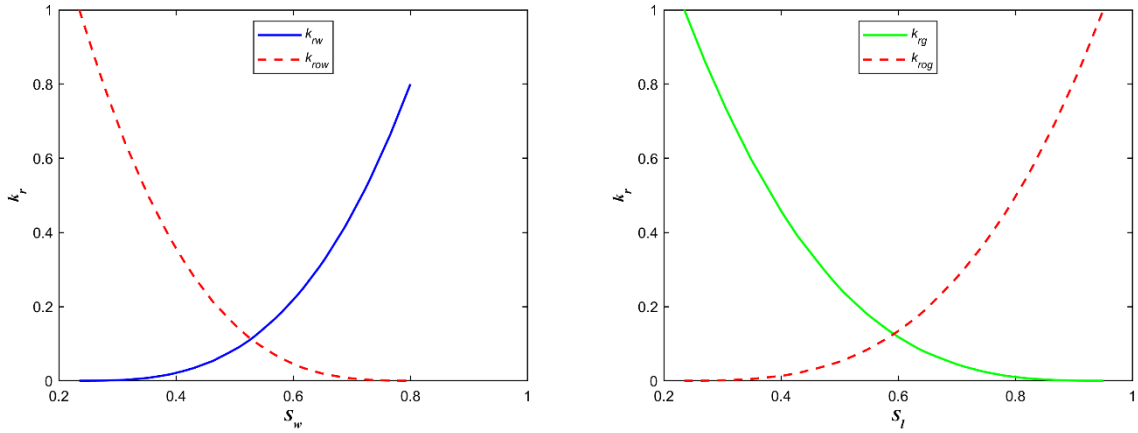

(a) (b)

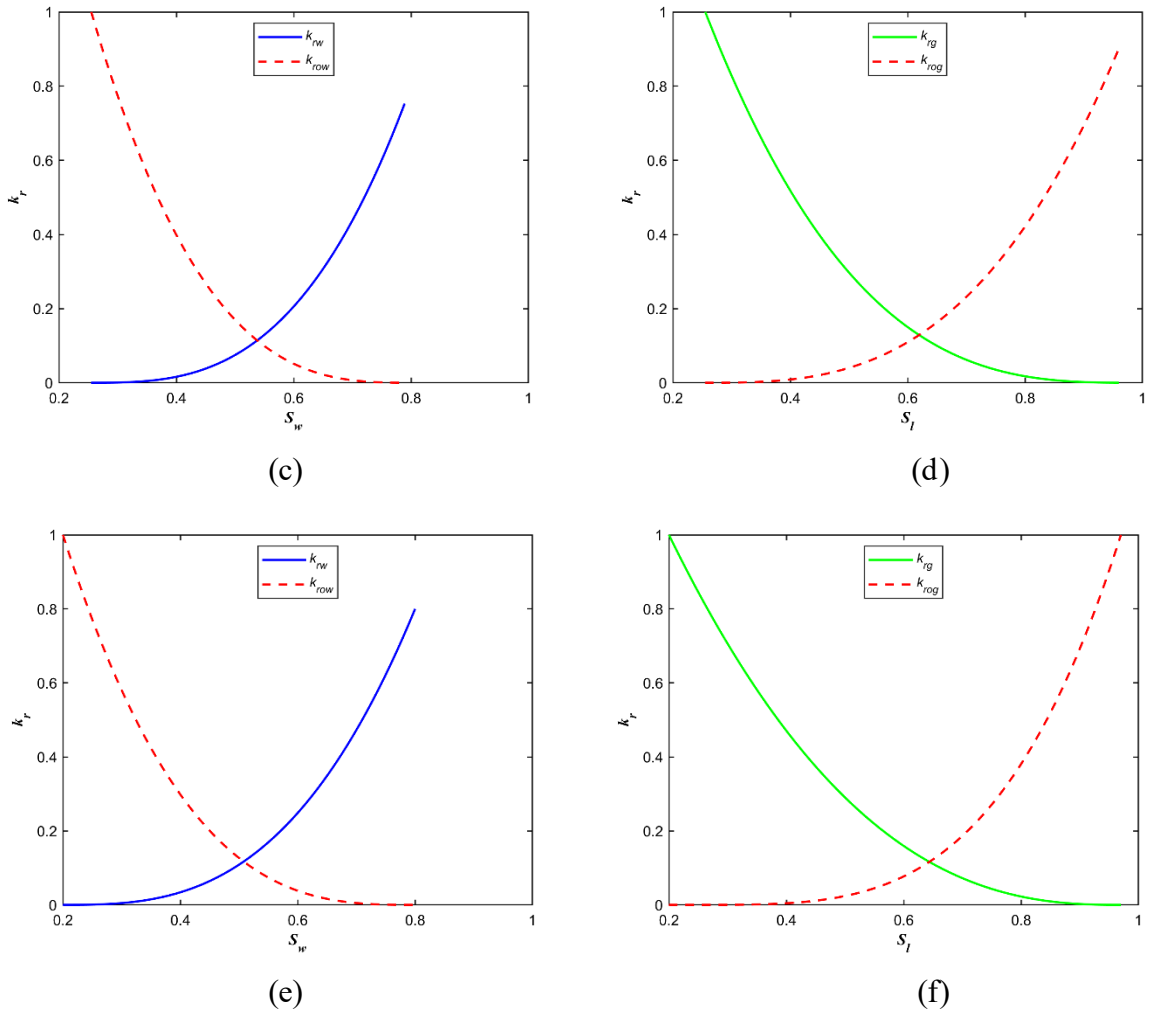

Figure 4.7 The relative permeability curves for: (a) well-1 oil-water system, (b) well-1 gas-liquid system, (c) well-2 oil-water system, (d) well-2 gas-liquid system, (e) well-3 oil-water system and (f) well-3 gas-liquid system.

4.3 Injection and Production Strategy for CSI Processes

In Chapter 7, a follow-up to Chapter 6 is presented to represent the CSI process as a post-CHOPS technique for enhancing heavy oil recovery. The reservoir condition at the end of CHOPS illustrated in Chapter 6 is determined as the initial condition for subsequent CSI simulations. The data files for history-matching results of the CHOPS process are the parent files in CMG; any CSI processes are conducted in restart files based on these parent files. This section primarily summarizes the injection and production strategies used in this research for CSI.

Ideally, after 6 to 7 injection/production cycles in fields, the oil recovery would be equivalent to that of the primary process; that is, the final oil recovery factor would be doubled (Coskuner and Huang, 2020b) after 6 to 7 cycles of CSI. Given the high computational requirement (taking more than 100 hours for one cycle on average in each well), only three injection/production cycles are conducted for each well in this study. In the base case, the production period is 6 months, the injection period is 1 month and the soaking period is 7 days in each cycle. Pure CO_2 as the solvent is injected into the reservoir in CSI. Standard (surface) conditions are 15 °C and 101.325 kPa. The well constraints for different periods and wells are shown in Table 4.3.

Wells	Injection Period		Production Period		
	Gas Injection Rate (std m^3/day)	Maximum BHP (kPa)	Maximum Gas Rate (std m^3/day)	Maximum Oil Rate (std m^3/day)	Minimum BHP (kPa)
Well-1	30000	3000	30000	20	500
Well-2	9000	3000	9000	11	500
Well-3	5000	3000	5000	10	500

Table 4.3 Well constraints in different periods and wells.

An attempt is commonly made to re-pressurize the reservoir to the initial reservoir pressure level (3,000 kPa) in each cycle before the well is put on production. The solvent injection and maximum oil rates are specified according to the different production histories for each well. Based on the piloting observations (Coskuner and Huang, 2020b) from some wells with good performance in the CHOPS process, the maximum oil rate in each CSI cycle approaching the oil peak in the CHOPS process when the well was put on production and then declined to the end of the cycle. The injection and production rates for gas and oil are the primary constraints for each well until the BHP constraint is reached and the rates decline.

CHAPTER 5: AN IMPROVED MODEL FOR CHOPS SIMULATION

In the model proposed by Yu and Leung (2020), a set of realistic 2D fractal wormhole patterns was generated by the DLA algorithm. Each fractal pattern used in a simulation was discretized with a locally-refined mesh. It was updated dynamically by coupling a three-phase multi-component flow simulation with a sand arch failure criterion: the wormhole network would expand following the fractal pattern only if the pressure gradient at the tip exceeded a threshold specified in the sand arch failure criterion.

In addition to generating a wormhole network that follows a fractal pattern, sand arch failure and fluidization mechanisms were controlled by the sand arch stability constraints. However, several limitations of this model should be noted. (1) The kinetic model for gas exsolution did not properly capture the characteristics of foamy oil behaviour. The previous model did not predict the trend of increasing producing GOR due to pressure depletion and free gas production at later times. (2) A calibration of the proposed model against a wider range of field histories (different CHOPS production profiles) was lacking. In particular, tuning the wormhole network growth rate during different periods of CHOPS production (e.g., early, middle and late times) to match the trends of oil and sand production rates was not carried out. For example, Tremblay and Oldakowski (2002; 2003) reported that the wormhole network would propagate relatively quickly initially, and then its rate of growth would slow down gradually over the rest of the life of the well. A more effectively calibrated CHOPS model is important for calculating its end state, which is also the initial condition for any post-CHOPS analysis (Chang and Ivory, 2015).

The purpose of this chapter is to develop an improved capability for simulating CHOPS production performance, enabling an improved representation of reservoir conditions at the end of

CHOPS to be established, i.e., an improved set of initial conditions for simulating the performance of potential post-CHOPS recovery technologies. In particular, this would lay the foundation for improved simulation studies of solvent-based processes for post-CHOPS recovery, such as CO_2-based cyclic processes (Chen and Leung, 2021; Chen et al., 2020).

Therefore, a few modifications and novel aspects are introduced in this chapter: (1) An improved foamy oil model is used and tuned. Two kinetic reactions are used to simulate the nucleation and coalescence processes. (2) The wormhole propagation speed is controlled by adjusting the time step size (a smaller timestep size can be used to simulate a more rapid propagation). The results indicate that these modifications enhance the model flexibility, and facilitate more control over matching producing GOR and sand production profiles. (3) Sensitivity to domain size is tested (i.e., size of the simulation grid). (4) The effect of multiple layers containing a wormhole network on production performance was investigated. The purpose is to investigate the effects of the vertical pressure gradient, including the effect of gravity, on production behaviour and wormhole growth within a given horizontal layer.

5.1 Tuning Parameters

The following tuning parameters are adjusted for the improved model: time step size for wormhole advancement rate (dr/dt), critical pressure gradient ($(dp/dr)_{cr}$), Kozeny constant (c), exponent in velocity-dependent factor (exp), reaction frequency factor (r_{ms}), reference oleic Darcy velocity (v_{ref}), critical oleic phase Darcy velocity (v_{crit}), reaction frequency factors (r_{CH4b} & r_{CH4g}) for the foamy oil model, irreducible water saturation (S_{wi}) for water production and critical gas saturation (S_{gc}) for gas production (i.e., producing GOR).

A smaller maximum time step is typically needed to match early production data from CHOPS wells when the wormhole network is advancing relatively quickly; at later times when the rate of wormhole advancement becomes slower, the maximum time step should be increased to accommodate this. In this study, an initial maximum time step of 1 day was selected after some sensitivity analysis for the first 20 days of the simulation (i.e., dr/dt was limited to a maximum of 0.5 m/day) when the oil production rate was ramping up along with the pressure gradient near the tip of the advancing wormhole network. Following this preliminary stage, a maximum time step of 0.5 days was selected for the next 100 days to accommodate the period of most rapid wormhole network growth while the oil production rate was at a peak (i.e., dr/dt could reach a maximum of 1 m/day). For the following 30 days, a maximum time step of 1.5 days was selected after the oil production had peaked, the wormhole growth rate would slow down (i.e., dr/dt was limited to a maximum rate of 0.33 m/day). Next, a maximum time step of 15 days was selected for the subsequent 7 months (i.e., dr/dt was limited to a maximum rate of 0.033 m/day). Finally, after the first year, it was assumed that the wormhole would grow even more slowly during the remainder of the simulation period, so the maximum time step size was 30 days. The selections of maximum time step size during different production periods are summarized in Table 5.1.

Periods (days)	Time step size (days)	dr/dt (m/day)
0-20	1	0.5
21-121	0.5	1
122-152	1.5	0.33
153-367	15	0.033
368-941	30	-

Table 5.1 Timestep selections for wormhole propagation speed at different periods for Chapter 5.

The final values of parameters in the sand arch failure criterion and the sand fluidization model that were tuned in this simulation study and the previous study by Yu and Leung (2020) are displayed in Table 5.2. Several factors were considered for tuning these parameters based on the study by Yu and Leung (2020). Firstly, the values of the parameters $(dp/dr)_{cr}$ and v_{ref} were adopted from the previous study (Yu and Leung, 2020). In this study, these values were reasonable. The effects of changing $(dp/dr)_{cr}$ was explored in this study, but this parameter had only a marginal effect on the simulation results for the range of $(dp/dr)_{cr}$ that was investigated (+/- 50% from the base value). The parameter v_{ref} in the sand production provides a velocity scale for the dimensionless velocity-dependent factor (v_{eln}). It acts as an amplifier for the reaction rate for transforming solid sand to mobile sand when v_n is slightly greater than v_{crit}. Secondly, an initial estimation of v_{crit} is made by tuning Eq. 3-13 to match the experimental observations by Tremblay et al. (1997). This selected value of v_{crit}, 0.013 m/day, is smaller than the selection, 0.025 m/day, in the study by Yu and Leung (2020). A smaller v_{crit} means more sand can be fluidized in the simulation, resulting in more sand production, particularly during the initial stage of CHOPS.

Finally, the wormhole network would often extend to 80-100 m out from the well after only a few months of CHOPS, eventually to 200 m out from the well (Sawatzky et al., 2002). However, it is observed that in the previous work (Yu and Leung, 2020), the wormhole network only extends to 60 m away from the well at the end of CHOPS. Attempts are made in this study to allow a more extensive wormhole network to be generated by the simulation at the end of CHOPS. This requires a relatively persistent sand production throughout the CHOPS compared to the study by Yu and Leung (2020). To achieve this and balance the impact of the lower v_{crit}, a smaller rate of sand mobilization should be given. Thus, r_{ms} goes down. Moreover, as mentioned in Section

3.1.5, *exp* is a dimensionless exponent ≥1; so, increasing local oil Darcy velocity would increase local sand velocity. Particularly during the initial stage when the local oil Darcy velocity is very high near the well block, the rate of sand production is very sensitive to the value of *exp*. A final value of 1.055 was selected to accommodate the sand production during the first few months. This is lower than the value of *exp* selected by Yu and Leung (2020). The Kozeny constant (c) determines the wormhole permeability directly. If c is too large (i.e., if the wormhole permeability is too small), the simulation cannot keep up with the oil production rate. It was found that the value of c listed in Table 5.2 was the largest value of c that could be used to match the oil production rate in the simulations. This is slightly smaller than the value of c used in the study by Yu and Leung (2020). The rate of sand production is also sensitive to the rate of wormhole advancement (i.e., to the selection of time step size). This is discussed in detail in Section 5.2.

Parameter	$(dp/dr)_{cr}$ (kPa/m)	r_{ms} (day^{-1})	v_{crit} (m/day)	v_{ref} (m/day)	exp	c (Darcy^{-1})
This study	68	0.0001	0.013	0.0002	1.055	1.5×10^{-5}
Yu and Leung (2020)	68	0.0004	0.025	0.0002	1.100	2.0×10^{-5}

Table 5.2 Final values of tuned parameters in the sand arch failure criterion and the sand fluidization model.

The final values of the parameter values in the foamy oil model that were tuned in this simulation study are displayed in Table 5.3. The high viscosity of heavy oil hinders the growth and coalescence of dispersed bubbles by slowing the diffusion of dissolved gas and dispersed bubbles (Maini et al., 1993; Uddin, 2005; Okazawa, 2009; Busahmin et al., 2017). Given the high viscosity of heavy oil in this CHOPS well (41,790 mPa·s at 20°C), a much lower value is assigned for bubble coalescence (r_{CH4g}) than the value chosen by Yu and Leung (2020).

Parameter	r_{CH4b} (day^{-1})	r_{CH4g} (day^{-1})
Value	0.143	0.00143

Table 5.3 Final values of tuned parameters in the kinetic model representing nonequilibrium gas exsolution behaviour.

5.2 Effect of Selections of Time Step Size

As discussed in Section 3.1.4, the time step size is used to adjust the advancement rate of wormholes due to the discretized nature of the model. The wormhole network can advance no more than one block at each time step; this restriction may artificially limit the rate of wormhole network growth. Therefore, it is observed that the smaller the time step size, the more rapid the rate of wormhole advancement, resulting in a higher sand production rate. As field sand production rates are higher during the initial stage of CHOPS, smaller time step sizes were selected for the initial periods of the simulations.

Three cases were run to probe the effect of time step size; i.e., the advancement rate of wormholes. The selection of time step size for three cases is listed in Table 5.4.

	Case 1		Case 2		Case 3 (Table 5.1)	
Periods (days)	Time step size (days)	dr/dt (m/day)	Time step size (days)	dr/dt (m/day)	Time step size (days)	dr/dt (m/day)
0-20	1	0.5	0.5	1	1	0.5
21-121	1	0.5	0.5	1	0.5	1
122-152	1.5	0.33	1.5	0.33	1.5	0.33
153-367	15	0.033	15	0.033	15	0.033
368-941	30	-	30	-	30	-

Table 5.4 Different selections of time step size.

The historical oil production peaked around 120 days, which indicates that wormholes propagated rapidly during this period. The effect of dr/dt is primarily explored during this stage.

As illustrated in Table 5.4, case 1 was run with a maximum advancement rate of 0.5 m/day in the first 4 months, while case 2 exhibits a faster wormhole propagation, 1 m/day. Case 3 is the final selection for model validation in Section 5.3. All other parameters and settings remain consistent. Note that after 367 days (i.e., one year), the rate of wormhole advancement slows considerably; the wormhole network does not advance at every time step. Therefore, the value of (dr/dt) is not listed in Table 5.4 because it is no longer dependent only on the time step size.

The simulation results of oil rate, sand rate, cumulative sand production and BHP variation are shown in Figure 5.1. Given that the wormhole advancement rate was slower in case 1, the well was constrained at a minimum BHP of 200 kPa to produce oil and sand throughout the course of CHOPS. The wormhole network is much less developed at the end of CHOPS compared to the other two cases, as illustrated Figure 5.2. Note that cases 2 and 3 exhibit identical selections of time step size after 20 days. Therefore, the oil and sand production rates for cases 2 and 3 in Figure 5.1 (a), (b) and (c) are nearly the same; the wormhole network is slightly more extensive in case 2 than case 3 at the end of CHOPS. The selection of time step sizes in case 3 was finally adopted, somewhat arbitrarily, for the model in this study.

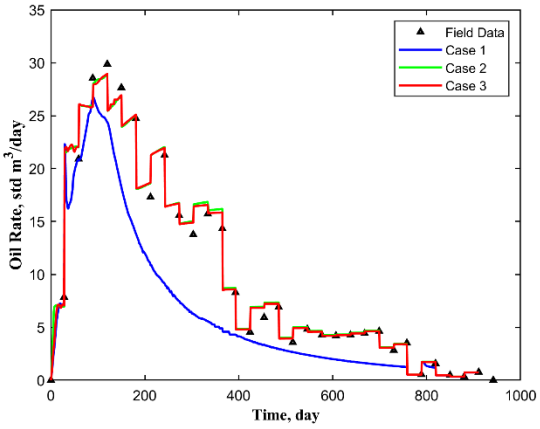

(a)

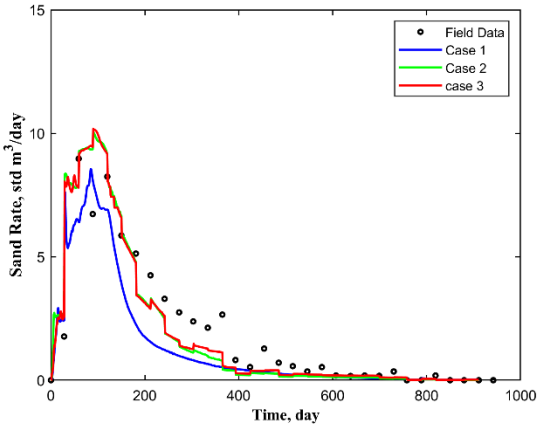

(b)

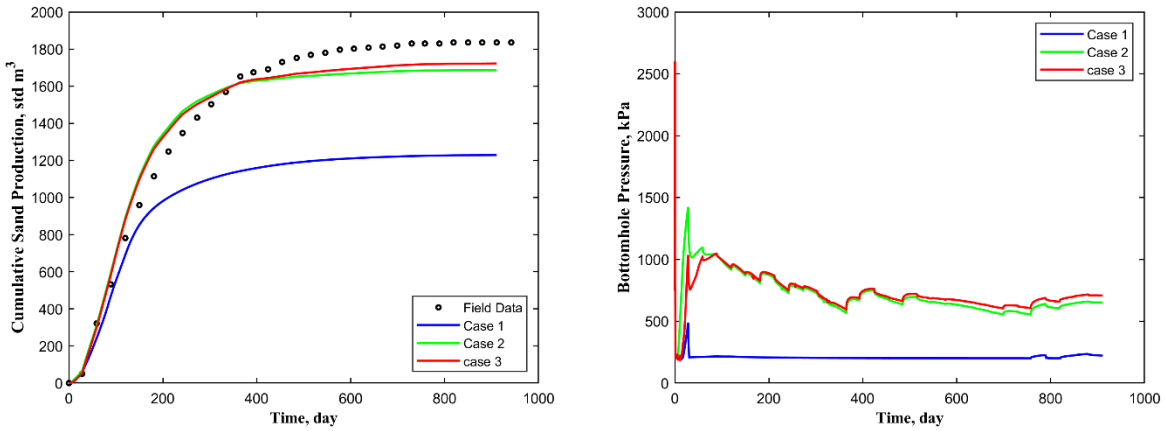

(c) (d)

Figure 5.1 Simulation results of three cases for different time step selections (a) dead oil rate; (b) sand rate; (c) cumulative sand production; and (d) BHP variation.

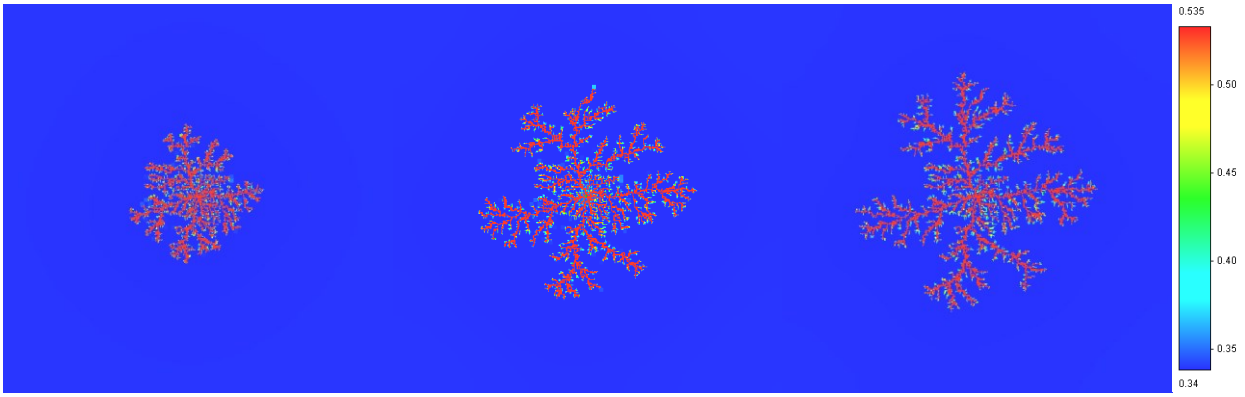

(a) (b) (c)

Figure 5.2 Aerial view of the porosity distribution for (a) case 1; (b) case 2; and (c) case 3.

5.3 Model Validation

The CHOPS production profiles generated in this study were compared to those generated in the previous study by Yu and Leung (2020). The well in the previous study was primarily constrained by a constant value of BHP, 500 kPa, throughout the course of the CHOPS. As discussed in Section 4.1.3, the primary well constraint in this study was the oil production rate. Two options for assigning the rate constraint were tested (see Table 5.5). In this study, a history match was performed by minimizing the differences between simulation predictions and other components of

the field production data (e.g., sand production). The producing GOR and BHP trends were also analyzed.

Case #	Input Approach	Curve Color
1	Constant rate	Red
2	Moving average over 3 months with weekly ramp-ups between data points (i.e., smoothed data in Figure 4.4)	Blue
3	Constant BHP (Yu and Leung, 2020)	Green

Table 5.5 Data assignment details of the three cases.

5.3.1 Oil and Sand Production

The simulation predictions for the three cases indicated in Table 5.5 were compared against the field data in Figure 5.3. Figure 5.3 (a) shows that the field oil production rate could be captured by the simulations in both cases 1 and 2 when the well was constrained by the total oil rate. As illustrated in Figure 5.3 (b) and (c), the oil and sand production rates were higher in case 1 than in case 2 during the first four months of production because the total oil production rate for the well constraint was slightly higher in case 1 than in case 2 (Figure 5.3 (a)). Eventually, the cumulative sand production for case 1 was approximately 20% higher than in case 2, but the initial sand production trend for case 2 was aligned more with the field data before 240 days, as indicated in Figure 5.3 (d).

Compared to cases 1 and 2, the simulated oil production rate in case 3 gradually deviates from the field data after 400 days. That is, the previous study by Yu and Leung (2020) cannot adequately capture the historical oil production during the late production times of CHOPS. Additionally, as illustrated in Figure 5.3 (c), the simulated sand production rate in case 3 was more than 30% higher than the field data and the two other cases at the peak of sand production. Subsequently, a lower sand production rate occurred in case 3 during the middle production period

of CHOPS than in cases 1 and 2. The simulation results demonstrate that the improved model in this study provided a better match to the field production data for this well than in the simulations presented in the previous study (Yu and Leung, 2020).

Figure 5.4 shows the porosity distributions corresponding to cases 1 and 2. This represents the development of the wormhole network over time. After the first four months, the wormhole network has extended to ~ 68 m away from the well, eventually extending to 72 m from the well. This demonstrates that slow, but persistent, wormhole network growth is necessary to improve the representation of oil and sand production rates during the middle and later stages of CHOPS.

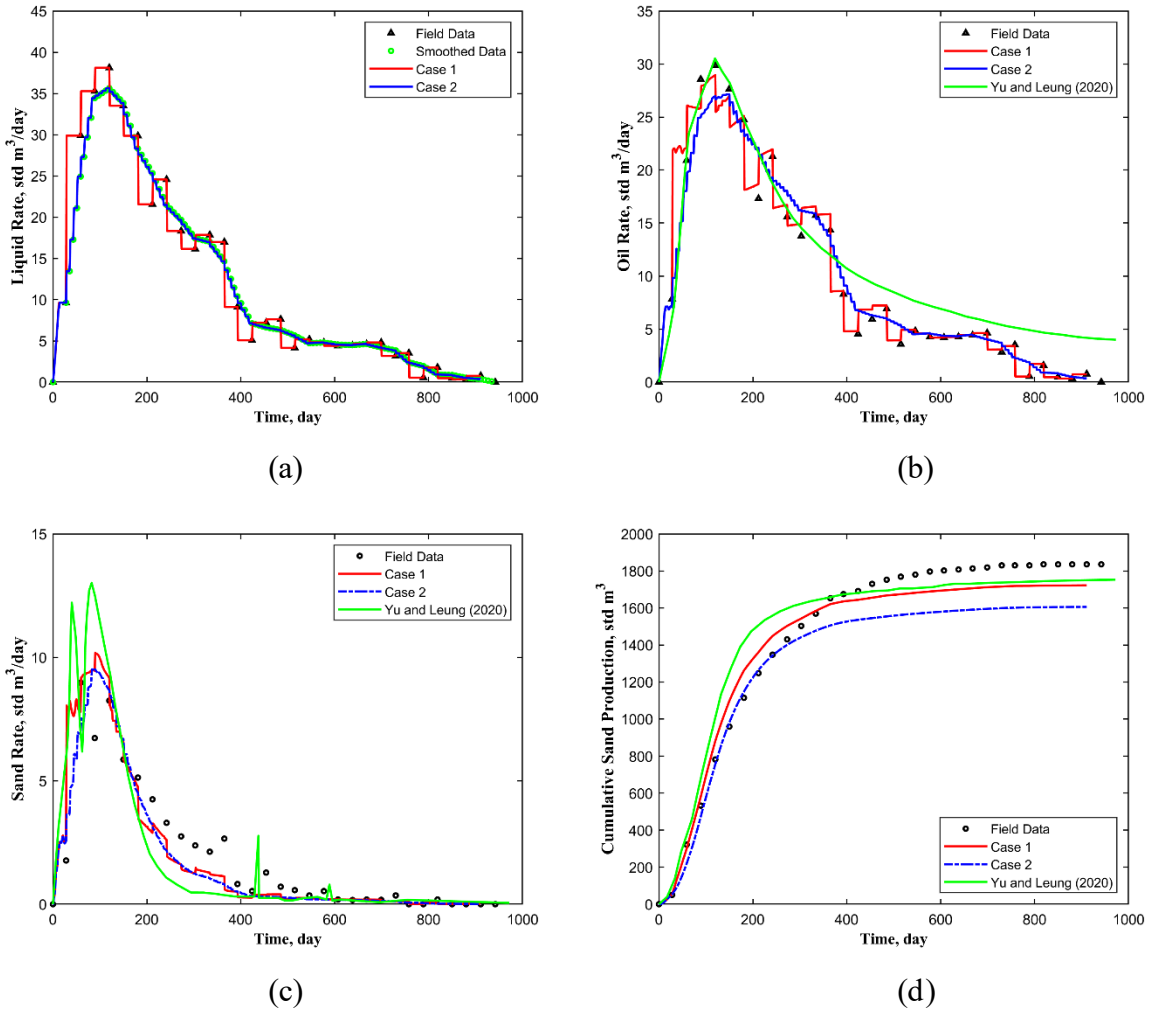

Figure 5.3 History match results: (a) total oil (dead oil + sand) rate; (b) dead oil rate; (c) sand rate; and (d) cumulative sand volume.

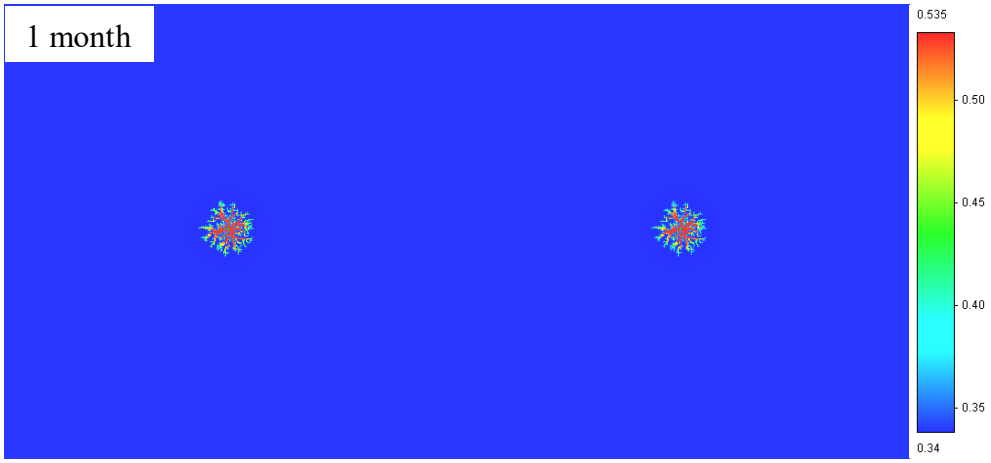
1 month
0.535
0.50
0.45
0.40
0.35
0.34

(a) (f)

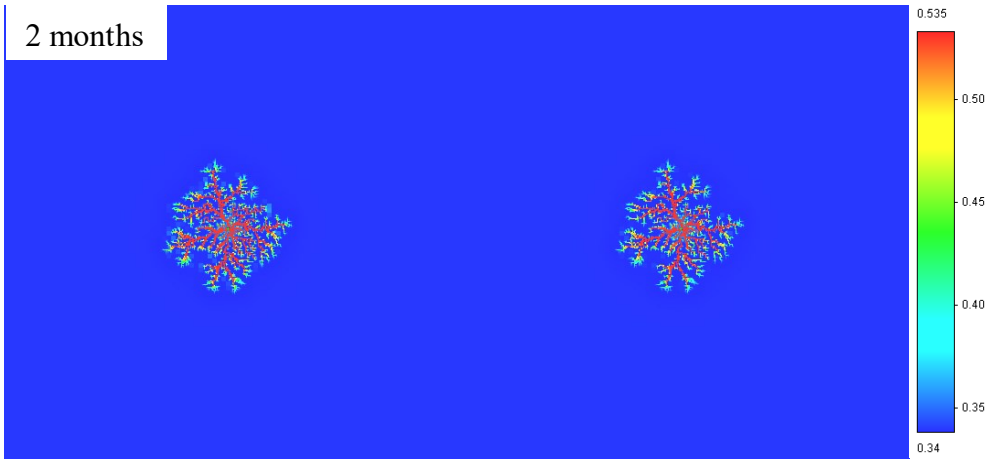
2 months
0.535
0.50
0.45
0.40
0.35
0.34

(b) (g)

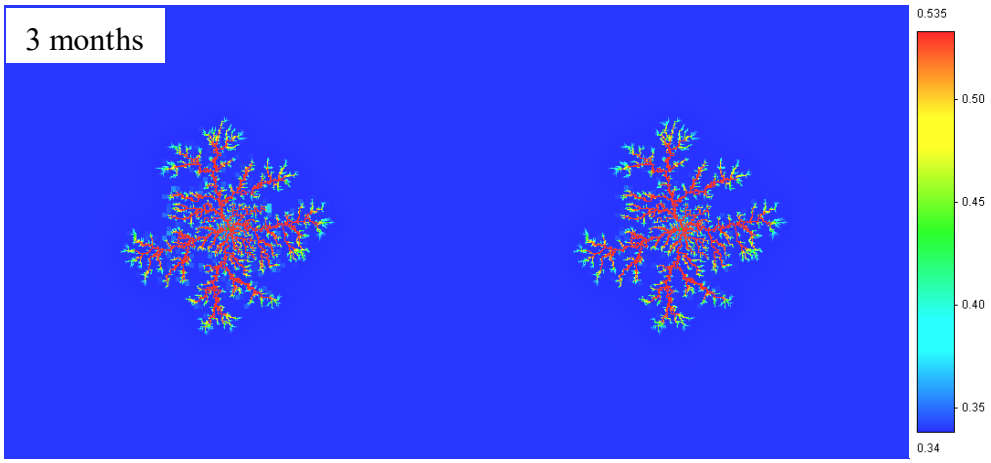
3 months
0.535
0.50
0.45
0.40
0.35
0.34

(c) (h)

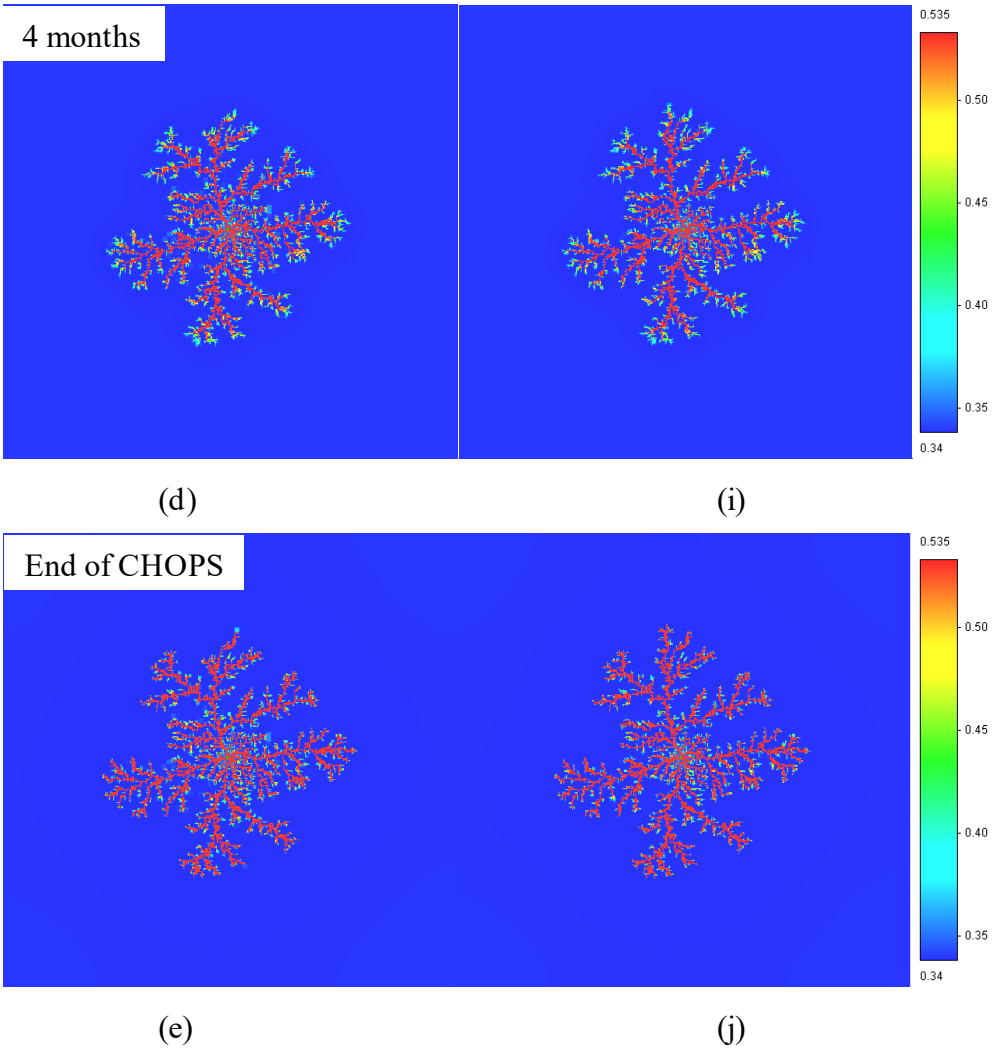

Figure 5.4 Aerial view of the porosity distribution for the two cases at different times: case 1 (a) – (e) and case 2 (f) – (j).

5.3.2 Producing GOR and Gas Production

Figure 5.5 illustrates the producing GOR and gas production over time. Although the gas production trends downwards, the producing GOR trends upwards in both cases. Fewer fluctuations are observed for case 2 than in case 1, as a result of the smoothing of the oil production rate constraint in case 2. It is evident that the foamy oil behaviour in the simulation model delays the release of free gas (coalescence of dispersed bubbles), as illustrated by a relatively low initial producing GOR followed by increasing levels during later stages.

In the simulation results from the previous study (Yu and Leung, 2020), case 3 in Figure 5.5 (a), the characteristics of foamy oil flow mentioned above are not reflected. The relatively low rates of gas production imply that the simulated gas saturation in the reservoir in the study by Yu and Leung (2020) would be lower than the simulated gas saturation in the reservoir in this study. This will impact the simulated performance of potential post-CHOPS recovery technologies, such as cyclic solvent processes.

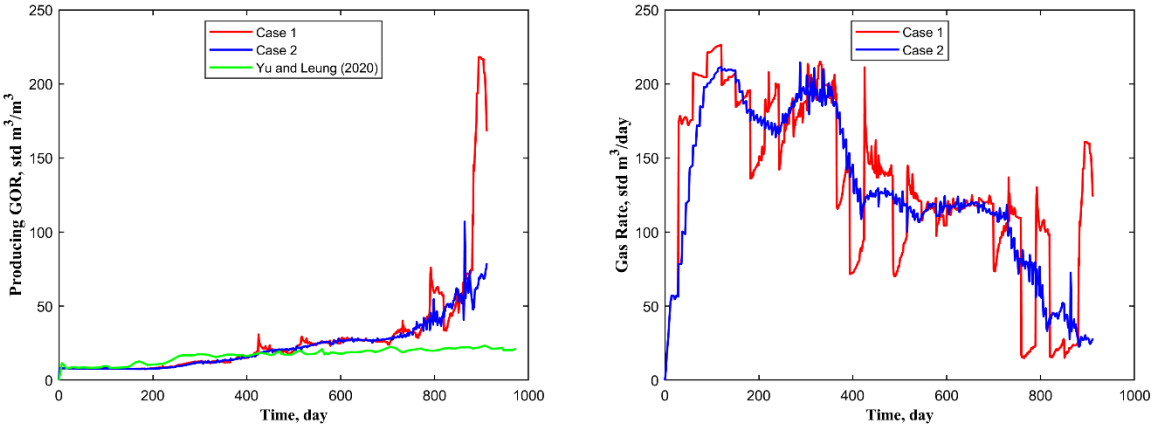

(a) (b)

Figure 5.5 Simulation predictions: (a) producing GOR and (b) gas rate.

The produced gas at surface conditions is composed of *CH4s*, *CH4b*, and *CH4g* (Figure 5.6). As reservoir pressure declines, more *CH4s* is converted to dispersed bubbles that coalesce into *CH4g*. Much of the produced gas originates from the *CH4s* and *CH4b* when the CHOPS well is experiencing relatively rapid wormhole growth during the early stage. Starting from approximately 150 days, more *CH4g* is produced, while the production of *CH4s* and *CH4b* is reduced (Figure 5.6). The *CH4g* is responsible for much of the gas production after 360 days. Given that the gas is more mobile, the oil production rate starts to decline as the *CH4g* breaks through at the well.

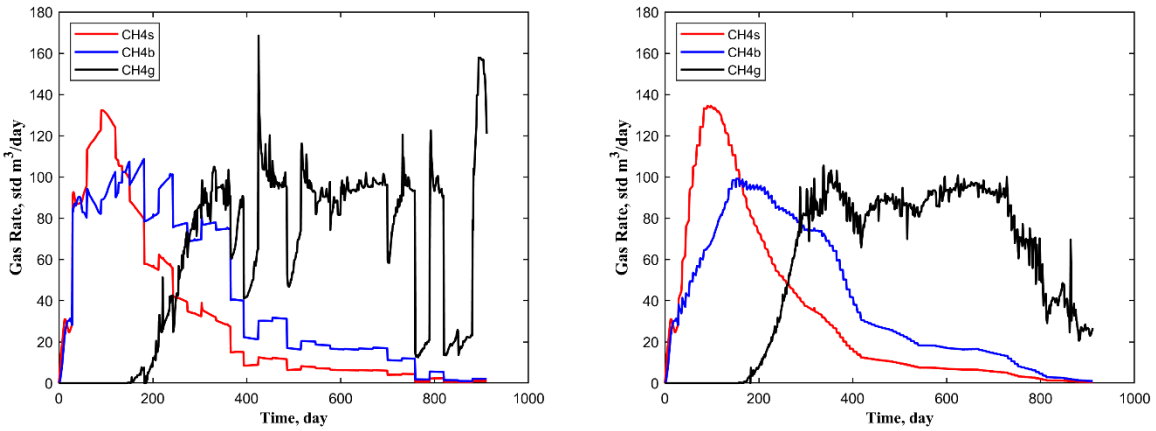

Figure 5.6 Simulated production profiles of the three gas components: (a) case 1 and (b) case 2.

5.3.3 Water Production and BHP

Figure 5.7 (a) compares the simulation results for the water production rate in this study (two cases) with the water production rate in the study by Yu and Leung (2020) and the historical water production data. The simulation predictions for the two cases in this study are similar and much lower than the historical values. Similar conclusions were reported by other simulation studies, including Istchenko and Gates (2012) and Fan et al. (2019). In the study by Yu and Leung (2020), a higher water production rate was observed than in two cases in this study during the early stage of the CHOPS (where there was a peak in water production), but then it fell to the same level as the simulated water production rate in this study. Istchenko and Gates (2012) suggested that there could have been a water zone in the area near the CHOPS well. As the wormhole network generated in the field approached this water zone, the increasing pressure gradient between the tip of the wormhole network and the water zone could enable the water to move through the reservoir into the wormhole network and the well at increasing rates. Istchenko and Gates (2012) did not introduce a water zone into their model due to a lack of field data identifying the location of the water zone. Therefore, they were not able to test their hypothesis. Similarly, given the lack of field

data regarding the existence and location of a water zone, a hypothetical water zone was not introduced in this simulation study.

Dusseault (2006) stated that water coning is a particularly difficult issue in CHOPS because of the high well drawdowns needed to sustain sand influx and to maximize the foamy oil effect. It has been noted in the field that even in cases of no free water detected in offset wells for a 500 m distance, lateral coning can still take place. If there is a water layer right near (under- or over-laying) the oil zone and the oil viscosity is greater than 100 mPa·s, it is usually impossible to avoid coning (Dusseault, 2006), and water breakthrough may happen early, shortly after putting the well into production (Qin and Wojtanowicz, 2009). Therefore, given the high oil viscosity (41,790 mPa·s at 20 °C) in this CHOPS well, if there is a water zone in the area near the well, it would be hard to avoid coning and resulting in increasing water production rates that were observed in the production history.

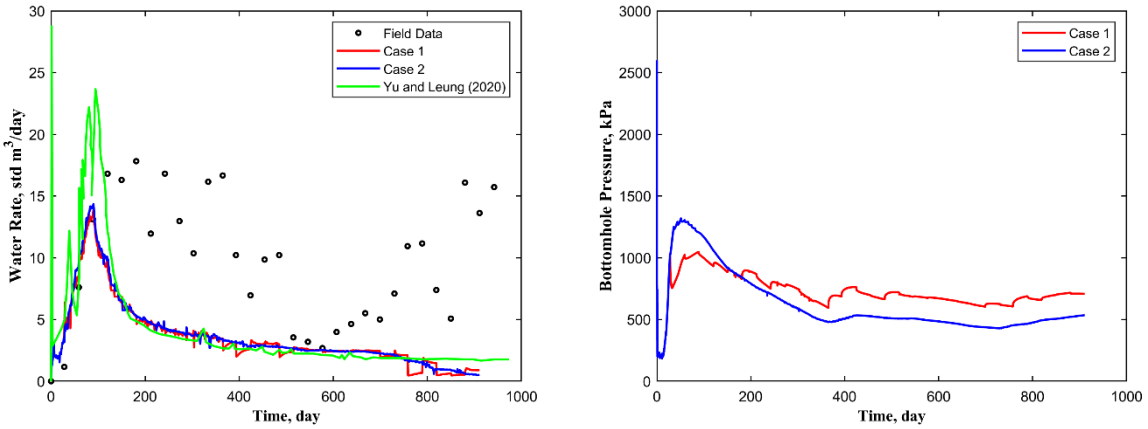

(a) (b)

Figure 5.7 (a) Water production profile and field data and (b) Variation of BHP.

The BHP variations in the two cases are presented in Figure 5.7 (b). BHP drops rapidly from 3,000 kPa to 200 kPa in both cases, and several factors may contribute to this behaviour. First, the well production increases abruptly from zero to a finite level at $t > 0$. Second, no high-

conductivity channel network has yet been developed. Interestingly, such a huge pressure drop offers a favourable condition for the generation of foamy oil; Maini (1999) and Yrigoyen and Carvajal (2001) reported that an aggressive drawdown schedule is advantageous to foamy oil formation. The initial steep pressure drop in the reservoir offers a strong driving force for bubble nucleation and coalescence (Uddin, 2005). The BHP then rises quickly from 200 kPa to nearly 1,000 kPa for case 1 and 1,300 kPa for case 2 over the next two months. This is the consequence of the rapid bubble nucleation and coalescence during this period. Additionally, the relatively rapid wormhole network growth increases the conductivity of the reservoir near the well, providing a secondary contribution to the rising BHP. After a period of rapid bubble nucleation and coalescence, these processes begin to slow down, resulting in a steady decrease in BHP.

5.4 Domain Size Sensitivity Test

The wormhole network often extends to 80-100 m out from the well after only a few months of CHOPS, but thereafter the growth rapidly slows down. Usually, the wormhole network continues to grow but much more slowly. Eventually, it could extend to 200 m out from the well (Sawatzky et al., 2002). It was observed in the previous work (Yu and Leung, 2020) that the pressure gradient in the grid blocks far away from the wellbore was very small. Thus, this region contributes insignificantly to the oil and sand production. Therefore, an investigation was carried out to determine if a smaller reservoir grid than the one used by Yu and Leung (2020) could adequately represent the production behaviour in this CHOPS well. Two different domain models (i.e., reservoir grids) were built. The smaller domain was 250 m by 250 m with a discretization of 100 by 100 grid blocks (i.e., each grid block was 2.5 m by 2.5 m in the horizontal directions), while the large one was 400 m by 400 m with 160 by 160 grid blocks in the horizontal directions (the same as in the previous study by Yu and Leung (2020)); the horizontal grid block size was left

unchanged. Both cases were run with a BHP constraint of 500 kPa. All other parameters were assigned to have the same values as in case 1 in Section 5.2.

Figure 5.8 illustrates the oil and sand production profiles. The results were similar for both cases. Figure 5.9 compares the pressure maps and wormhole networks at the end of CHOPS for each case. The results suggest that the drainage area in the two cases was nearly identical. The pressure drop in the reservoir beyond 250 m away from the wellbore was very small. This is not surprising, since the wormhole network only extended to approximately 78 m away from the wellbore, as shown in Figure 5.9 (c) and (d). Therefore, the smaller simulation domain was used in this study to build to achieve faster runtimes in the simulations.

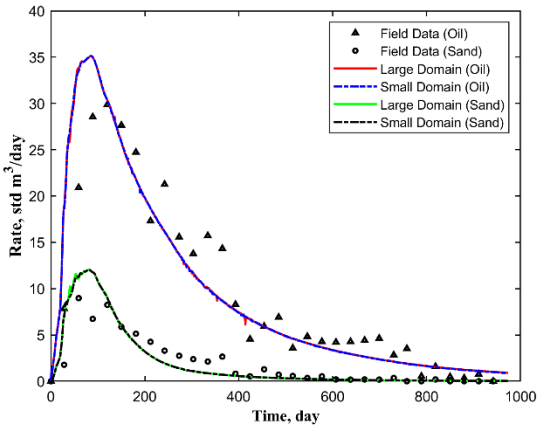

Figure 5.8 Oil and sand production profile for the two models with varying domain sizes.

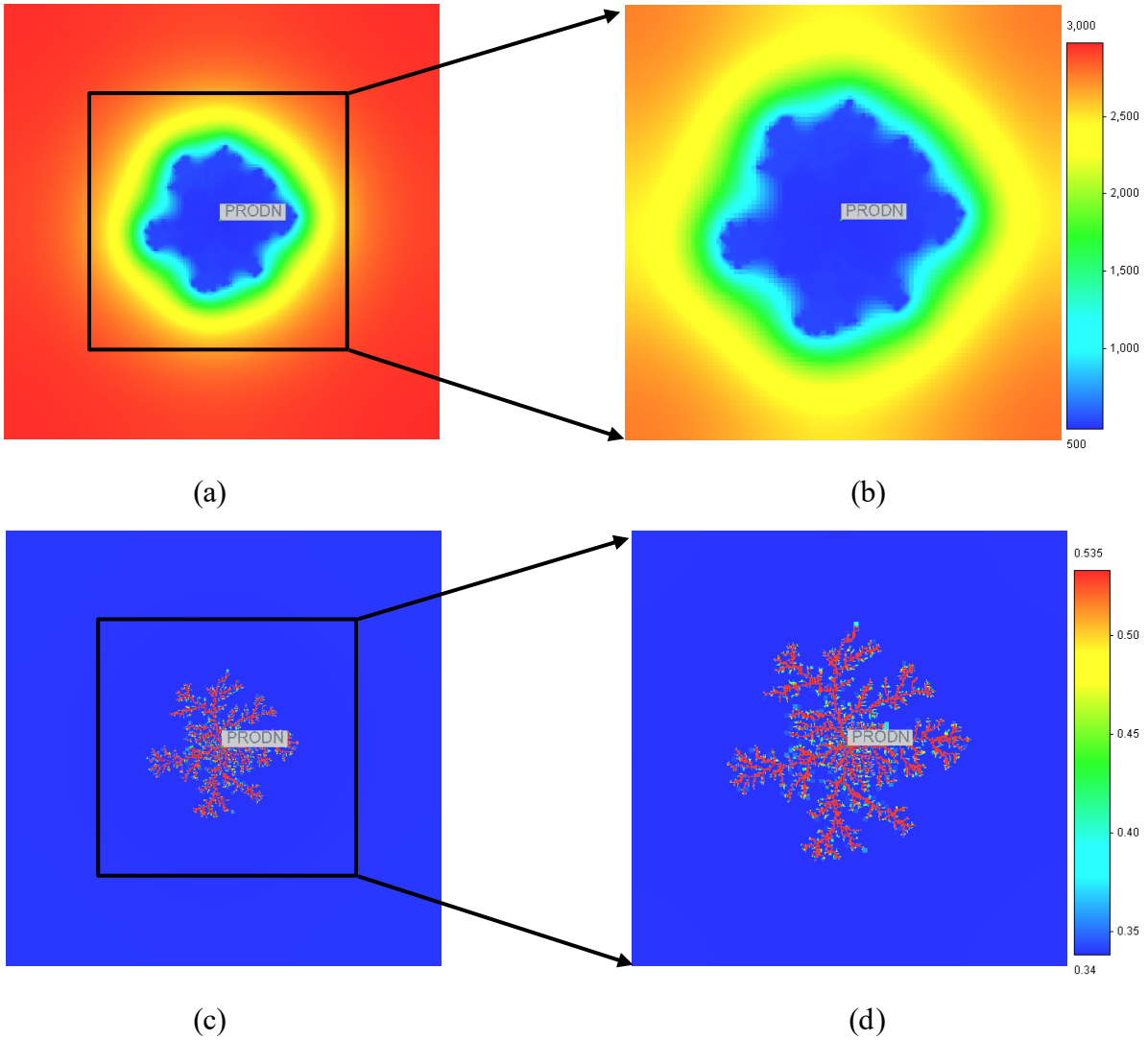

Figure 5.9 Pressure distribution at final time step: (a) large domain case and (b) small domain case. Porosity distribution at final time step: (c) large domain case and (d) small domain case.

5.5 Multi-layered Wormhole Network System

In Section 3.1.4, the conditions that are necessary for wormholes to propagate are discussed in detail. The key factor is the critical pressure gradient. If the pressure gradient at the wormhole tip exceeds the critical pressure gradient, the wormhole will keep growing. In Lloydminster-area heavy oil reservoirs, the combination of a thin pay thickness and high oil viscosity leads to a primarily horizontal pressure gradient under primary production. In addition, due to the depositional processes in these reservoirs, the horizontal permeability is much larger than the

vertical permeability. Therefore, it is reasonable to assume that the wormholes tend to grow within individual layers in the reservoir, even in thin reservoirs.

5.5.1 Double-Layered Wormhole Network System

This section analyzes a 3D reservoir consisting of more than one 2D wormhole pattern (e.g., two). The objective is to investigate the effects of vertical pressure variation on production performance and wormhole growth. Based on their sand-pack experimental studies, Tremblay and Oldakowski (2002) reported that the pressure at the top orifice was slightly lower than that at the bottom orifice, leading to a higher pressure gradient at the top than at the bottom. As a result, the wormhole length was much greater (5× longer) at the top than at the bottom. Considering that such huge differences were observed at the laboratory scale, it is interesting to test in this simulation study whether or not a slight vertical pressure variation could lead to observable differences in wormhole growth behaviour at the field scale.

In this section, the pay thickness (3.5 m) is divided into two layers with an equal thickness (1.75 m each): "M-1" (top) and "M-2" (bottom). Both "M-1" and "M-2" are perforated and the same fractal pattern (as illustrated in Figure 4.1 (b)) is implemented in both layers. The well is constrained by a minimum BHP of 500 kPa. All other parameters are the same as the single-layered model in case 1 in Section 5.3.

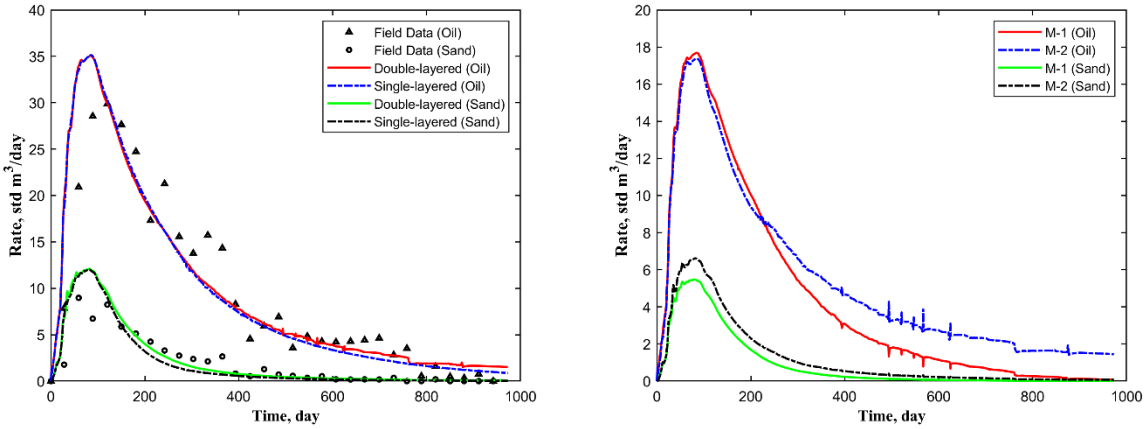

(a) (b)

Figure 5.10 (a) Dead oil and sand rate in the single- and double-layered cases; (b) Dead oil and sand rate in each layer for the double-layered case.

The total oil and sand production rates are nearly identical for both cases. However, the profiles in each layer appear to be quite different, particularly at the later stages (e.g., $t > 240$ days), as illustrated in Figure 5.10 (b). There is a significant pressure drawdown horizontally, driving fluid flow laterally within the layer into the wellbore. However, as the reservoir pressure declines, the pressure gradient along the horizontal direction is reduced, so that gravitational effects begin to play a secondary role. This drives some oil from "M-1" into "M-2", resulting in more oil being produced from "M-2". More fluidized sand is also dragged into "M-2" and produced. The wormhole network and pressure distributions at the end of the CHOPS simulation are shown in Figure 5.11. The difference between the two layers is minimal.

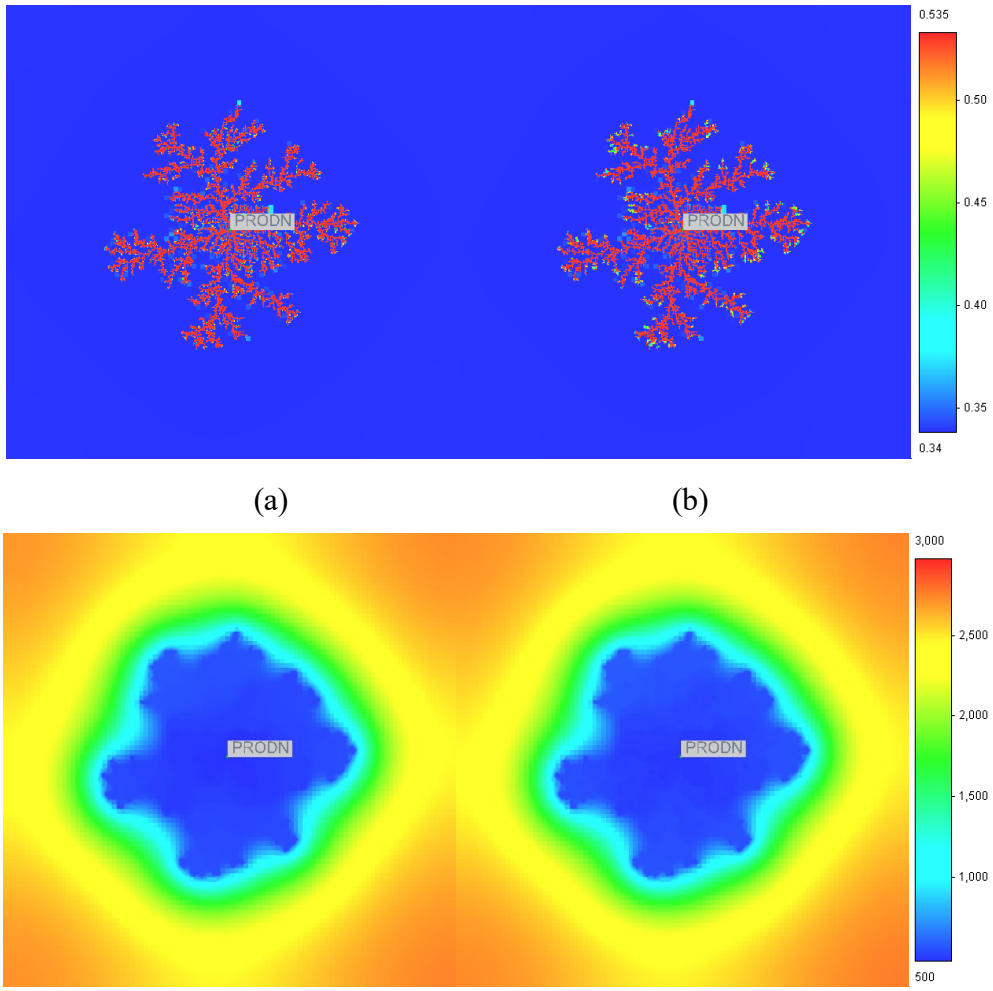

Figure 5.11 Porosity distribution at final time step: (a) "M-1" and (b) "M-2"; pressure distribution at final time step: (c) "M-1" and (d) "M-2".

The vertical pressure variation between the two layers is less than 20 kPa throughout the CHOPS process. The results of these simulations indicate that the differences between the two layers are relatively insignificant. This implies that a single-layered system is likely sufficient for performing field-scale simulations.

5.5.2 Effect of Gravity

Expanding the study in the previous section, in this case the pay thickness (3.5 m) is divided into three layers: "M-1" (top, 1.2 m), "M-2" (Middle, 1.1 m) and "M-3" (bottom, 1.2 m). All these

layers are perforated. The well is constrained by a minimum BHP of 500 kPa. All other parameters are the same as the single-layered model in case 1 in Section 5.3. Two cases, case 1 and case 2, were run to investigate the effect of gravity as the pay thickness is subdivided into thinner layers. The same fractal pattern (as illustrated in Figure 4.1 (b)) is implemented only in "M-2" in case 1, and in "M-1" and "M-3" in case 2, as illustrated in Figure 5.12. The case with all three layers containing a potential wormhole network is not carried out here. This is because Section 5.5.1 demonstrates that the simulation results are consistent in both a double-layered and a single-layered system. It is unlikely that the simulation results would be any different for triple-layered system.

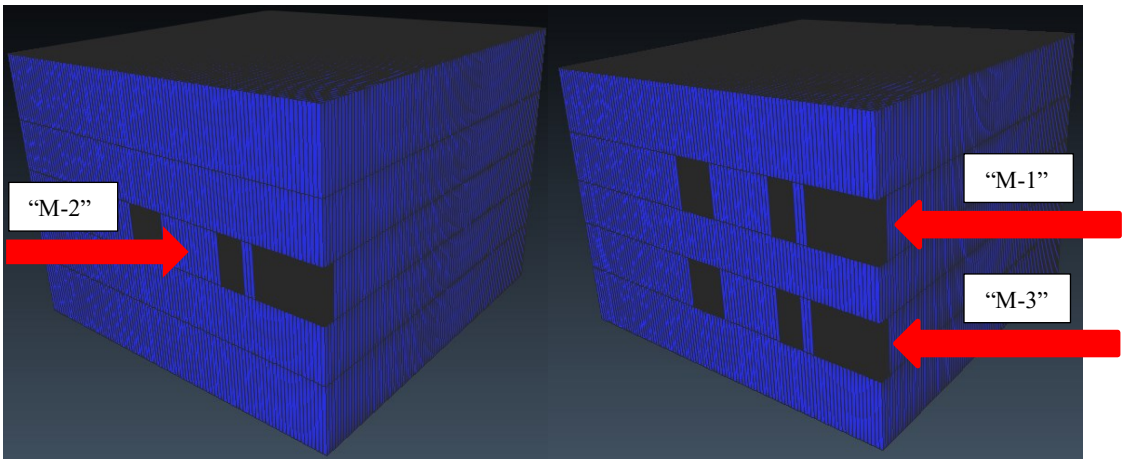

(a) (b)

Figure 5.12 The implementation of the fractal pattern in different layer(s) in (a) case 1 (b) case 2; and (c) case 3.

The oil and sand rates in the two cases are displayed in Figure 5.13, along with the single-layered case shown in Section 5.5.1. The simulation results indicate that fewer layers employing fractal patterns result in lower oil and sand production. In case 1, where the layer containing the wormhole network is much thinner (by a factor of three) than the original case, the oil and sand production rates are reduced. One possibility for this behaviour is that the vertical thickness of the wormhole cells is much smaller (by a factor of three) than in the original case, likely leading to

lower oil and sand flow rates through the wormhole cells. In case 2, where the total vertical thickness of the two layers containing wormhole networks is two-third of the thickness of the wormhole layer in the original case, the reduction in oil and sand production rates is not large.

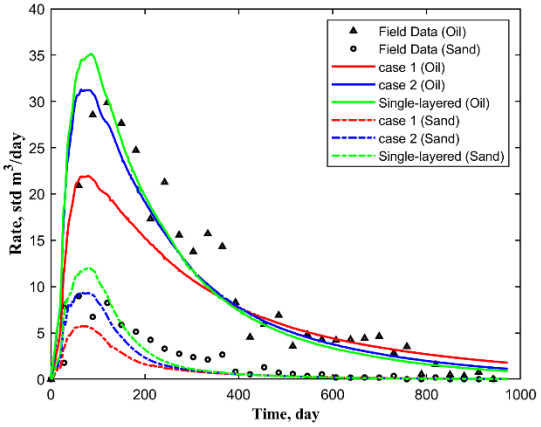

Figure 5.13 Simulation results of the two cases and single-layered system.

The oil and sand production rates in each layer for cases 1 and 2 are shown in Figure 5.14. As the wormhole network exists only in one layer in case 1, "M-2" is the dominant contributor to the oil and sand production, as illustrated in Figure 5.14 (a). Similarly, in case 2, there is essentially no oil and sand production from the layer "M-2" as it does not contain a wormhole network. This is illustrated in Figure 5.14 (b).

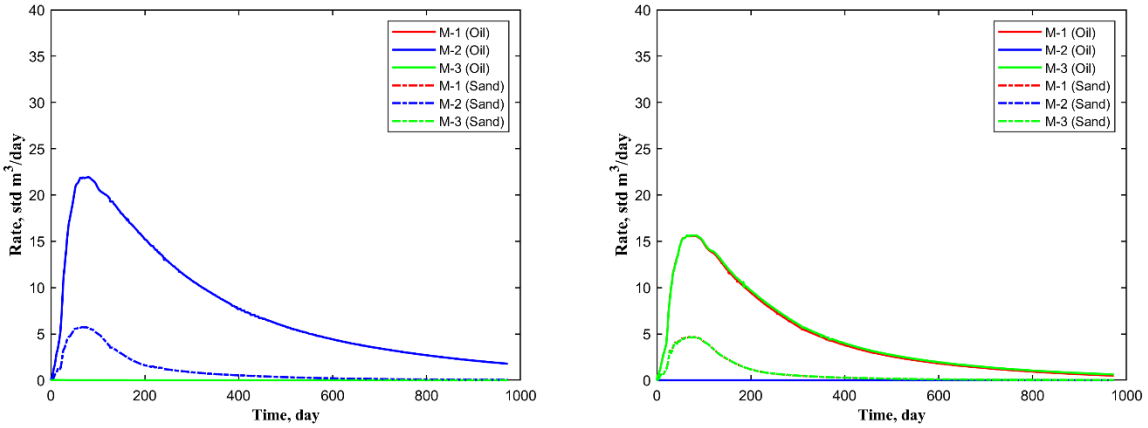

(a) (b)

Figure 5.14 Dead oil and sand rates in different layers for (a) case 1; and (b) case 2.

On the other hand, Figure 5.14 (b) illustrates that oil and sand production rates from "M-1" and "M-3" are essentially the same in case 2, implying that the effects of gravity are negligible in these simulations. The horizontal pressure gradient provides the dominant drive. As illustrated in the double-layered system in Section 5.5.1, where the wormhole network is developed in both layers, gravity plays a secondary role only when the pressure gradient in the horizontal direction becomes sufficiently small.

5.6 Summary

- A model of dynamic wormhole growth coupled to a multi-component flow simulator was modified from a previous study (Yu and Leung, 2020) to improve the simulations of the CHOPS process. Several parameters in the sand production model were tuned to adjust the simulated sand production rate to match the field sand production rate better, particularly, the peak sand production and subsequent declining sand production. For example, the parameter *exp* was reduced in this study to reduce the sand production rate during the initial stage of CHOPS production. It was found that the parameters contained in the sand production model were not independent; the effects of these parameters on the simulated CHOPS production were mutually dependent. Therefore, a number of iterations were required (i.e., changes to the set of parameters) to achieve an acceptable match to production. Similarly, parameters in the foamy oil model were tuned to adjust the trend in the simulated producing GOR to match the increasing producing GOR, a common characteristic of production from CHOPS wells. In the study by Yu and Leung (2020), the simulated producing GOR did not show this trend; it remained relatively flat with time. Associated with the higher producing GOR in this study is the increased gas saturation in the reservoir at the end of CHOPS than predicted by Yu and Leung (2020). This difference

in the level of the gas saturation in the reservoir at the end of CHOPS will influence the simulated behaviour of subsequent post-CHOPS technologies, such as cyclic solvent processes.

- History matching of a CHOPS well was performed in this study. The monthly oil rate data was used as a primary constraint. A reasonable match to sand production and reasonable trends in BHP and producing GOR was achieved. Water production was not matched as well after the initial period of CHOPS, as discussed in Section 5.3.3. The simulated results for the sand production rate and producing GOR in this study were an improvement compared to the previous study by Yu and Leung (2020). This results in an improved representation of reservoir conditions at the end of CHOPS.
- The wormhole propagation rate was controlled in the simulation model in this study by adjusting the time step size used in the coupling module. Smaller time steps were used initially to facilitate more rapid wormhole growth during the early production stage. Larger time steps were used later when the wormhole network growth slowed down. This way of controlling the wormhole network growth rate was important for matching the production behaviour in the CHOPS well.
- The simulation results obtained from two cases with different domain sizes indicated that a smaller domain (250 m by 250 m) is sufficient to simulate the production from the CHOPS well in this study.
- Studies were performed to investigate the impact of the vertical block size on the simulation results. When the wormhole layer in the base case was divided into two, the oil and sand production profiles for the double-layered wormhole network system were the same as for the single-layered case. In the double-layered case, there were small differences

in production between the two layers. These were mainly caused by gravity drainage from the upper layer to the lower layer. However, these differences did not impact the model's total oil and sand production. This implies that a single-layered wormhole network system was sufficient to simulate the production from the CHOPS well in this study.

- Continuing of the studies to investigate the impact of the vertical block size on the simulation results, a multi-layered (i.e., triple-layered) wormhole network system was considered. In this case, the base case's wormhole layer was divided into three layers. In one variation, the wormhole network was only present in the middle layer. In the second variation, the wormhole network was present in the top and bottom layers. When the wormhole network was only present in the middle layer, the oil and sand production rates were somewhat lower than in the base case. This indicates that the thickness of the grid blocks in the wormhole layer could impact the oil and sand production rates. When the wormhole network was only present in the top and bottom layers, the oil and sand production rates were nearly the same as in the base case. This indicates that the oil and sand production rates are not very sensitive to the thickness of the grid blocks in the wormhole layer. Further, the results of both variations in the study indicate that the oil and sand production in the simulations is primarily driven by the pressure gradient in the wormhole layer(s). There is little production, if any, from the layers that do not contain a wormhole network.

CHAPTER 6: A FIELD CASE STUDY FOR THE IMPROVED MODEL

Chapter 5 has offered a number of improvements to enhance model flexibility: (1) An improved foamy oil model was used and tuned. Two kinetic reactions were used to simulate the nucleation and coalescence processes. Parameters in the foamy oil model were tuned to adjust the trend in the simulated producing GOR to match the increasing producing GOR. (2) The wormhole propagation speed is controlled by adjusting the time step size (a smaller timestep size can be used to simulate a more rapid propagation). The results indicate that these modifications enhance the model flexibility, and facilitate more control over matching producing GOR and sand production profiles. (3) Several parameters in the sand production model were tuned to adjust the simulated sand production rate to match the field sand production rate better, particularly, the peak sand production and subsequent period of declining sand production. However, several limitations of this modified model should be noted when further investigation was carried out for the feasibility of effectively simulating a variety of production and flow behaviours associated with CHOPS wells: (1) The sand production model in Chapter 5 could simulate a large amount of sand production at the initial stage, followed by a sharp decline. It failed to effectively capture a wider range of sand production behaviours over the entire CHOPS production phase. (2) The model did not provide options for different fractal patterns when simulating the potential wormhole growth paths.

Therefore, this chapter introduces a few key modifications to the workflow originally developed by Yu and Leung (2020) and subsequently modified in Chapter 5. The goal is to enhance the modelling flexibility for simulating a variety of production and flow behaviours associated with CHOPS wells. In particular, three CHOPS wells from Dee Valley in the Lloydminster area

with vastly different characteristics were selected to investigate how the improved CHOPS model could match field histories. The novel modifications are: (1) A time-dependent division factor available in STARS was employed in the sand production model to offer additional flexibility in capturing a range of sand production profiles. (2) A fractal pattern generation code was added such that different fractal patterns could be assigned for different wells to be more compatible with their oil and sand production histories.

6.1 Tuning Parameters for History Matching

The following tuning parameters are adjusted in this study to capture the production and flow behaviours of the three new CHOPS wells: time step size for wormhole advancement rate (dr/dt), critical pressure gradient ($(dp/dr)_{cr}$), Kozeny constant (c), exponent in velocity-dependent factor (exp), critical oleic phase Darcy velocity (v_{crit}), coefficients in division factor (coefficients A and B), reaction frequency factors (r_{CO2b} and r_{CO2g}) for the foamy oil model, irreducible water saturation (S_{wi}) and critical gas saturation (S_{gc}) for each well.

Time step selections for wormhole advancement rate were shown in Table 6.1. The same selected timestep sizes were applied for all three wells. The steady sand production profiles in Figure 4.5 (c) suggest that the wormhole network may continuously propagate throughout the CHOPS process. As shown in Table 6.1, the advancement rate is assigned to decrease gradually with time so sand production can be maintained at a certain level. Additionally, a lower critical pressure gradient $(dp/dr)_{cr}$ is thus given to facilitate the growth of the wormhole network (Table 6.2).

Periods (days)	Time step size (days)	dr/dt (m/day)
0-15	1	0.5
16-410	1.5	0.33
411-775	2	0.25
776-987	4	0.125
988-1505	8	0.0625
1506-1686	30	-

Table 6.1 Timestep selections for wormhole propagation speed at different periods for Chapter 6.

The final values of the sand fluidization model parameters for all three wells are displayed in Table 6.2. Permeability in wormholes is calculated by using the updated porosity (Eq. 3-14). The reduced sand production in this study compared to Chapter 5 leads to a greater selection of the Kozeny constant. As mentioned in Chapter 5, the parameter v_{ref} in the sand production provides a velocity scale for the dimensionless velocity-dependent factor (v_{eln}). It acts as an amplifier for the reaction rate when v_n is right above v_{crit}. Due to the low mobility of heavy oil, the selection of v_{ref} is an appropriate choice for a heavy oil system (Chapter 5). As mentioned in Section 3.1.5, *exp* is a dimensionless exponent ≥1, so increasing local oil velocity would increase local sand velocity. Sensitivity studies show that the rate of sand production is highly sensitive to the value selected for *exp* when it is slightly greater than 1. For this reason, it is set to be equal to 1 in this study to adjust the sand production.

Parameter	c (Darcy^{-1})	$(dp/dr)_{cr}$ (kPa/m)	r_{ms} (day^{-1})	v_{ref} (m/day)	exp
Value	6.5×10^{-5}	45	0.0001	0.0002	1

Table 6.2 The final values of tuning parameters for sand arch criterion and fluidization model.

Table 6.3 lists the final values of the sand fluidization model tuning parameters for each well. Compared to Chapter 5, the dead oil viscosity is an order magnitude less in this study (41,790

mPa·s and 5,000 mPa·s at 20 °C); the viscous force exerted on the sand particles is reduced, weakening the ability to drag sand particles flowing along with the oil toward the wellbore during the early stages. The reduction in dead oil viscosity will also lead to a larger v_{crit} (Eq. 3-13), which also means a reduction of the dragging forces. A reasonable range of 0.01~1 m/day is thus assumed for v_{crit} here.

Wells	v_{crit} (m/day)	*A*	*B*
Well-1	0.71	300	2.3
Well-2	0.47	300	2.3
Well-3	0.20	150	2.0

Table 6.3 The final values of the sand fluidization model tuning parameters for the three wells.

The foamy oil and relative permeability model parameters are shown in Table 6.4. Considering that the oil production in well-1 outperforms the other two wells (as mentioned in Section 4.2.1), a lower r_{CH4g} is used for well-1 to delay the formation of CO_2 free gas and extend the duration of foam oil flow, resulting in higher oil production in this well.

Wells	r_{CH4b} (day^{-1})	r_{CH4g} (day^{-1})	S_{wi}	S_{gc}
Well-1	0.215	0.0108	0.235	0.050
Well-2	0.215	0.0215	0.255	0.015
Well-3	0.215	0.0215	0.200	0.030

Table 6.4 The final values of tuning parameters for the foamy oil model.

6.2 Impact of Division Factor on Sand Production

Given that sand production profiles are highly dependent on the choice of coefficients *A* and *B* (as discussed in Section 3.1.5), a sensitivity analysis is conducted in this section to explore the impacts of coefficients *A* and *B*, and D_{ivn}, on the simulated profiles. Cases listed in Table 6.5 are only used to study the sensitivity of coefficients *A* and *B* in Eq. 3-11, and v_{crit} = 0.1 m/day is assigned for

all cases. D_{ivn} is equal to 1 in case 1. Results of sensitivity tests of the two coefficients are shown in Figure 6.1 and Figure 6.2.

Run	*A*	*B*	Run	*A*	*B*
Case 1	-	-	Case 7	1	5
Case 2	1	1	Case 8	1	10
Case 3	10	1	Case 9	100	2
Case 4	100	1	Case 10	100	5
Case 5	300	1	Case 11	100	10
Case 6	1	2			

Table 6.5 Parameters selected for coefficients *A* and *B*.

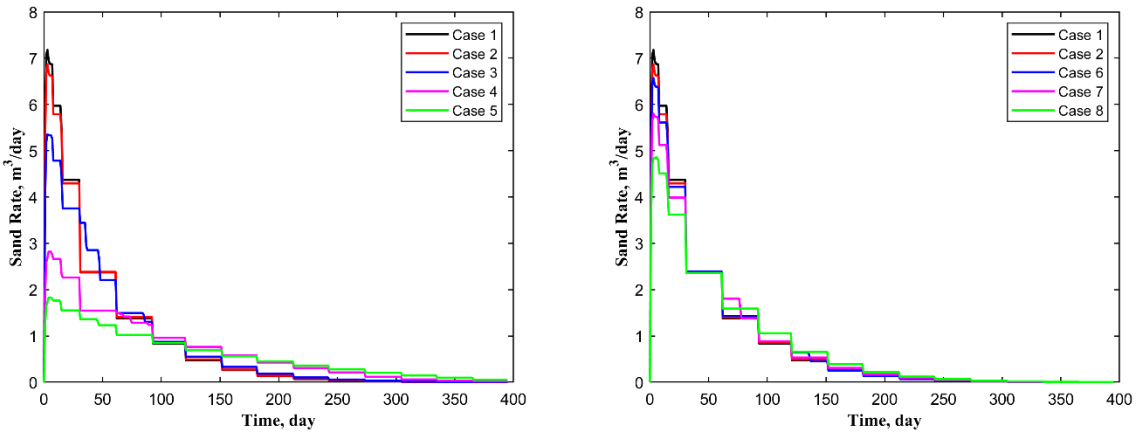

(a) (b)

Figure 6.1 Sensitivity of (a) coefficient *A* and (b) coefficient *B* to sand production.

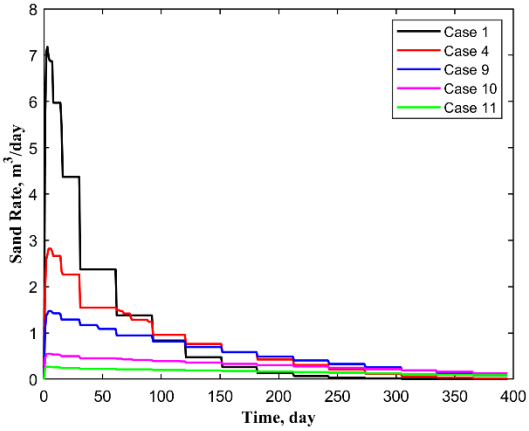

Figure 6.2 Sensitivity of coefficient *B* to sand production.

As shown in Figure 6.1, both coefficients A and B impact the sand rate during the initial stage of the production process, compared to the middle and late stages. The test results demonstrate that sand production is more sensitive to coefficient A than coefficient B, which is an exponential coefficient, in controlling sand mobilization at the initial stage. This is attributed to the relatively lower concentration of *Mobile Sand* in the oleic phase during the initial production stage compared to the middle and late stages. When $A = 1$, the impact of the magnitude of coefficient B on the division factor remains relatively insignificant. Despite varying coefficients A and B values, only slight elevations can be observed in the middle production stages in cases 4, 5, and 8.

However, if $A > 1$, increasing B would reduce sand production during the middle and late production times, as shown in Figure 6.2. As mentioned in Section 3.1.5, a more sustained sand production during the middle stage requires more solid sand to remain in the void space, i.e., higher C_{vn}, during the early stage. However, suppose either coefficient A or B is excessively large, especially if B is too large, the sand production would be strongly suppressed throughout the CHOPS process. The choice for coefficient B in cases 4 and 9 would yield higher sand rates at the middle production times than other cases are preferred. In the end, coefficient B is set to 2 (same as case 9) for the next stage of sensitivity analysis (Table 6.6), since a lower initial sand rate is observed in case 9.

The tests conducted above provide a preliminary range for selecting coefficients A and B without using the historical sand production data and the consideration of v_{crit}. It is thus desirable to conduct further tests for selecting coefficients A and B, as well as v_{crit} (Eq. 3-12), using historical data from well-1 as an example. Parameters for the next stage of testing are shown in Table 6.6. Parameters in case 5 are selected as the final tuning parameters for the simulation of

well-1. Cases 1 to 4 are used to probe the sand production at the initial stage. The results in Figure 6.3 indicate that as the coefficients A and B increase, v_{crit} can be set to a smaller value to match the historical data. If $D_{ivn} = 1$, achieving a similar result as case 5 in Figure 6.3 would require an unreasonably high v_{crit} to suppress sand mobilization during the initial production stage, and such large values may exceed the reasonable range (0.01~1 m/day).

Run	A	B	v_{crit} (m/day)
Case 1	100	2.0	1.50
Case 2	200	2.0	1.00
Case 3	200	2.0	0.50
Case 4	300	2.0	0.80
Case 5	300	2.3	0.71

Table 6.6 Parameter selections for sand production model.

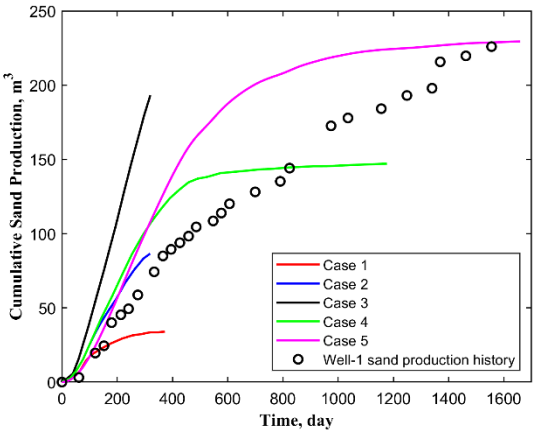

Figure 6.3 Sand production results under different parameter selections.

An evident discrepancy in the shape of the cumulative sand production profile can be observed between simulation results and the actual field data in case 5, as illustrated in Figure 6.3. Even after extensive parameter tuning, the sand production increases rapidly during the initial times compared to the field data. Subsequently, it declines at around 400 days, enabling the

ultimate cumulative sand production to match the field data. The field data does not reflect such a decline but represents a more stable or sustained sand production rate throughout the middle and late stages. A plausible reason can be postulated. Due to the uncertainty regarding the critical pressure gradient ($(dp/dr)_{cr}$) and the wormhole diameter (R_c), a constant average value of v_{crit} is considered. The simulator does not allow this value to be updated. However, physically, local oleic phase Darcy velocity (v_n) inevitably undergoes a significant increase in early time, caused by rapid pressure drawdown or wormhole activation, followed by a subsequent decrease as pressure depletes.

On the other hand, greater values of v_{crit}, such as in cases 1 and 2, results in a premature termination of wormhole network propagation and significantly reduces oil production compared to the field data. Smaller values of v_{crit}, such as in case 3, resulting in excessively rapid propagation of the wormhole network. Case 4 demonstrates that minor alterations in D_{ivn} and v_{crit} can have a significant impact on sand production. The goal of tuning these three parameters is to ensure the ultimate sand production approaching the field data while attempting to decrease the rate of sand production at the initial stage and maintain a stable rate at the middle and late times. The selections of case 5 allow the model to match the oil production behaviour with a reasonable wormhole advancement rate (Section 6.3). The simulation results demonstrate that if the initial sand rate is too low, the wormhole network is not propagating fast enough and the predicted oil production would be too low compared to the historical oil production, despite drawing down aggressively by keeping BHP at its minimum.

The same sensitivity tests of the division factor are carried out for well-2 and well-3, and the final tuning parameters are shown in Table 6.4. It is possible to further adjust *A, B,* and v_{crit}

to better match the history but given the lower viscosity of heavy oil in this study, an order of magnitude greater than Chapter 5 may be reasonable.

6.3 History Matching Results

Like in Chapter 5, the wells are simulated using rate constraints, estimated or smoothed with a 3-month moving average of the actual monthly production data. In other words, instead of using the actual monthly production rate from the field data, a 3-month average is assigned to a particular month. To further facilitate a more gradual (realistic) ramp-up and decline, the rate constraint is assigned on a weekly (1/4 of a month) basis, where the production rate for a particular week in a month is linearly interpolated between the monthly rates of the current month and the next month.

Simulation results of the oil rate and cumulative sand production for the three wells are profiled against the field data in Figure 6.4. Simulated predictions of oil production match the field successfully for all three wells. As discussed in Section 6.2, attempts are made to match the simulation results with the trend observed in actual field data.

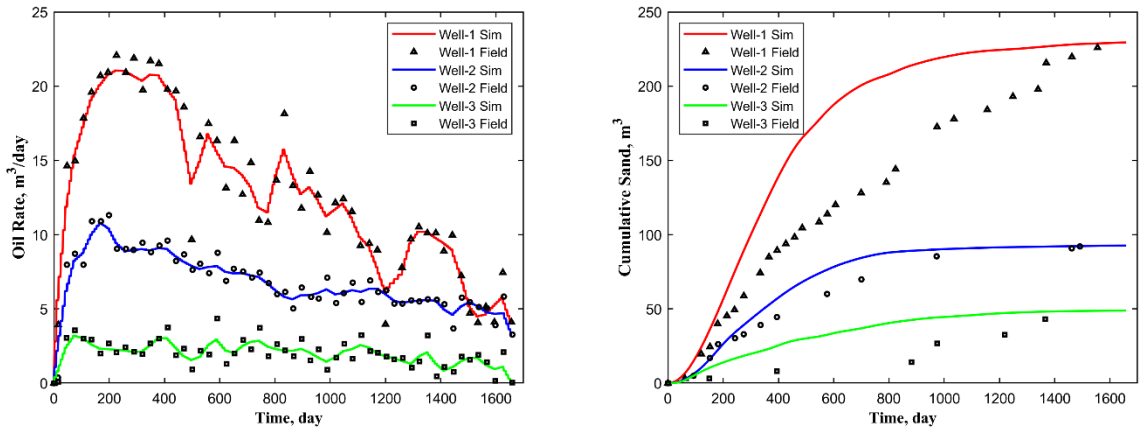

(a) (b)

Figure 6.4 Simulating results of (a) oil rate and (b) cumulative sand production for all three wells.

Simulated cumulative water production profiles for the three wells are compared with the field data in Figure 6.5. The final values of S_{wi} for different wells listed in Table 6.4 are selected after some sensitive analysis. Steep increases in the cumulative profile for well-1 imply rapid jumps in pressure, as discussed in Section 4.2.1. A possible reason is that the well is shut in because of well operations, resulting in a temporary reservoir pressure build-up. Upon reopening the well, the increased pressure gradient causes an increase in both oil and water production. The simulation results do not capture the rapid changes in water production, which are likely the result of fluctuating BHP that is unknown. Simulation results in well-2 and well-3 matches the actual field data better than well-1 as no such jumps are observed in the historical profiles.

Typically, gas production is sensitive to pressure variation due to its nature of compressibility. However, the slight compressibility of oil and incompressibility of water (assumed in this study) enable the system highly sensitive to the liquid production volumes. Besides, sand and oil production in well-2 are higher than in well-3. It is thus hypothesized that more wormholes are developed in well-2 than in well-3.

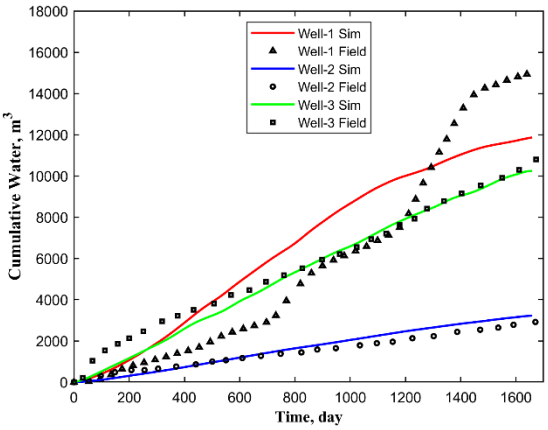

Figure 6.5 Simulation results of cumulative water production for three wells.

Figure 6.6 compares the simulation results of producing GOR to the field data and BHP variations for each well. The simulation producing GOR profiles for each well exhibits a similar and consistent trend with the field data during the mid-CHOPS period. For well-1 and well-2, the field producing GOR data at the end of CHOPS is much higher than the simulation results, implying that these two wells are closer to the gas cap than well-3, and consequently, gas from the gas cap may enter wormholes easily.

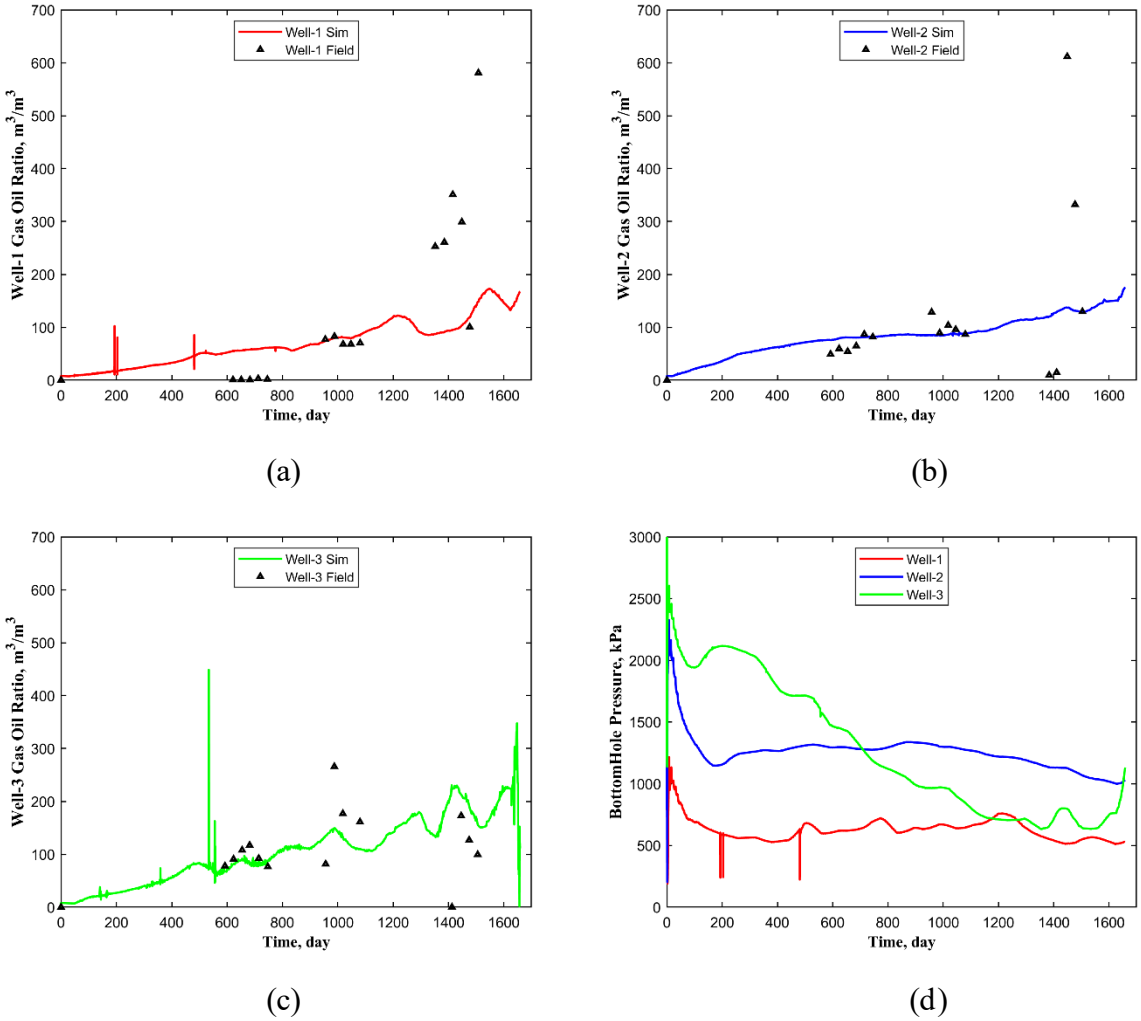

Figure 6.6 Simulation results: (a) well-1 producing gas/oil ratio; (b) well-2 producing gas/oil ratio; (c) well-3 producing gas/oil ratio; and (d) BHP for three wells.

6.4 Wormhole Network Characterization

The wormhole network is fully developed at the end of the CHOPS process along the prescribed fractal pattern. Figure 6.7 exhibits the wormhole permeability distribution at the end of CHOPS to represent the development of the wormhole network. Differentiated footprints of wormholes can be visually observed in the three graphs, and the cumulative oil and sand production is correlated to the coverage of wormholes in a qualitative sense.

As shown in Figure 6.7 (d), the density of the developed wormhole network is plotted against the designated path (i.e., fractal patterns). Almost all matrix cells along the fractal pattern are activated to wormhole cells in well-1, indicating the consistent density variation over distance in the fractal pattern and the wormhole network. The wormhole network in well-3 displays the least developed one, as indicated by the most significant gap between the two density plots of the fractal pattern and the wormhole network over distance.

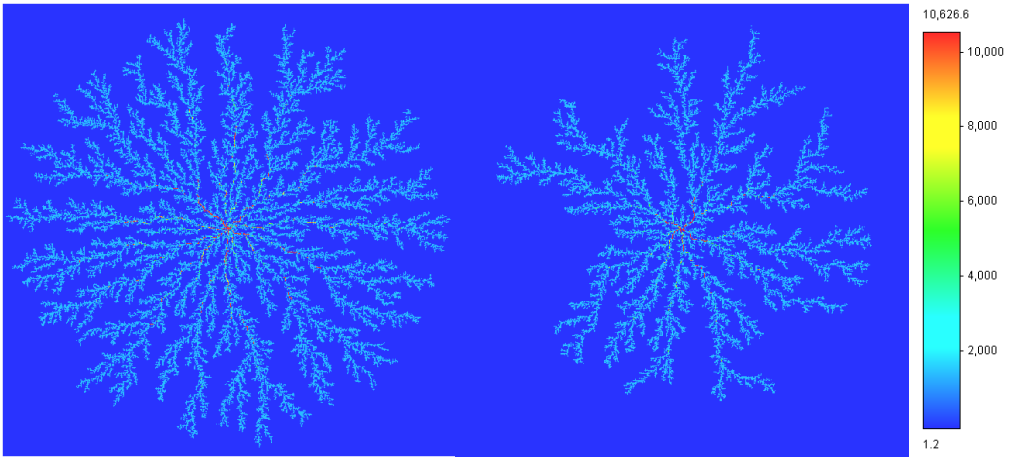

(a) (b)

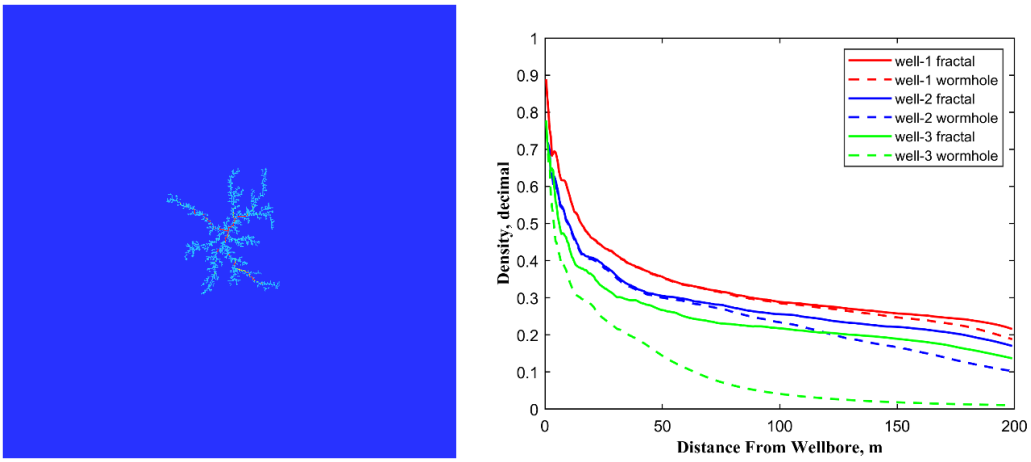

(c) (d)

Figure 6.7 Wormhole networks at the end of CHOPS process for (a) well-1; (b) well-2; (c) well-3 and (d) density contrasts between fractal patterns and wormhole networks.

The density of the wormhole network changing with time is shown in Figure 6.8. The wormhole density of well-3 declines rapidly during the initial 200 days, indicating that the wormhole propagates slower than the other two cases, even though the same advancement rate was selected for all three wells (Table 6.1). Wormhole density for well-3 remains constant after 300 days because the wormhole stops expanding. Eventually, the wormhole network would stop growing for all three wells. Figure 6.9 shows the top view of the development of wormhole coverage for each well. Well-3 exhibits the least visually dense network in the sixth month. By contrast, the wormhole network of well-1 approximately covers the whole domain at the end of CHOPS. Evidently, the network in well-1 is denser than the other two at each selected period.

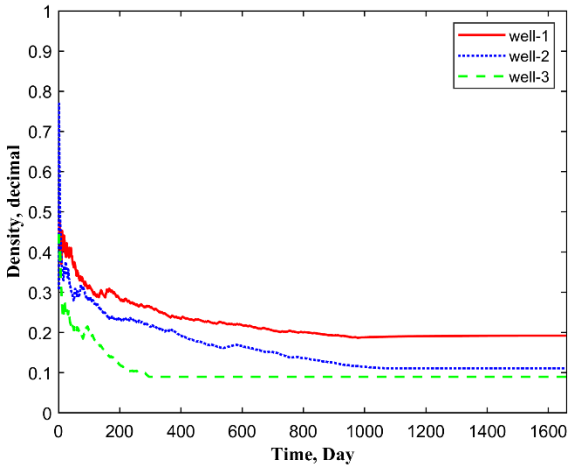

Figure 6.8 The density of the wormhole network varies over time for three wells.

It should be noted that the density of the wormhole network is measured based on the current area that wormholes covered, where the radius is selected as the distance between the farthest wormhole cell and the wellbore. Therefore, the size of the red circles containing the wormhole network in Figure 6.9 differs for three wells at the same selected time. Nonetheless, the density of the wormhole network in well-1 is greater than in the other two wells at the same selected time. While the density in well-3 approaches well-2 at the end of CHOPS (Figure 6.8), even with a significant size difference of red circles (Figure 6.9) between them. The simulation results demonstrate that the greater the wormhole network density, the more branches there are, making the network more complex and resulting in greater sand production.

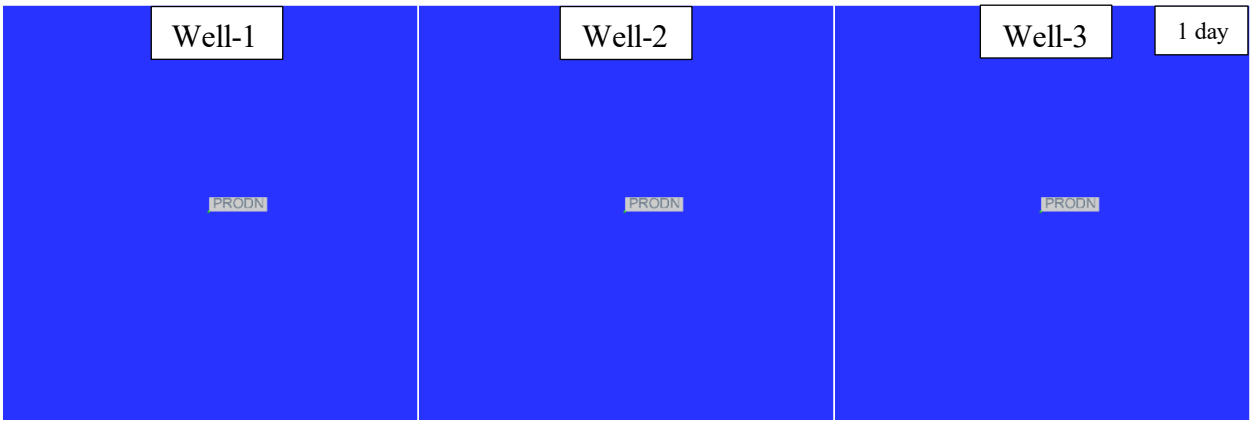

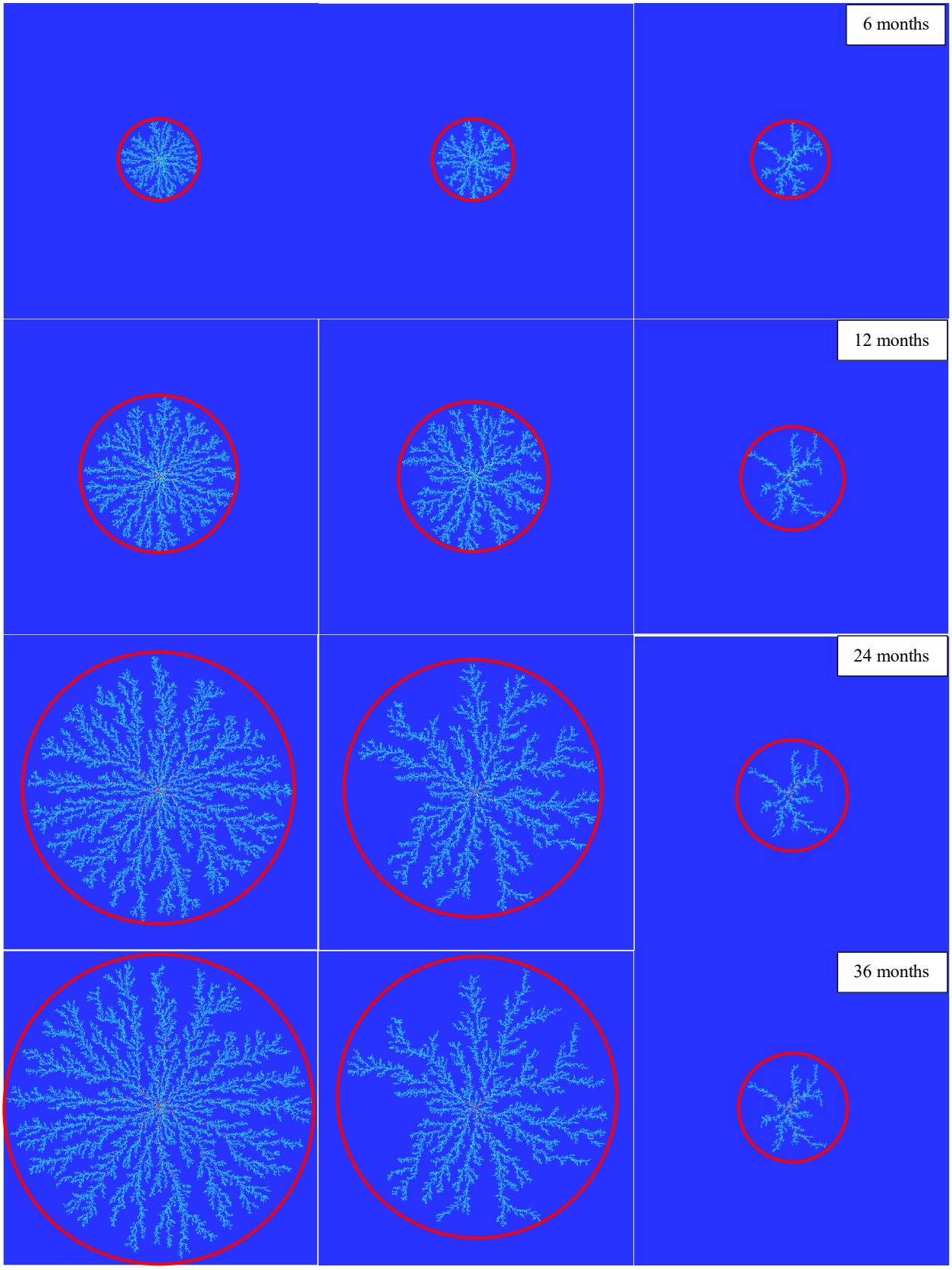

Figure 6.9 Top view of the permeability distribution in the middle (wormhole) layer at different times for three wells.

6.5 Summary

- Aiming to further investigate the robustness of the improved CHOPS model for simulating a variety of production and flow behaviours associated with CHOPS wells, three CHOPS wells with different production profiles were selected to demonstrate how the refined model in this study can be used to simulate production behaviour from other CHOPS wells with different production profiles. These three CHOPS wells came from Dee Valley area near Lloydminster in western Saskatchewan. Further tuning of the parameters in the refined model in this study was required to match the production behaviour from these wells. In particular, a time-dependent division factor was introduced into the sand production model to offer additional flexibility in representing sand transport during different periods of CHOPS production. This factor can be used to tailor the rate of sand transport depending on the conditions in the wormhole network (i.e., the effective porosity and oil flow rate).
- Parameters in the foamy oil model (i.e., the frequency factors controlling the nonequilibrium behaviour) and the critical gas saturation were tuned to match the historical producing GOR data for these three wells. These parameters had to be changed slightly for each well in order to match the field gas production data.
- The simulated cumulative water production was matched to the field water production data by tuning the relevant endpoints in the relative permeability system for each well. A good match to field water production was achieved for two of the wells with this approach, but the match was not as good for one of the wells. As discussed in Section 5.3.3, it is possible that a water zone contributed to the water production from this well; if such a water zone existed, its location is not known.

- To enhance the flexibility of the improved CHOPS model in effectively simulating a variety of production and flow behaviours, a time-varying division factor available in CMG STARS was employed in this study to model a wide range of sand production behaviours throughout the different periods in the life of CHOPS wells. The introduction of this division factor allows v_{crit} to be set so that sand production can be matched well during the initial stage of CHOPS; since the division factor is time-varying, it can be constructed to increase over time so that the simulated rate of sand production is maintained at an adequate level following the peak in sand production. Other parameters in the sand production model such as *exp*, as well as the maximum time step size for the rate of wormhole advancement, were adjusted to match the historical oil and sand production data.
- The fractal pattern generation code in the model by Yu and Leung (2020) was modified so that different fractal patterns could be assigned for different wells to be more compatible with their oil and sand production histories. Typically, denser fractal patterns were more suitable for cases with more oil and sand production during the CHOPS process. The simulated results showed that CHOPS wells with more oil and sand production could generate a more extensive wormhole network.

CHAPTER 7: PURE CO_2 INJECTION IN CSI DURING POST-CHOPS PROCESS

This work is launched based on the model proposed by Yu and Leung (2020) and subsequently modified in Chapter 5, which is used to perform history matches for three CHOPS single wells from Dee Valley in Lloydminster area with different production and flow behaviours (Chapter 6).

The reservoir condition at the end of CHOPS is determined as the initial condition for subsequent CSI simulations for each well. In the model, realistic fractal wormhole patterns are generated by the DLA algorithm to represent the wormhole branching network. In the CHOPS process, the wormhole network grows dynamically by coupling three-phase multi-component flow simulation with a sand arch failure criterion: the wormhole network would expand following the fractal pattern only if the pressure gradient at the tip exceeds a threshold specified in the sand arch failure criterion.

However, the dynamic propagation of the wormhole network would stop as barely sand production and sufficient stability of wormhole structures in the CSI (Oldakowski and Sawatzky, 2018). In non-thermal CSI processes, the behaviour of solvent with heavy oil is the determinant for oil production and solvent recovery. Hence, the nonequilibrium processes, including dissolution and exsolution of solvent and foamy oil behaviour, are key to simulate for a reasonable and representative production forecast. This chapter provides insights into the effect of bubble lifespan in foamy oil flow, and reaction frequency factor (*rrf*) in solvent dissolution and exsolution.

In this research, pure CO_2 was selected as the solvent for the CSI simulation over a mixture of CO_2 with propane or methane, or a mixture of propane and methane. There are several reasons for making this somewhat arbitrary choice. As mentioned in Section 2.3, the solvent in a gaseous form can pressurize the reservoir more effectively than if it is in a liquid form (Chang and Ivory,

2013; Coskuner and Huang, 2020b). As illustrated in Figure 7.1, at the targeted initial reservoir condition, 3,000 kPa and 20 °C (Table 4.2), both CO_2 and a mixture of 86% CO_2 and 14% propane have similar phase behaviour; both remain in the gaseous phase at the target maximum injection pressure. However, the cost of adding propane to injection stream means that a CO_2/propane mixture would need to have significant advantages over CO_2 alone to make a more attractive solvent for CSI.

In fact, CO_2 has some additional advantages over CO_2/propane mixtures, as discussed in Section 2.4. These are summarized below:

- Stays longer in heavy oil as dispersed bubbles;
- Fewer losses to the reservoir;
- Dissolves faster in live oil.

CO_2 has further advantages over methane/propane mixtures, as discussed in Section 2.4. These are summarized below:

- Easier to dissolve into heavy oil;
- Reduces oil viscosity more;
- Creates more nucleation sites as pressure depletes.

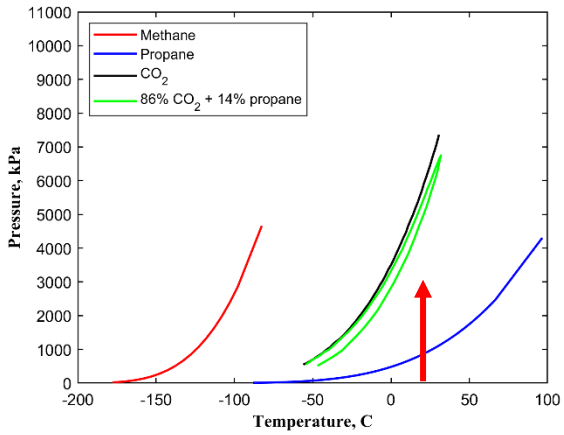

Figure 7.1 Phase envelope for methane, propane and CO_2 (100% each), and mixture of CO_2 and propane (86%/14%). The tip of the red arrow indicates the temperature and maximum pressure in this simulation study. (https://www.fluidmodelinggroup.com/Calc/PVTTests)

Note that a solvent mixture of CO_2 and propane as the basis for CSI could be targeted in a future work using this improved CHOPS model. Such a simulation study could investigate whether adding small fractions of propane to CO_2 could offer advantages in the performance of CSI. For example, a solvent mixture containing both propane and CO_2 could reduce the viscosity of the resulting solvent-heavy oil mixture more than it is reduced using only CO_2 while maintaining foamy oil flow as a result of sufficient amount of CO_2. Several different compositions of a CO_2-propane mixture could be explored to try to find a mixture that offers an optimal performance of the CSI process. However, in the field pilot test reported by Coskuner and Huang (2020b), the addition of 14% propane to CO_2 did not lead to an improvement in CSI performance. It was speculated by Coskuner and Huang (2020b) that the reason could have been the loss of propane during the soaking period.

7.1 Tuning Parameters of the Base Case for Each Well

The base case for each well should contain a reasonable set of parameter selections that could result in a representative forecast of post-CHOPS. Based on the CSI results from piloting tests and field-scale simulation studies (Husky Energy, 2011; Chang and Ivory, 2013; 2015; Coskuner and

Huang, 2020b), some key parameters in the model are tuned to obtain a reasonable forecast for the CSI process.

Since a solvent is injected into the reservoir, the parameter associated with nonequilibrium processes (solvent dissolution and exsolution) is critical to reproduce the foamy oil flow in CSI. Reaction kinetics (i.e., rate of mass transfer) of nonequilibrium processes are measured by the *rrf* and controlled by how significantly the mole fraction of solvent deviates from the equilibrium solvent mole fraction in the oleic phase. As aforementioned in Chapter 3, the equilibrium composition is dependent on pressure and temperature. The *rrf* can be obtained experimentally (Wang et al., 2020; 2022; 2023). However, given the significantly different scale between the laboratory and field, results from laboratory could merely be a guide for the parameter selection in a field simulation. The *rrf* ranges from 6.94×10^{-7} to 6.94×10^{-6} day^{-1} for CO_2 dissolution and exsolution in the experimental tests, whereas in a field scale, after some sensitive analyses, the *rrf* of CO_2 dissolution (r_{CO2s}) is in order of magnitude of 0.0001 day^{-1} or smaller, which is aligned with the value of 0.0005 day^{-1} provided in the study by Chang and Ivory (2013).

Regarding the exsolution process, Chang and Ivory (2013) used an identical value to that of the solvent dissolution. However, it is worth noting that the dead oil viscosity in their study is greater than that in this study (18,755 mPa·s at 23.4 °C versus 5,000 mPa·s at 20 °C). In porous media, the great oil viscosity hinders the growth and coalescence of dispersed bubbles by slowing the diffusion of dissolved gas and dispersed bubbles (Maini et al., 1993; Uddin, 2005; Okazawa, 2009; Busahmin et al., 2017). Compared to the study conducted by Chang and Ivory (2013), bubbles are more likely to nucleate and coalesce in this study due to the lower oil viscosity.

Furthermore, CO_2 exhibits a higher capacity to produce more nucleation sites (Bjorndalen et al., 2012) than methane and propane (a mixture of 60% methane and 40% propane used in the study by Chang and Ivory, 2013). This implies the dissolved CO_2 is more likely to develop dispersed bubbles within the oleic phase under given pressure and temperature conditions. As a result of the aforementioned factors, *rrf*s associated with the exsolution process (including bubble nucleation and coalescence) for CO_2 is expected to be greater than that stated in the study by Chang and Ivory (2013). Parameters selected for the base case of each well are shown in Table 7.1.

Property	Values
r_{CH4s} for CH_4 dissolution (day^{-1})	1.0×10^{-5}
r_{CH4b} for CH_4 nucleation (day^{-1})	0.215
r_{CH4g} for CH_4 coalescence (day^{-1})	0.0215 (0.0108 for Well-1)
r_{CO2s} for CO_2 dissolution (day^{-1})	0.0005
r_{CO2b} for CO_2 nucleation (day^{-1})	0.05
r_{CO2g} for CO_2 coalescence (day^{-1})	0.005
Diffusion coefficient for oleic components (m^2/day)	4.32×10^{-5}
Diffusion coefficient for gaseous components (m^2/day)	0.0144
Mechanical dispersion for both oleic and gaseous phases(m)	0.005

Table 7.1 Parameters for gas/oil mixing and nonequilibrium processes for the base case.

Typically, methane is experimentally demonstrated that it exhibits a higher level of difficulty in dissolving into heavy oil compared to CO_2 under a given pressure and temperature conditions (Tharanivasan et al., 2006; Bjorndalen et al. 2012; Ma et al., 2017; Bryan et al., 2018). Therefore, in this study, a low r_{CH4s} is allocated to methane re-dissolution into heavy oil. Exsolution *rrf*s for methane (r_{CH4b} and r_{CH4g}) are inherited directly from the CHOPS process. Parameter selections for the mixing process are referenced from the study by Chang and Ivory (2013).

7.2 Effect of More Rapid Bubble Coalescence

The reduction of heavy oil viscosity and foamy oil flow by CO_2 injection in the CSI process primarily contribute to the enhancement of heavy oil recovery. In CSI simulations, the bubble lifespan of CO_2 dispersed bubble is affected by r_{CO2g} (*rrf* for coalescence of CO_2 dispersed bubbles) and how far off it deviates from r_{CO2b} (*rrf* for nucleation of CO_2 dispersed bubbles). If $r_{CO2g} \geq r_{CO2b}$, CO_2 dispersed bubbles are more likely to connect, forming a free gas, consequently leading to a shorter bubble lifespan.

In the base case, the *rrf* of coalescence is merely one-tenth of the *rrf* of nucleation for both methane and CO_2. In a new case termed the "more rapid coalescence" case (hereinafter referred to as MRC case), r_{CO2g} is equal to r_{CO2b}, individually for each well. Moreover, r_{CH4g} is also increased by a factor of ten in the MRC case, as shown in Table 7.2. This MRC case is used to assess the impact of reduced bubble lifespan. Other parameters remain constant in two cases.

	r_{CH4b} (day^{-1})	r_{CH4g} (day^{-1})	r_{CO2b} (day^{-1})	r_{CO2g} (day^{-1})
Base case (Table 7.1)	0.215	0.0215 (0.0108 for well-1)	0.05	0.005
MRC case	0.215	0.215 (0.108 for well-1)	0.05	0.05

Table 7.2 Parameter selections for CH_4 and CO_2 exsolution process in the base case and MRC case.

7.2.1 Cumulative Oil Production

The cumulative oil production of the base case and the MRC case at the end of production in each individual cycle is shown in Table 7.3 and Figure 7.2. Notably, increasing both r_{CH4g} and r_{CO2g} by a factor of ten leads to a considerable decrease in oil production for each well following three cycles (Figure 7.2). For instance, the total cumulative oil production is substantially decreased by 40% from 6,623 m^3 to 3,953 m^3 after three cycles in well-1. This change supports the conclusion

that foamy oil flow, in the form of a longer lifespan of dispersed bubbles, is beneficial to oil recovery.

On the other hand, as indicated in Table 7.3, for the MRC case, the cumulative oil production in well-3 decreases as the cycle progresses. However, the cumulative oil production during cycle 2 is increased by ~10% (17% in the MRC case for well-2) than in cycle 1. For cycle 3, the cumulative oil production is generally decreased by ~10% compared to cycle 2 (20% in the MRC case for well-3). More details are discussed later.

	Wells	Cumulative oil production in each cycle (std m^3)			
		Cycle 1	Cycle 2	Cycle 3	In total
Base case	Well-1	2,163	2,345	2,116	6,623
	Well-2	1,742	1,815	1,684	5,241
	Well-3	1,054	1,205	1,125	3,384
MRC case	Well-1	1,316	1,400	1,236	3,953
	Well-2	1,087	1,275	1,154	3,516
	Well-3	506	478	380	1,316

Table 7.3 Cumulative oil production of the two cases in each individual cycle.

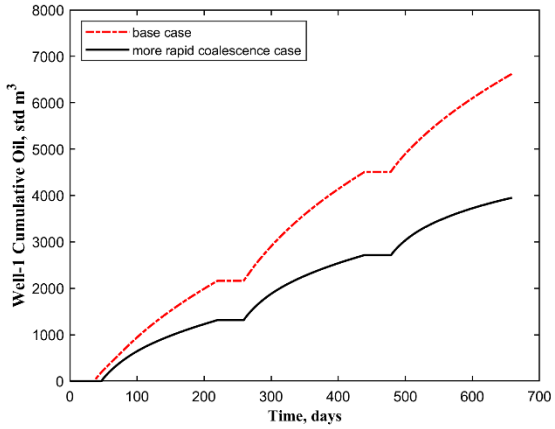

(a)

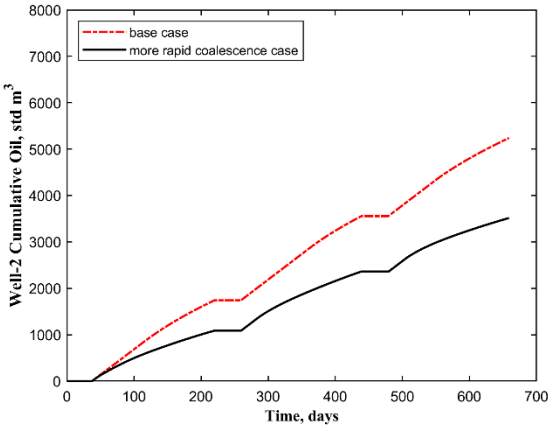

(b)

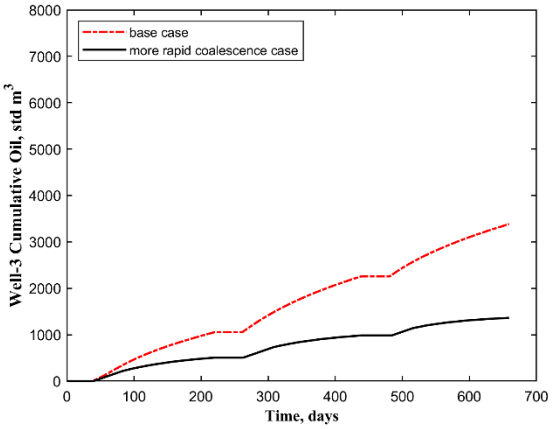

(c)

Figure 7.2 Cumulative oil production of the two cases for (a) well-1; (b) well-2 and (c) well-3.

7.2.2 Cumulative CO_2 Injection and Production

Table 7.4 exhibits the details of cumulative CO_2 injection and production at the end of production in each individual cycle for the two cases. BHP variation over time for all scenarios is shown in Figure 7.3. The well constraint experiences an earlier alteration from injection rate (i.e., primary constraint) to maximum BHP (i.e., secondary constraint) during the injection in the base case than in the MRC case. Specifically, for the base case in well-1, BHP reaches the maximum earlier during the injection in all three cycles than in the MRC case, as illustrated in Figure 7.3 (a). While for the base case in well-2 and well-3, BHP changes consistently in cycle 1 with the MRC case. The earlier alteration of well constraint occurs during the injection in the latter two cycles in the base case compared to the MRC case, as shown in Figure 7.3 (b) and (c). Significantly, for the base case in well-2, BHP during the production in cycles 2 and 3 drops slower than in the MRC case. This indicates that a longer period of time for the well is constrained by the maximum oil rate in the base case.

This earlier alteration of well constraint results in inconsistent injection volumes in the two cases, as indicated in Table 7.4. Cumulative CO_2 injection volume during each individual cycle in

the MRC case exhibits a higher or equal level than in the base case. Consequently, after three cycles of injection and production, a higher total cumulative CO_2 injection volume is recorded in the MRC case compared to the base case for each well. Notably, well-1 exhibits nearly double the injection volume in the MRC case (Table 7.4).

Moreover, cumulative CO_2 production in each individual cycle demonstrates remarkedly increases as the lifespan of dispersed bubbles is reduced in the MRC case compared to the base case. Even, cumulative CO_2 production differs by an order of magnitude in some scenarios (e.g., cycle 1 of well-1). Huge differences in total cumulative CO_2 production can be observed between the two cases. As the cycles progress in each well, cumulative CO_2 production gradually increases, with the exception of well-1 in the MRC case, which is discussed later.

	Wells	Cumulative CO_2 injection in each cycle ($\times 10^5$ std m^3)				Cumulative CO_2 production in each cycle ($\times 10^5$ std m^3)			
		Cycle 1	Cycle 2	Cycle 3	In total	Cycle 1	Cycle 2	Cycle 3	In total
Base case	Well-1	7.00	2.14	1.89	11.04	0.53	0.69	0.83	2.05
	Well-2	2.67	1.56	1.36	5.58	0.45	0.43	0.59	1.47
	Well-3	1.50	1.13	0.95	3.59	0.37	0.35	0.46	1.17
MRC case	Well-1	8.66	6.41	6.39	21.46	6.66	4.54	6.29	17.49
	Well-2	2.70	2.79	2.72	8.21	1.01	1.33	2.21	4.54
	Well-3	1.50	1.55	1.55	4.60	0.92	1.36	1.61	3.89

Table 7.4 Cumulative CO_2 injection and production of the two cases in each individual cycle.

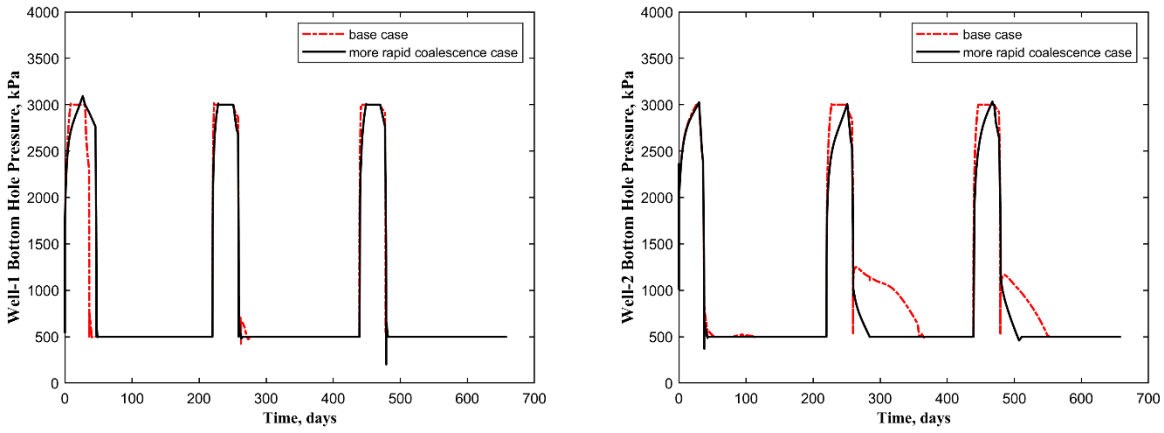

(a) (b)

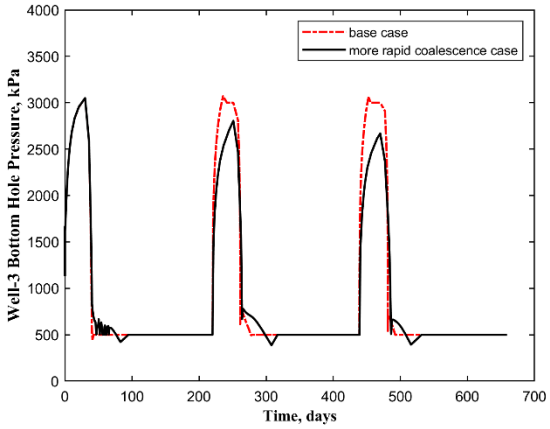

(c)

Figure 7.3 BHP of the two cases: (a) BHPwell-1; (b) well-2 and (c) BHPwell-3BHP.

7.2.3 Cumulative CO_2 Retention, Recovery and Net CO_2/Oil Ratio

Table 7.5 lists the cumulative CO_2 retained in the reservoir, the corresponding CO_2 recovery factor and net CO_2/oil ratio of the two cases at the end of production in each cycle. Compared to the MRC case, exceptionally high cumulative CO_2 retained in the reservoir and small CO_2 recovery factor can be observed in the base case. These demonstrate that more rapid bubble coalescence can significantly decrease CO_2 retention in the reservoir and increase its recovery. As the cycles progress, generally, the increase in cumulative CO_2 retention diminishes. Even in cycle 3 of well-3 in the MRC case, CO_2 retention is lower than in cycle 2. By contrast, in the base case, the increase

in cumulative CO_2 recovery rises as the cycles progress, while in the MRC case, the increments differ in different well. These may imply an increase in the proportion of newly injected CO_2 that is produced during the latter cycles. Besides, as shown in Table 7.5, the well with a better development of wormhole network exhibits a lower cumulative CO_2 recovery. The MRC case for well-2 stands as an exception which exhibits a significantly lower one than in the two others.

Net CO_2/oil ratio refers to the ratio of the net amount of CO_2 injected into the reservoir (i.e. difference between CO_2 injection volume and production volume, or CO_2 retained in the reservoir) to the amount of oil produced during a specific time period. It reflects the utilization of CO_2 injection volume in displacing oil from underground. A lower net CO_2/oil ratio is more desirable, rendering a cost saving. The gradually decreased net CO_2/oil ratio as the cycle progresses in the two cases (Table 7.5) implies an improved CO_2 utilization. For the MRC case in well-1 and well-3, the smaller net CO_2/oil ratio than in the base case indicates that more rapid bubble coalescence facilitates the utilization of CO_2. However, the situation in well-2 stands the opposite, the net CO_2/oil ratio in the MRC case is greater than in the base case.

	Wells	Cumulative CO_2 retained in the reservoir after each cycle ($\times 10^5$ std m^3)			CO_2 recovery after each cycle (%)			Net CO_2/oil ratio after each cycle (std m^3/m^3)		
		Cycle 1	Cycle 2	Cycle 3	Cycle 1	Cycle 2	Cycle 3	Cycle 1	Cycle 2	Cycle 3
Base case	Well-1	6.47	7.93	8.99	7.5	13.3	18.5	299.4	175.8	135.7
	Well-2	2.21	3.35	4.12	17.0	20.8	26.3	127.1	94.1	78.5
	Well-3	1.13	1.92	2.41	24.4	27.2	32.7	107.6	84.8	71.3
MRC case	Well-1	2.00	3.87	3.97	76.9	74.3	81.5	151.7	142.4	100.4
	Well-2	1.69	3.16	3.67	37.3	42.5	55.3	155.8	133.6	104.2
	Well-3	0.58	0.77	0.71	61.5	74.8	84.5	113.9	78.2	52.1

Table 7.5 Cumulative CO_2 retained in the reservoir, CO_2 recovery factor and net CO_2/oil ratio of the two cases after each cycle.

7.2.4 Distribution of CO_2 Dispersed Bubbles

As illustrated in Figure 7.4, a certain quantity of CO_2 dispersed bubbles is observed at the end injection period in cycle 1 for the two cases, which is not supposed to be generated during pressurization. Evidently in well-1, as indicated in Figure 7.4 (a) and (d), the mole fraction of CO_2 dispersed bubbles near the wellbore in the base case is greater than in the MRC case, while the other two wells separately exhibit a similar distribution for both cases.

During the injection, the solvent injection causes rapid pressurization and advection, leading to a great fraction of CO_2 is dissolved into the heavy oil rapidly. This, in turn, gives rise to local pressure reductions, particularly within the wormhole cells near the wellbore. If the instantaneous mole fraction of dissolved CO_2 exceeds the equilibrium mole fraction in the oleic phase under the current pressure and temperature conditions, irreversible gas exsolution occurs locally. The first product of the kinetic pseudo reactions, CO_2 dispersed bubbles, increases the oleic phase volume, thereby reducing the pore space available for free gas. The existing free gas in that block is compressed, causing a local pressure to rise again. Sufficient CO_2 dispersed bubbles formed and retained longer will eventually cause BHP to ascend rapidly and remain at the maximum, consequently reducing the injection rate. If CO_2 dispersed bubbles coalescing to a free gas occurs more rapidly (i.e., the MRC case), the quantity of CO_2 dispersed bubbles is reduced, releasing the supersaturation state. The alteration of well constraints will advent later.

Since the substantially higher injection rate in well-1 (Section 4.3) can cause greater pressurization and significant advection around the wellbore than well-2 and well-3, the rate of CO_2 dissolution is relatively higher, increasing the likelihood of occurrence of local CO_2 exsolution. Consequently, in the base case, the earlier alteration of well constraints is more likely to happen during cycle 1 in well-1 than in the two others, as indicated in Figure 7.3 (a). The similar

distribution of CO_2 dispersed bubbles demonstrates that the injection rate is insufficient to support more local CO_2 exsolution and thereby the alteration of well constraints during cycle 1 in the base case. However, BHP reaching the maximum earlier in the injection of cycles 2 and 3 in the base case for well-2 and well-3, as shown in Figure 7.3 (b) and (c), is primarily attributed to the presence of CO_2 dispersed bubbles retained from previous cycles, as indicated in Figure 7.5.

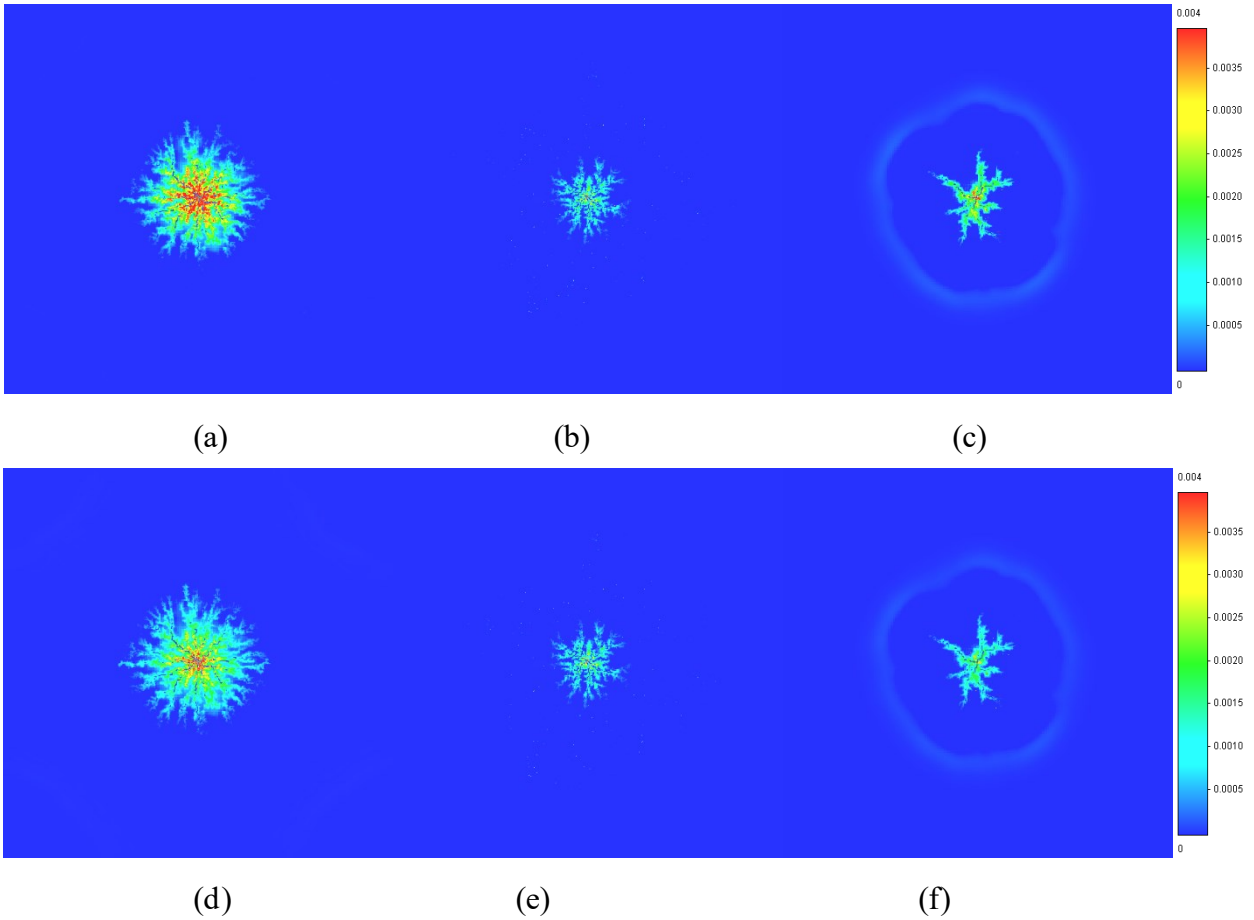

Figure 7.4 Distribution of CO_2 dispersed bubbles (mole fraction in oleic phase) at the end of injection in cycle 1 of (a) the base case for well-1; (b) the base case for well-2; (c) the base case for well-3; (d) the MRC case for well-1; (e) the MRC case for well-2 and (f) the MRC case for well-3.

At the end of each cycle, CO_2 retained in the reservoir is in the form of free gas, dissolved gas and dispersed bubbles. Due to the nonzero critical gas saturation (as indicated in Table 6.4), a portion of CO_2 free gas is retained in the gaseous phase at the end of each cycle. Figure 7.5 and Figure 7.6 display the distribution of CO_2 dispersed bubbles (mole fraction in the oleic phase) at

the end of production in each cycle for the base case and the MRC case. Visibly, a great discrepancy of the distribution can be observed between the two cases for each well. Due to the more rapid bubble coalescence in the MRC case, much less CO_2 is retained in the form of dispersed bubbles at the end of each cycle compared to the base case, as listed in Table 7.5. Besides, the mole fraction of CO_2 dispersed bubbles increases as the cycles progress, significantly near the wellbore in the base case (Figure 7.5).

In the base case, due to the great CO_2 injection volume (Table 7.4) in cycle 1 and the longer bubble lifespan, numerous dispersed bubbles formed during this cycle coalescing to a free gas are delayed. Thus, a significant portion of dispersed bubbles at the end of cycle 1, as illustrated in Figure 7.5 (a), (d) and (g), persists into cycle 2 to enhance oil production. Meanwhile, due to the presence of vast dispersed bubbles, the CO2 injection volume is significantly reduced over cycles, significantly in cycle 2 compared to cycle 1. Nonetheless, the oil production exhibits an increase in cycle 2 from cycle 1, as seen in Table 7.3, demonstrating the significance of the foamy oil behaviour. The widespread of CO_2, in turn, increases its retention in the reservoir (Table 7.5). However, the reduction in injection cannot support newly injected CO_2 transporting farther from the wellbore to mix with heavy oil, thereby facilitating the generation of CO_2 dispersed bubbles. As a result, CO_2 dispersed bubbles are mainly distributed near the wellbore in the latter two cycles, with an area visually smaller than in cycle 1.

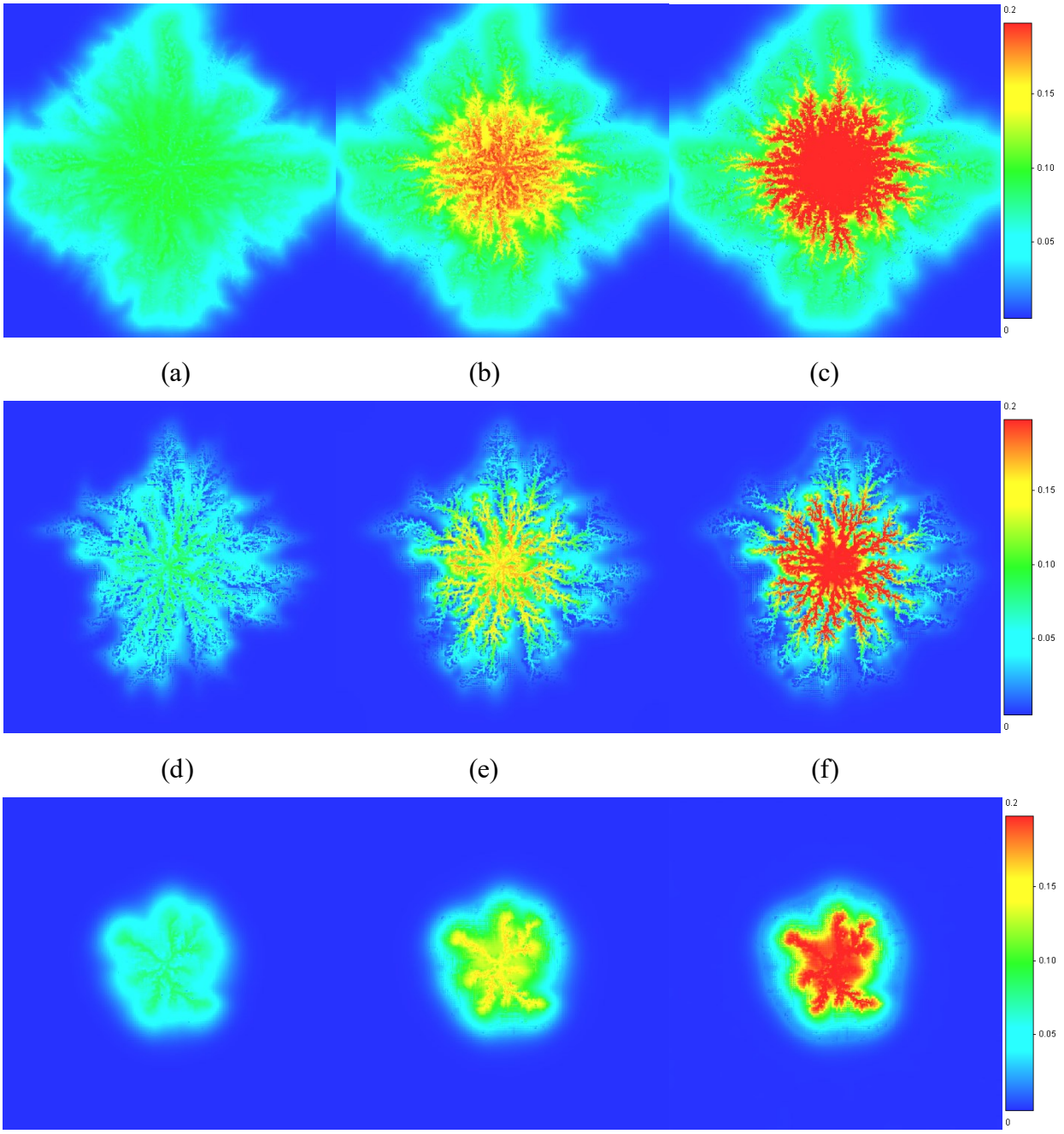

Figure 7.5 Distribution of CO_2 dispersed bubbles (mole fraction in oleic phase) for the base case at the end of production in (a) cycle 1 in well-1; (b) cycle 2 in well-1; (c) cycle 3 in well-1; (d) cycle 1 in well-2; (e) cycle 2 in well-2; (f) cycle 3 in well-2; (g) cycle 1 in well-3; (h) cycle 2 in well-3 and (i) cycle 3 in well-3.

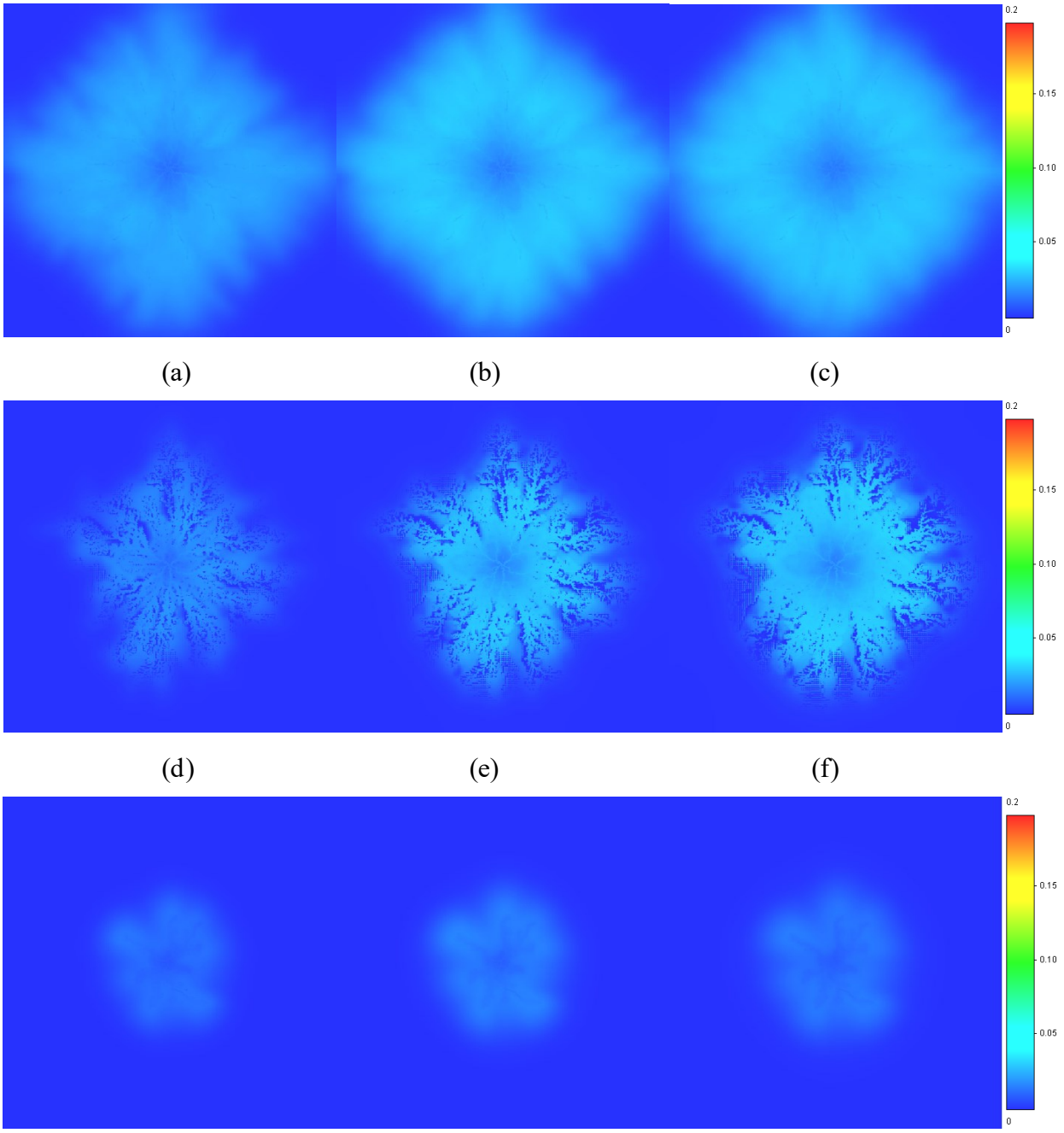

Figure 7.6 Distribution of CO_2 dispersed bubbles (mole fraction in oleic phase) for the MRC case at the end of production in (a) cycle 1 in well-1; (b) cycle 2 in well-1; (c) cycle 3 in well-1; (d) cycle 1 in well-2; (e) cycle 2 in well-2; (f) cycle 3 in well-2; (g) cycle 1 in well-3; (h) cycle 2 in well-3 and (i) cycle 3 in well-3.

7.2.5 Distribution of Dissolved CO_2

The different area contained CO_2 dispersed bubbles (Figure 7.5 and Figure 7.6) in each well is the consequence of the distinct development of wormhole networks for injected CO_2 transportation

and mixing with heavy oil (i.e., CO_2 footprint). With a well-developed wormhole network and considering the injection rate (Section 4.3), the CO_2 footprint is most extensive at well-1, followed by well-2, and is smallest at well-3. The magnitude of CO_2 footprint directly influences the dissolved CO_2 in heavy oil and the generation of CO_2 dispersed bubbles for foamy oil flow, ultimately impacting oil production. The widespread of CO_2, in turn, increases its retention in the reservoir (Table 7.5). The CO_2 footprint can be represented by the distribution of dissolved CO_2 or CO_2 dispersed bubbles (mole fraction in oleic phase). Note that using the latter to represent the CO_2 footprint can only be captured accurately at the end of the production period.

At the end of soaking, the distribution of dissolved CO_2 (mole fraction in the oleic phase) reflects the development of the CO_2 footprint right before the production. As illustrated in Figure 7.7 for the base case, the development of CO_2 footprint by newly injected CO_2 decreases as the cycles progress. The increased oil production in the base case compared to the MRC case (Table 7.3) demonstrates the dominant contribution made by the foamy oil behaviour in the form of a longer bubble lifespan, rather than the CO_2 footprint.

Figure 7.8 displays the distribution of dissolved CO_2 (mole fraction in oleic phase) at the end of soaking. The CO_2 footprint is visibly increased in cycle 2 compared to cycle 1, as shown in Figure 7.8 (b), (e) and (h). This increase suggests that the injection volume during cycle 1 inadequately sufficiently facilitates the spread of CO_2 in the reservoir. It is fairly believed that CO_2 injected during cycle 2 continues to expand its footprint. However, the similar injection volume during cycle 3 results in minor changes in CO_2 footprint compared to cycle 2. This demonstrates that cycle 2 shows a significantly faster increase in CO_2 retention within the reservoir compared to cycle 3, as indicated in Table 7.5. Additionally, the visible increase in CO_2 footprint as the

cycles progress for well-2, as shown in Figure 7.8 (d) – (f), contributes to the extremely low CO_2 recovery (Table 7.5) compared to well-1 and well-3 in the MRC case.

Besides, in the MRC case, oil production increases to a different extent in cycle 2 than in cycle 1 (Table 7.3) due to the expansion of the CO_2 footprint, except in well-3. This is attributed to the low injection rate in well-3 (Section 4.3), leading to insufficiently pressurizing the reservoir and creating foamy oil flow, even though the CO_2 footprint slightly extends as the cycles progress, as shown in Figure 7.8 (g) – (i).

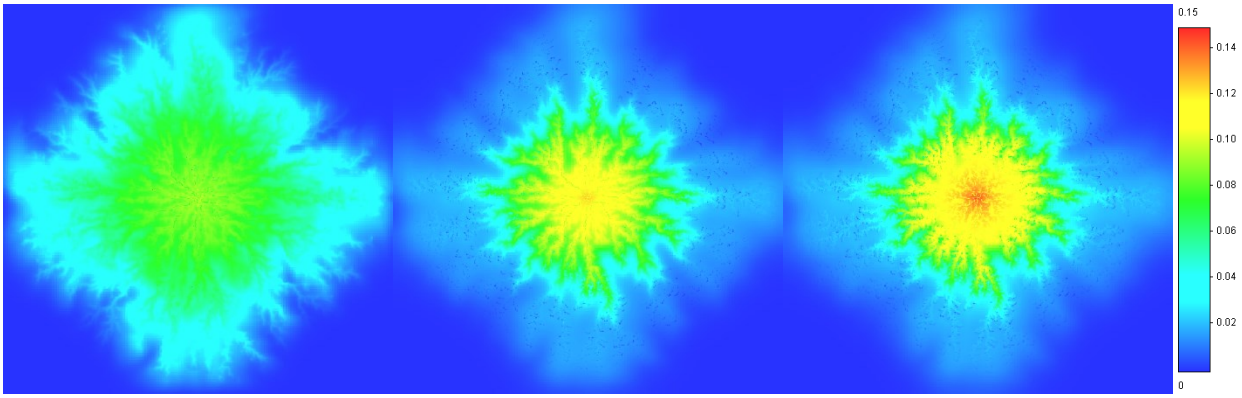

(a) (b) (c)

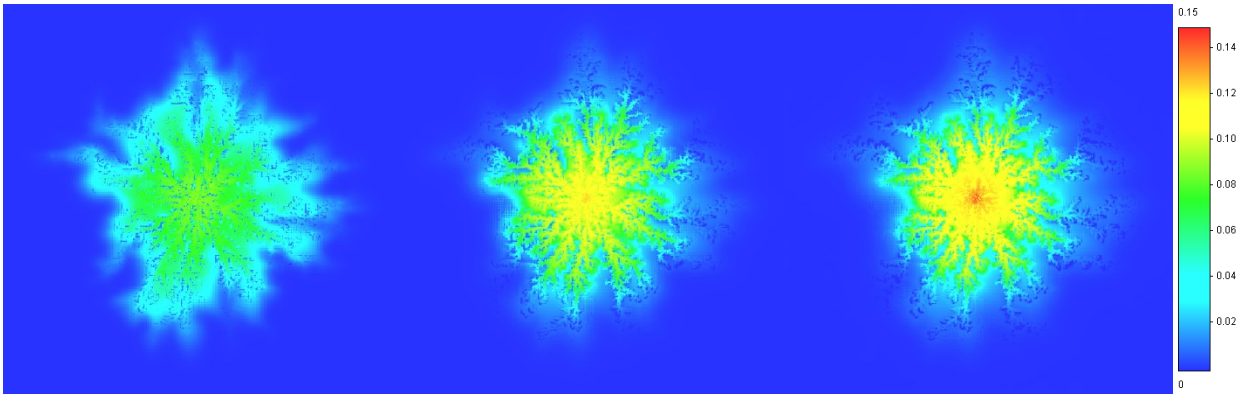

(d) (e) (f)

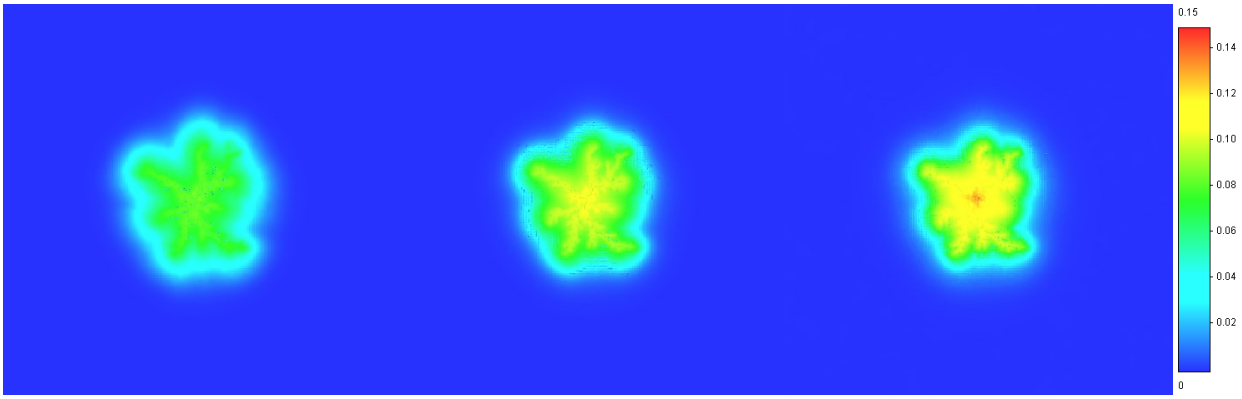

(g) (h) (i)

Figure 7.7 Distribution of dissolved CO_2 (mole fraction in oleic phase) in the base case at the end of soaking in (a) cycle 1 in well-1; (b) cycle 2 in well-1; (c) cycle 3 in well-1; (d) cycle 1 in well-2; (e) cycle 2 in well-2; (f) cycle 3 in well-2; (g) cycle 1 in well-3; (h) cycle 2 in well-3 and (i) cycle 3 in well-3.

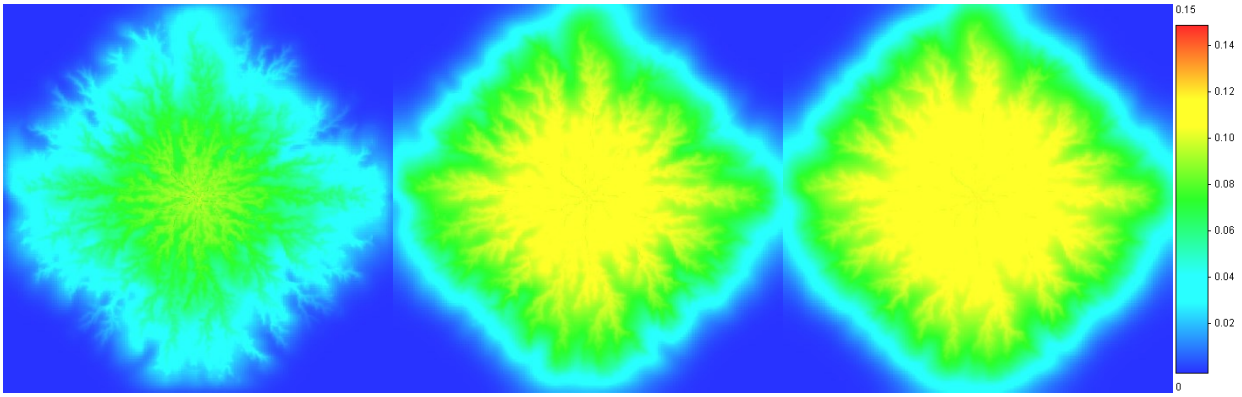

(a) (b) (c)

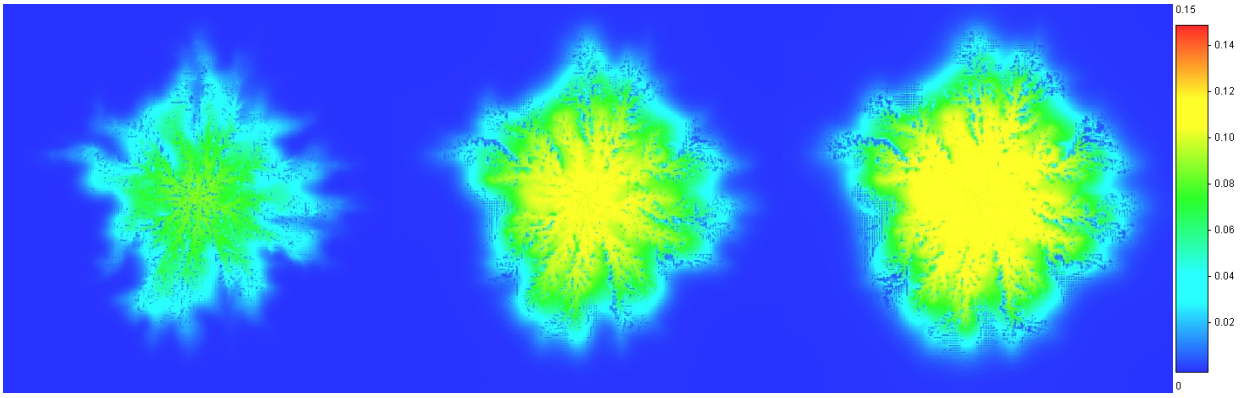

(d) (e) (f)

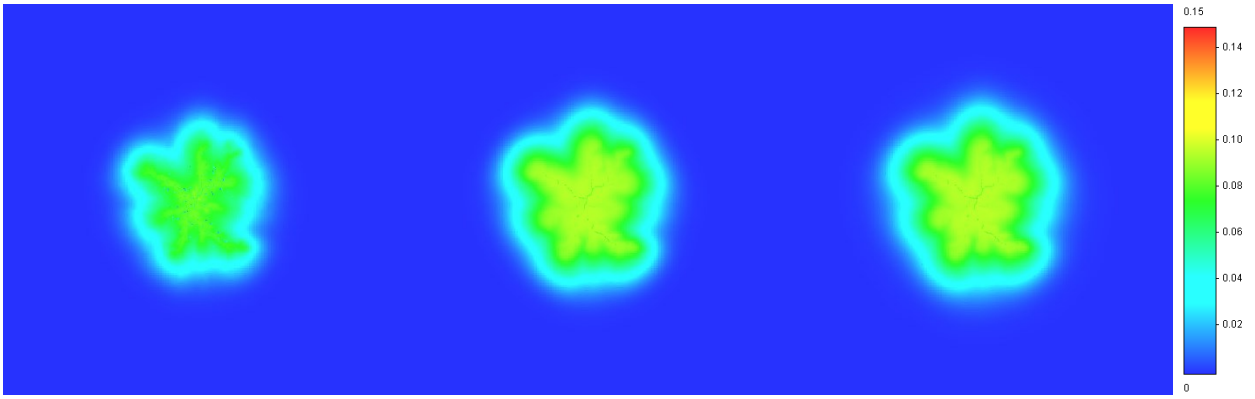

(g) (h) (i)

Figure 7.8 Distribution of dissolved CO_2 (mole fraction in oleic phase) in the MRC case at the end of soaking in (a) cycle 1 in well-1; (b) cycle 2 in well-1; (c) cycle 3 in well-1; (d) cycle 1 in well-2; (e) cycle 2 in well-2; (f) cycle 3 in well-2; (g) cycle 1 in well-3; (h) cycle 2 in well-3 and (i) cycle 3 in well-3.

Figure 7.9 and Figure 7.10 demonstrate the distribution of dissolved CO_2 at the end of production in each cycle for the base case and the MRC case. Generally, compared to the base case, the MRC case exhibits a higher mole fraction of dissolved CO_2 in the reservoir at the end of production in each cycle for each well. The visible disparity between the two cases suggests that a relatively greater fraction of dissolved CO_2 is converted to CO_2 dispersed bubbles in the base case. The plausible reason is that, in the base case, the longer presence of CO_2 dispersed bubbles increases the oleic phase volume, as mentioned earlier, maintaining the reservoir pressure at a high level. This will force CO_2 free gas to dissolve into the heavy oil more rapidly, increasing the amount of dissolved CO_2. During the production, the increasing pressure facilitates the bulk motion of the oleic phase, and diffusion and dispersion enable dissolved CO_2 to gather around the wellbore. This significantly raises x_{CO2sn} in the downstream blocks, which overwhelms the increased x'_{CO2sn} caused by the elevated reservoir pressure. According to Eq. 4, more CO_2 dispersed bubbles are generated. This also explains that, in the base case, the mole fraction of dissolved CO_2 and CO_2 dispersed bubbles are higher around the wellbore than in the MRC case, as indicated in Figure 7.5, Figure 7.6, Figure 7.9 and Figure 7.10.

The presence of dissolved CO_2 in the oleic phase can reduce the rate of CO_2 dissolution, as per Eq. 3-25. As shown in Figure 7.9 and Figure 7.10, x_{CO2sn} at the end of each cycle experiences an increase as the cycles progress, except for cycle 3 in the MRC case where shows tiny changes from cycle 2. This indicates the portion of CO_2 remaining in the form of free gas after its injection is increased as the cycles progress. This significantly diminishes the foamy oil flow. Due to CO_2 footprint expanding during cycle 2 in the MRC case and a great quantity of CO_2 dispersed bubbles inherited from cycle 1 in the base case, oil production is increased in cycle 2 than in cycle 1. However, when the two cases lose these advantages during cycle 3, the decreased rate of CO_2 dissolution dominates the reduction in oil production (Table 7.3).

In the MRC case for well-1, due to the phenomenon mentioned above, a greater fraction of CO_2 injected in cycle 2 is retained in the gaseous phase than in cycle 1. This leads to a rapid increase in reservoir pressure (Figure 7.3 (a)) and consequently a decrease in injection volume in cycle 2. Even though x_{CO2sn} increases at the end of cycle 2, the injection volume in cycle 3 remains at a similar level (Table 7.4) due to the expanded CO_2 footprint, as shown in Figure 7.7 (b).

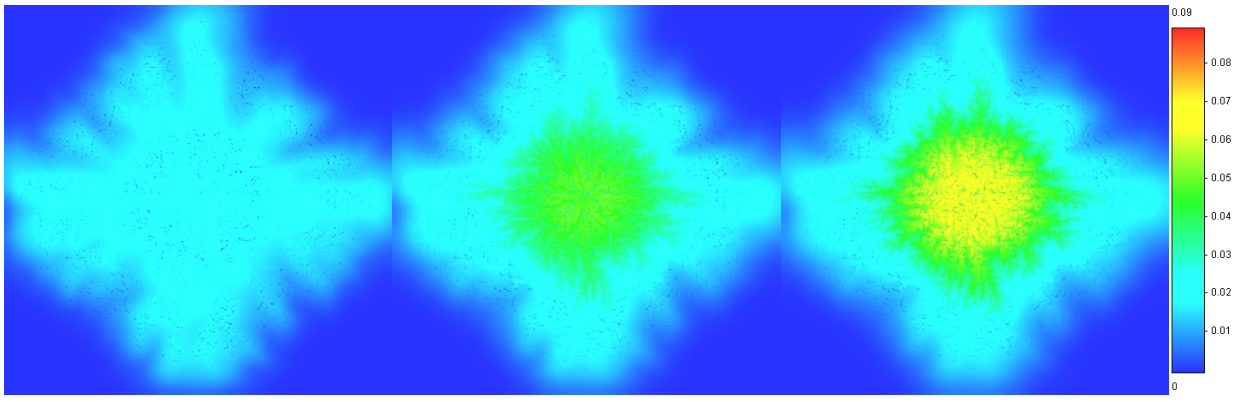

(a) (b) (c)

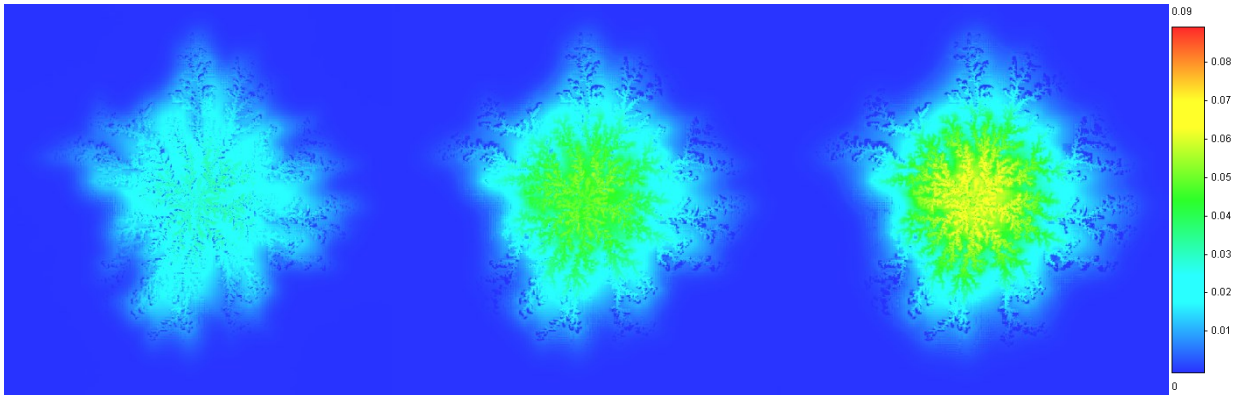

(d) (e) (f)

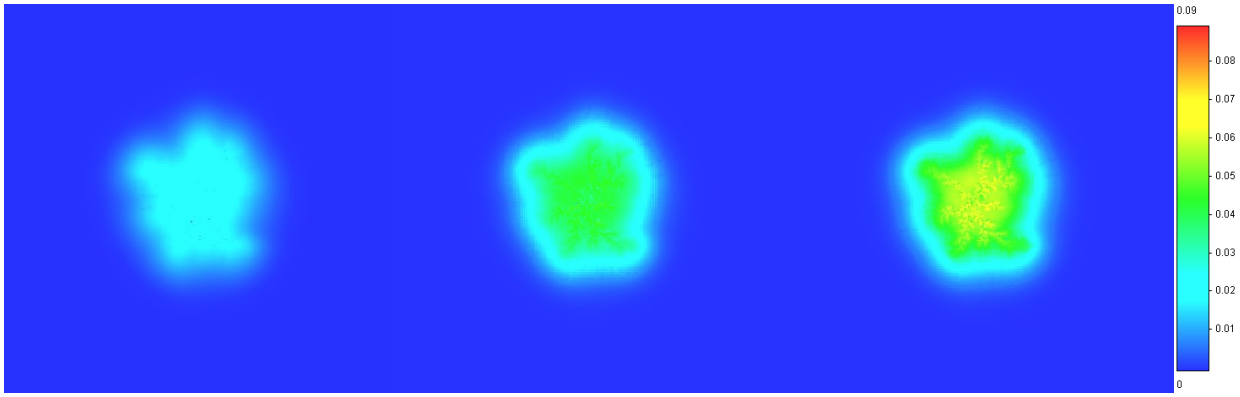

(g) (h) (i)

Figure 7.9 Distribution of dissolved CO_2 (mole fraction in oleic phase) in the base case at the end of production in (a) cycle 1 for well-1; (b) cycle 2 for well-1; (c) cycle 3 for well-1; (d) cycle 1 for well-2; (e) cycle 2 for well-2; (f) cycle 3 for well-2; (g) cycle 1 for well-3; (h) cycle 2 for well-3 and (i) cycle 3 for well-3.

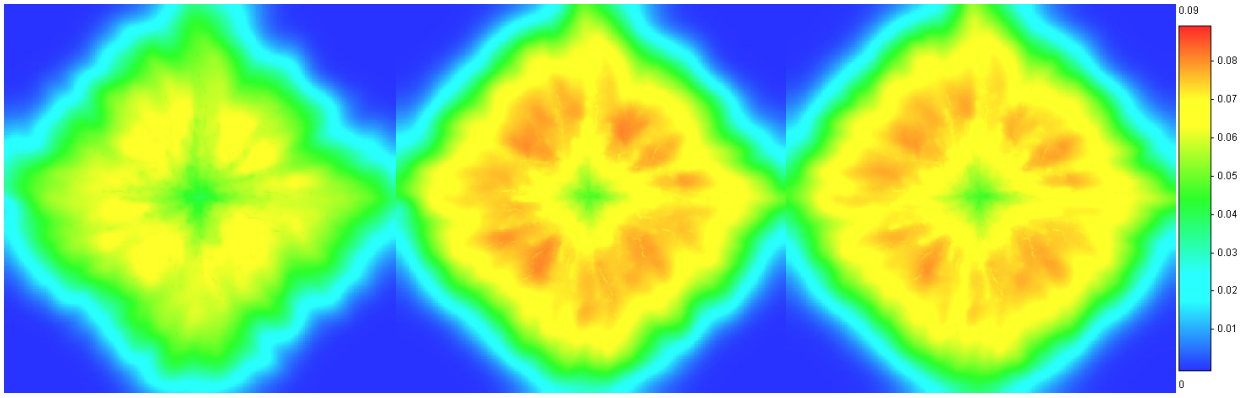

(a) (b) (c)

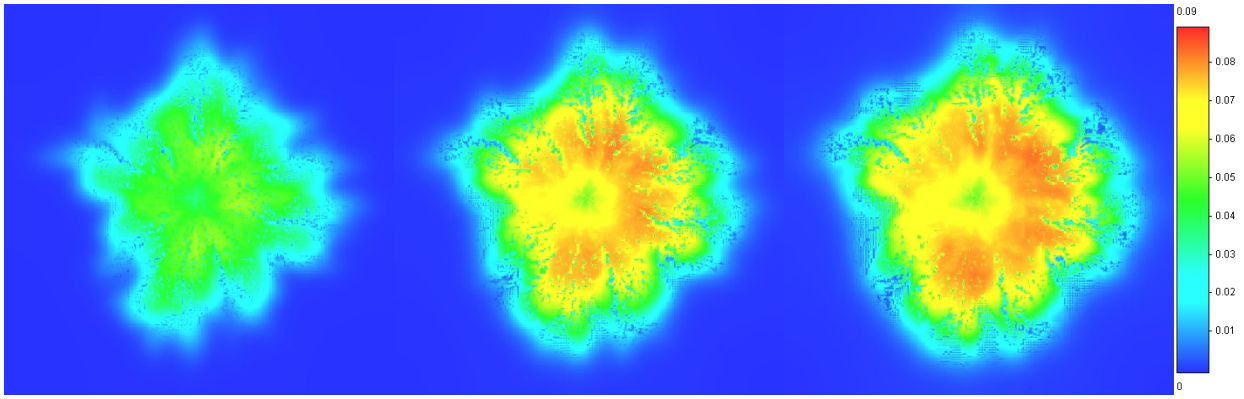

(d) (e) (f)

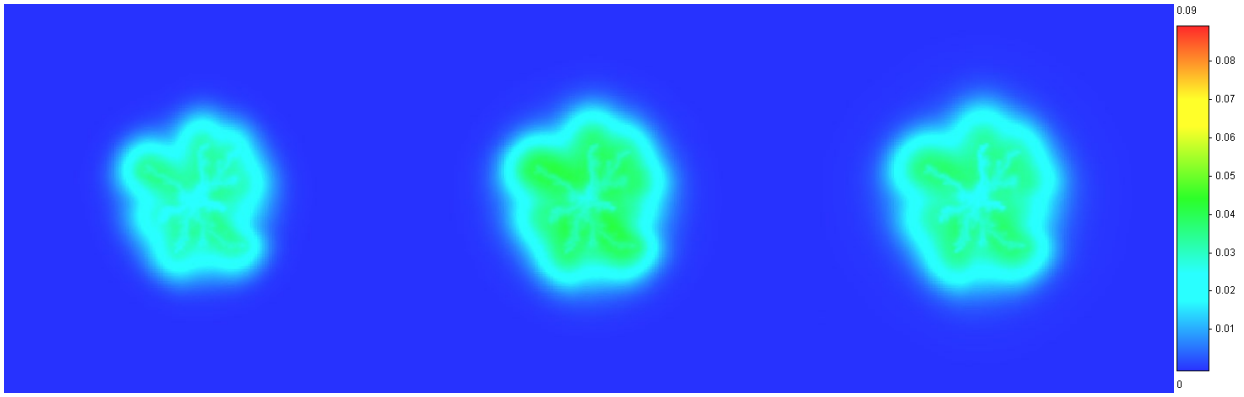

(g) (h) (i)

Figure 7.10 Distribution of dissolved CO_2 (mole fraction in oleic phase) in the MRC case at the end of production in (a) cycle 1 for well-1; (b) cycle 2 for well-1; (c) cycle 3 for well-1; (d) cycle 1 for well-2; (e) cycle 2 for well-2; (f) cycle 3 for well-2; (g) cycle 1 for well-3; (h) cycle 2 for well-3 and (i) cycle 3 for well-3.

7.3 Effect of Reaction Frequency Factor

The reaction frequency factor plays a critical role in nonequilibrium processes. Its magnitude determines the efficiency and effectiveness of the solvent to mix with heavy oil and develop foamy oil flow. To examine the impacts of *rrf* in different nonequilibrium processes, the first cycle of the CSI for each well with different *rrf* is carried out. The testing cases (cases 1 to 4) are listed in Table 7.6.

Run	r_{CO2s} (day^{-1})	r_{CO2b} (day^{-1})	r_{CO2g} (day^{-1})
Base case	0.0005	0.05	0.005
Case 1	0.05	0.05	0.005
Case 2	0.5	0.05	0.005
Case 3	0.0005	0.0005	0.00005
Case 4	0.0005	0.5	0.05
MRC case	0.0005	0.05	0.05

Table 7.6 Impacts of *rrf*s in different nonequilibrium processes.

In contrast to the base case, only *rrf*(s) in one single process is altered in each case, leaving the rest constant. Note that when testing the exsolution process, r_{CO2b} and r_{CO2g} varies concurrently. Cases 1 and 2 are run to investigate the impacts of r_{CO2s}. Cases 3 and 4 are used for the effects of *rrf*s in CO_2 exsolution (r_{CO2b} and r_{CO2g}). Table 7.7 summarizes oil production and CO_2 recovery at the end of cycle 1, while Figure 7.11 depicts the oil production for all cases. As observed in the table, the oil production in all cases at the end of production in cycle 1 is lower than in the base case for each well.

Run	Cumulative oil (std m^3)			CO_2 recovery (%)		
	Well-1	Well-2	Well-3	Well-1	Well-2	Well-3
Base case	2,162	1,742	1,054	7.5	17.0	24.4
Case 1	1,821	1,169	842	26.2	33.6	43.1
Case 2	1,481	914	686	25.6	37.1	47.9
Case 3	838	674	320	15.2	25.0	28.6
Case 4	1,301	1,187	585	26.4	30.8	60.5
MRC case	1,316	1,087	506	76.9	37.3	61.5

Table 7.7 Production results of three wells at the end of production in cycle 1.

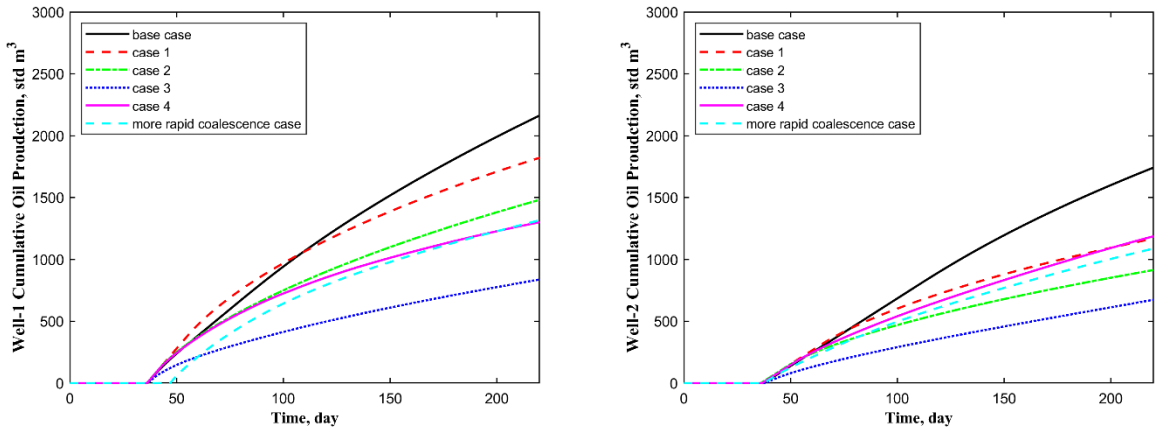

(a) (b)

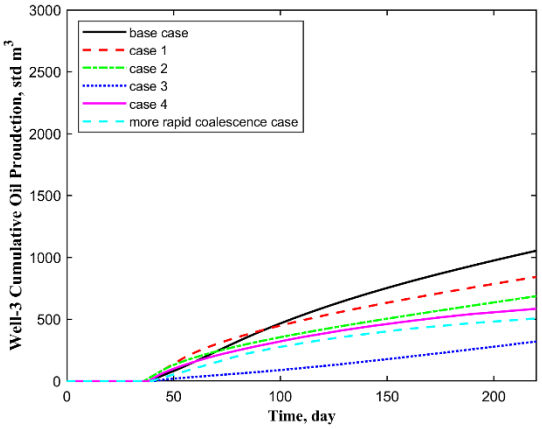

(c)

Figure 7.11 Cumulative oil production for different cases in (a) well-1; (b) well-2; and (c) well-3 at the end of production in cycle 1.

7.3.1 Effect of Faster CO_2 Dissolution

Increasing r_{CO2s} remarkedly raises the amount of CO_2 dissolved into the heavy oil. This results in a relatively substantial formation of CO_2 dispersed bubbles during the injection (as shown in Figure 7.4 and Figure 7.12, note that the two figures are on different scales) compared to the base case. The consequence is that BHP is elevated explosively before the well is put on production in the two cases, as illustrated in Figure 7.13 (a), (c), and (e), even with the well constraint of the maximum BHP of 3,000 kPa in place. The CO_2 injection volume decreases significantly, as illustrated in Figure 7.13 (b), (d) and (f) for cases 1 and 2.

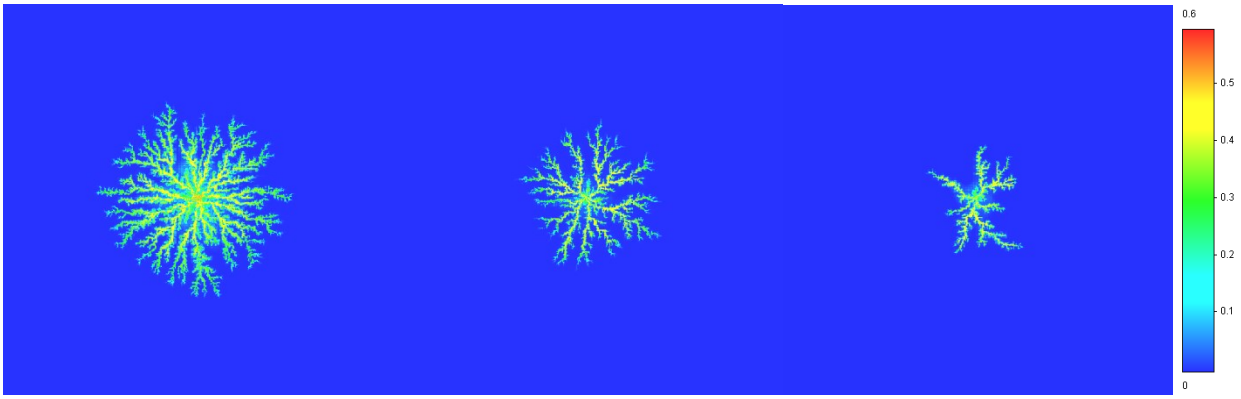

(a) (b) (c)

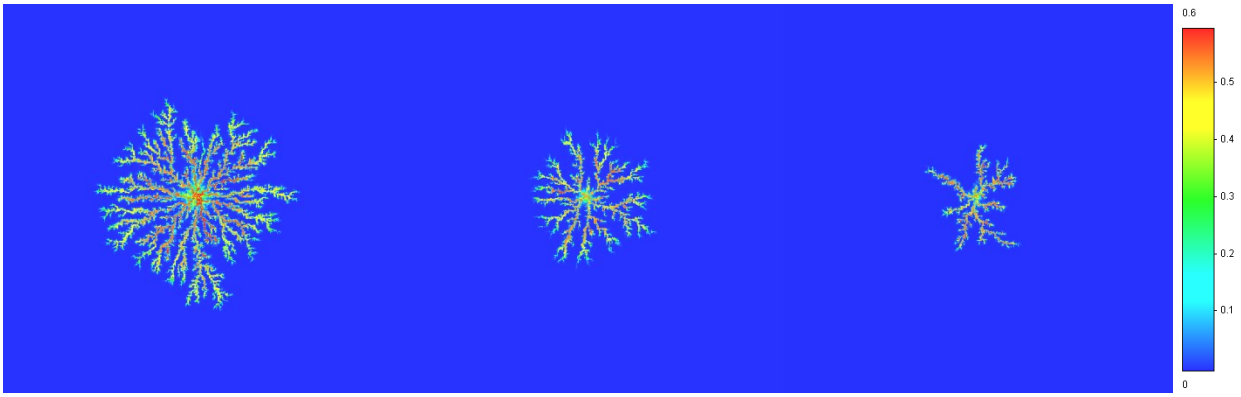

(d) (e) (f)

Figure 7.12 Distribution of CO_2 dispersed bubbles (mole fraction in oleic phase) at the end of injection in cycle 1 of (a) case 1 for well-1; (b) case 1 for well-2; (c) case 1 for well-3; (d) case 2 for well-1; (e) case 2 for well-2 and (f) case 2 for well-3.

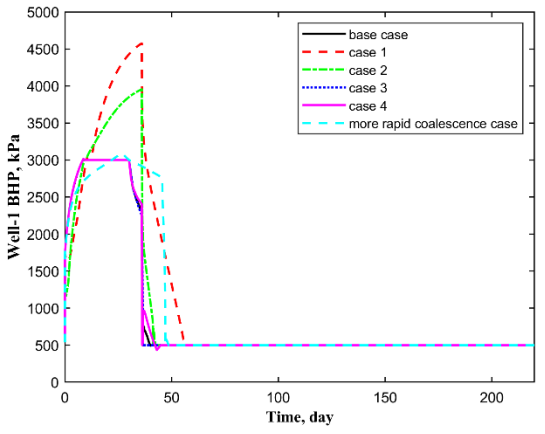

(a)

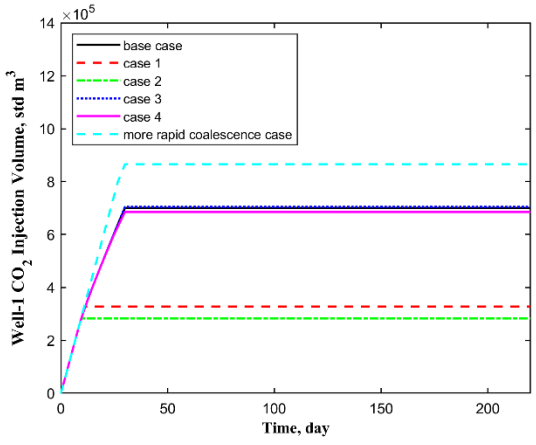

(b)

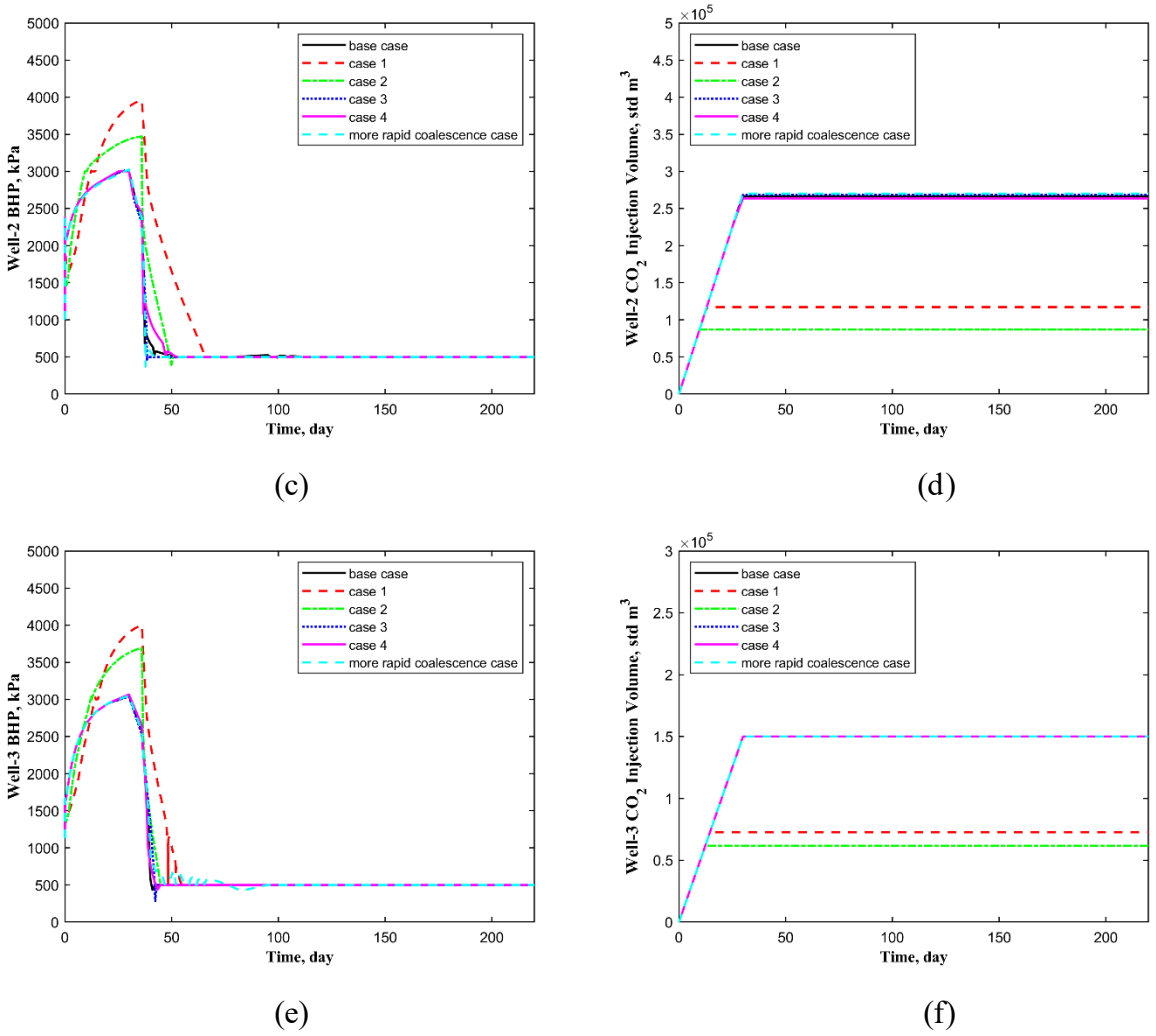

Figure 7.13 Simulating results of all cases at the end of cycle 1: (a) BHP for well-1; (b) Cumulative CO_2 injection for well-1; (c) BHP for well-2; (d) Cumulative CO_2 injection for well-2; (e) BHP for well-3 and (f) Cumulative CO_2 injection for well-3.

At the end of soaking in cycle 1, a significant difference can be observed in the CO_2 footprint between the base case with cases 1 and 2, as illustrated in Figure 7.14 and Figure 7.8 (a), (d) and (g). It demonstrates that increasing r_{CO2s} into heavy oil substantially diminishes the CO_2 transportation along the wormhole network into regions distant from the wellbore. The vast majority of CO_2 is exclusively dissolved into the heavy oil that is distributed within wormhole cells in cases 1 and 2, leaving the heavy oil outside of wormholes untouched by CO_2. Even though the mole fraction of dissolved CO_2 is high near the wellbore at the end of the soaking, the amount

of oil that can be potentially displaced is limited. Ultimately, oil production in cases 1 and 2 is decreased compared to the base case (Table 7.7). There appears to be a larger CO_2 footprint near the wellbore in case 1 than in case 2, indicating that the increase in r_{CO2s} is less likely for CO_2 penetrating the matrix.

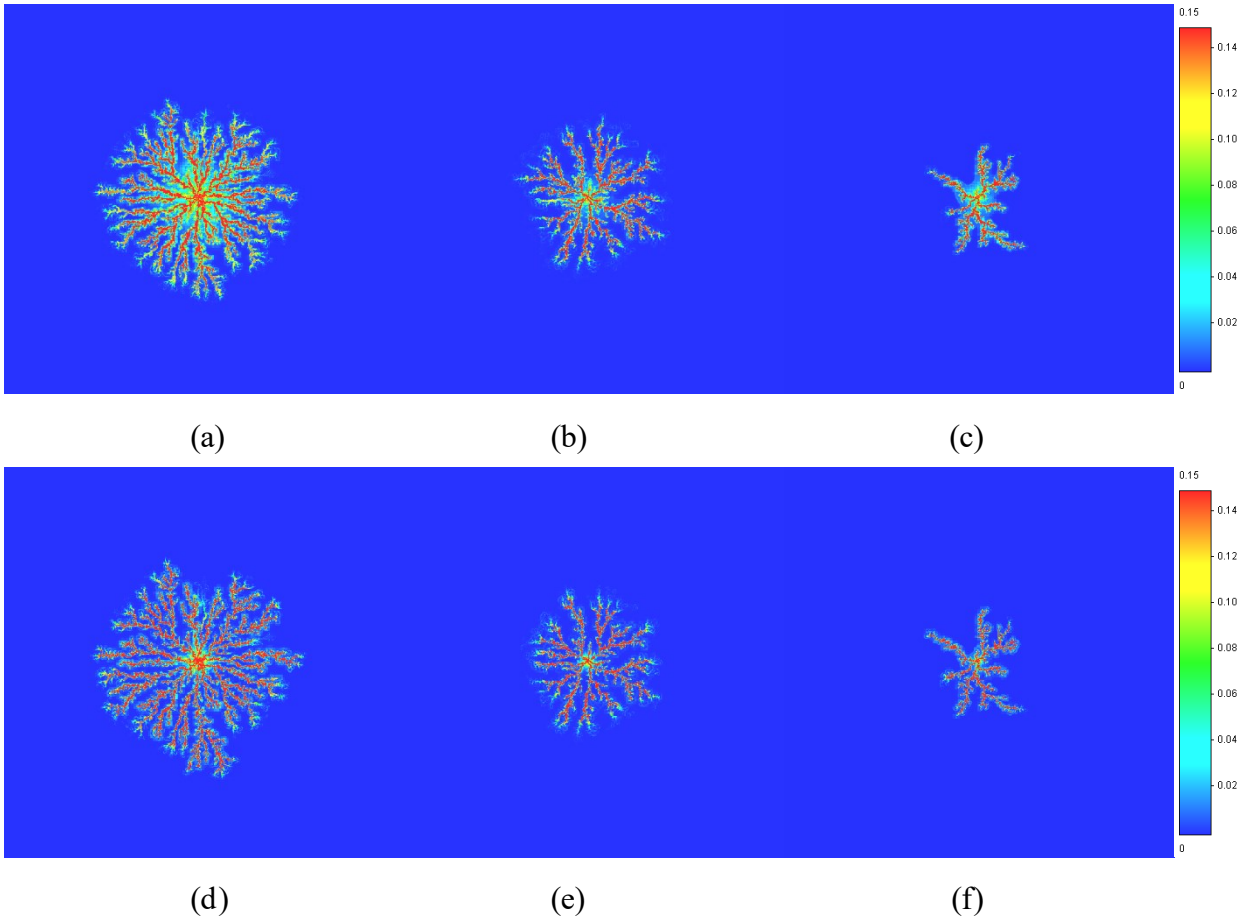

Figure 7.14 Distribution of dissolved CO_2 (mole fraction in oleic phase) at the end of soaking in cycle 1 of (a) case 1 for well-1; (b) case 1 for well-2; (c) case 1 for well-3; (d) case 2 for well-1; (e) case 2 for well-2 and (f) case 2 for well-3.

Figure 7.15 indicates that CO_2 is essentially recovered in the form of bubbles (*CO2b*) and dissolved gas (*CO2s*) in cases 1 and 2. This causes the dependency of CO_2 recovery on oil production and the amount of CO_2 dissolved in heavy oil. The extremely low production observed in CO_2 free gas (*CO2g*) implies that most of the injected CO_2 is dissolved into the heavy oil. Moreover, the production of CO_2 free gas is two orders of magnitude lower than that of methane

free gas (*CH4g*), underscoring that the composition of CO_2 in the gaseous phase stands for an exceptionally low level. Therefore, the CO_2 retained within the reservoir is in the form of dissolved gas, bubble and a minor portion of free gas.

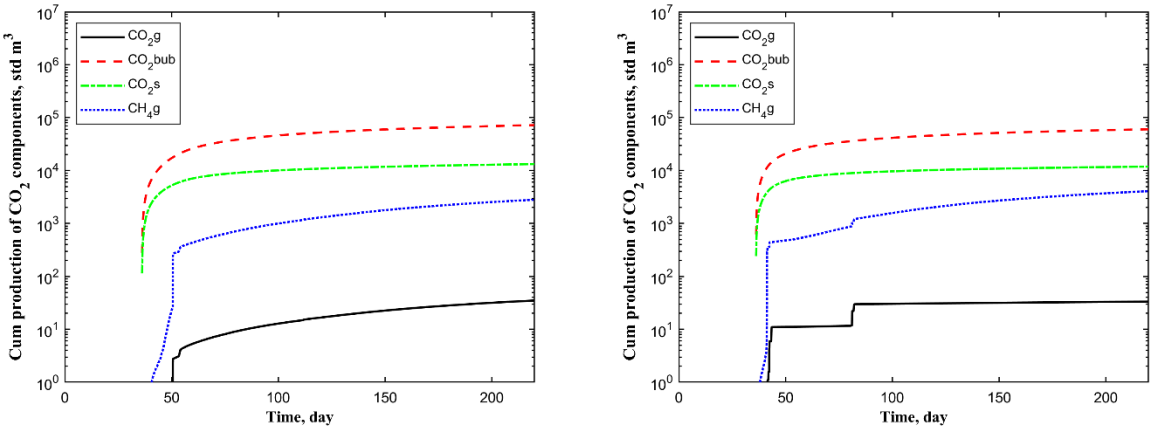

Figure 7.15 Production of different CO_2 components in (a) case 1 and (b) case 2 for well-1.

7.3.2 Effect of Slower/Faster CO_2 Exsolution

Decreasing both r_{CO2b} and r_{CO2g} by an order of two in case 3 remarkedly reduces the generation of CO_2 dispersed bubbles. This decreased foaminess results in the poorest oil production in case 3, as indicated in Table 7.7. Given the injection rate and r_{CO2s} consistent with the base case, case 3 exhibits that a greater portion of CO_2 is retained in the form of dissolved gas at the end of production than in the base case, as illustrated in Figure 7.16 (d) – (f) and Figure 7.9 (a), (d) and (g). While maintaining CO_2 in a dissolved state can keep the heavy oil less viscous, the substantially less foaminess heightens the challenge of effectively driving the oil to the wellbore. So, the comparison between the base case and case 3 suggests that the principle behind CSI to enhance heavy oil recovery extends beyond the mere reduction in heavy oil viscosity; the role of foamy oil behaviour is more pivotal. This is aligned with the conclusion by Chen et al. (2020).

As illustrated in Figure 7.16, compared to the end of soaking, x_{CO2sn} is visibly increased at the end of production; i.e., CO_2 free gas continues to dissolve into heavy oil during the depressurization process. This is attributed to the nature of the nonequilibrium process – CO_2 dissolution. At the end of soaking, $x_{CO2sn} << x'_{CH4sn}$ due to the small r_{CO2s}. When the well is put on production, the slower pressure drop away from the wellbore allows the CO_2 dissolution to persist. During the production, due to less dissolved CO_2 being converted to CO_2 dispersed bubbles, as per Eq. 3-23 and Eq. 3-25 where x_{CO2sn} stands at a high level, CO_2 free gas dissolved into the heavy oil is reduced compared to the base case. Therefore, a higher CO_2 recovery is observed in case 3 in comparison to the base case for each well (Table 7.7).

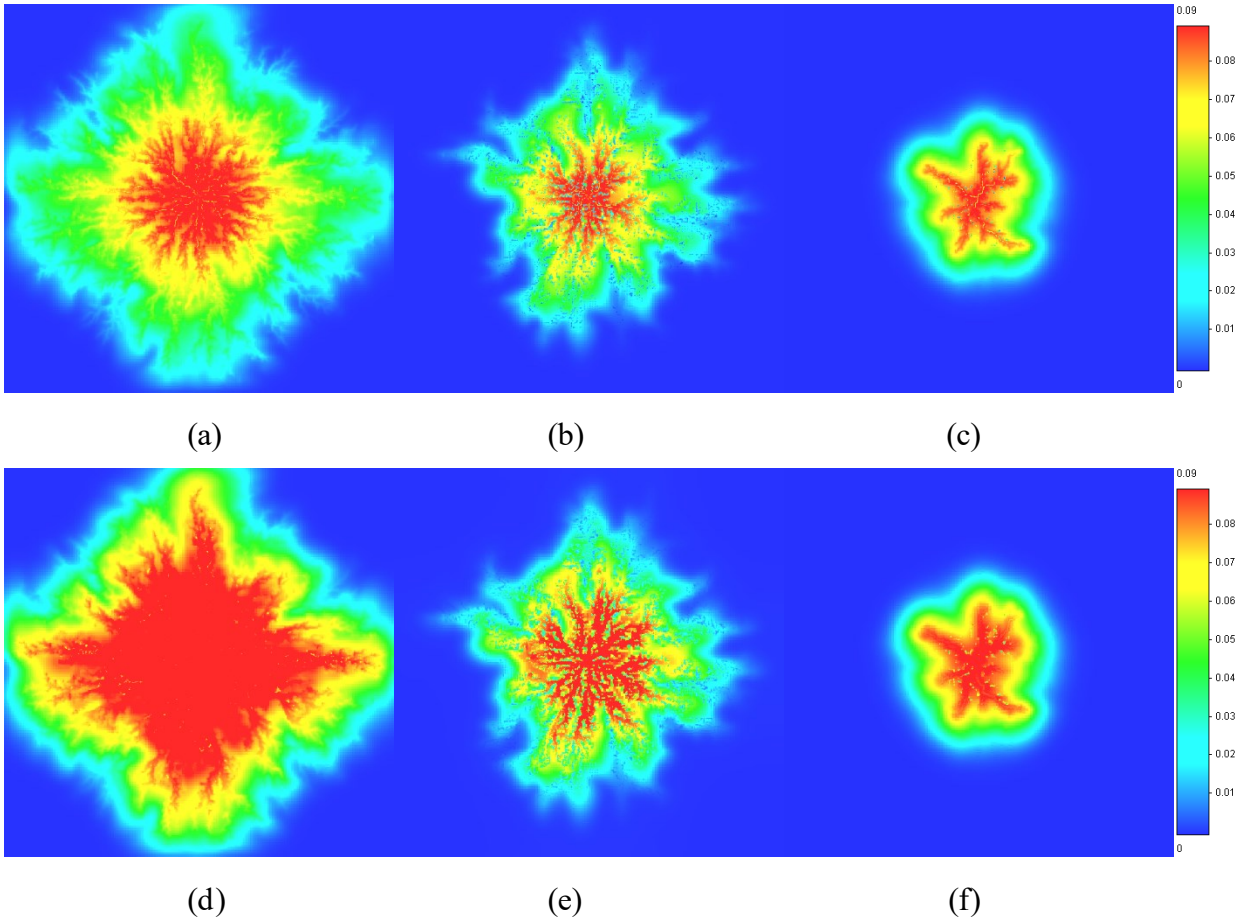

Figure 7.16 Distribution of dissolved CO_2 (mole fraction in oleic phase) in cycle 1 of case 3 at the end of (a) soaking for well-1; (b) soaking for well-2; (c) soaking for well-3; (d) production for well-1; (e) production for well-2 and (f) production for well-3.

An increase in CO_2 recovery and reduction in oil production can be observed in case 4 compared to the base case (Table 7.7). This is because the increase in both r_{CO2b} and r_{CO2g} raises the rate of formation of CO_2 free gas, relatively weakening the foamy oil behaviour. It may suggest that r_{CO2g} holds the critical influence over oil production and CO_2 recovery when a sufficient amount of CO_2 dispersed bubbles is present in the heavy oil. In addition, compared to the MRC case with the same r_{CO2g}, the oil production in case 4 demonstrates a similar level. However, CO_2 recovery in case 4 is a lower than in the MRC case due to the longer bubble lifespan. Besides, as the base case performs, CO_2 recovery in case 4 is lower in wells with better-developed wormhole networks.

7.4 Summary

- Post-CHOPS CSI simulations were performed for the three CHOPS wells simulated in Chapter 6. The initial conditions for the CSI simulations were determined by the simulated reservoir conditions at the end of CHOPS in each of these three wells. The solvent selected for the CSI simulations was 100% CO_2. In the CSI simulations, the wormhole network was assumed to be stable; i.e., no sand production occurred during the CSI process.
- Nonequilibrium processes play a critical role in the dissolution of CO_2 into the live heavy oil, and in the exsolution of CO_2 from the live heavy oil (i.e., via both bubble nucleation and coalescence). The reaction frequency factors (*rrf*s) control the nonequilibrium processes of solvent dissolution and exsolution. This determines the effectiveness of the solvent in mixing with the heavy oil during the injection period and developing foamy oil flow during the production period. The values of the frequency factor for CO_2 dissolution *rrf* (r_{CO2s}) and the values of the dispersion parameters for gas/oil mixing were used from the study by Chang and Ivory (2013). The exsolution *rrf* (for bubble nucleation) for CO_2

was higher in this study than the one in the study conducted by Chang and Ivory (2013). This decision was based on the viscosity of the dead oil in this study compared to the viscosity of the dead oil in the study by Chang and Ivory (2013); the oil viscosity was lower in this study, implying that bubble nucleation would occur more rapidly. Note that the nonequilibrium exsolution model used by Chang and Ivory (2013) did not include a reaction representing bubble coalescence.

- In the base case, bubble coalescence during exsolution was slower, leading to a longer lifespan of dispersed bubbles. When bubble coalescence occurred more rapidly, oil production from CSI decreased significantly. This difference in oil production performance indicates that foamy oil flow, in the form of a longer lifespan of dispersed bubbles, is beneficial to oil recovery.
- When the rate of CO_2 dissolution is faster, the penetration of CO_2 into the matrix beyond the wormhole network is reduced. Most of the injected CO_2 dissolves into the heavy oil that is in the wormhole network. This results in a decrease in oil production, compared to the case when the rate of CO_2 dissolution is slower.
- If the rate of bubble nucleation and coalescence is increased from the base case, oil production decreases. Similarly, if the rate of bubble nucleation and coalescence is decreased from the base case, oil production decreases. In both cases, the lifespan of dispersed bubbles is most likely somewhat shorter than it is in the base case. This provides additional support for the interpretation of the simulation results presented above that foamy oil flow (in the form of dispersed bubbles) is beneficial to oil production.

CHAPTER 8: CONCLUDING REMARKS

8.1 Conclusions

This thesis extends the model developed in a previous study by Yu and Leung (2020). The model proposed by Yu and Leung (2020) integrates the primary physical mechanisms of the CHOPS process: sand production and foamy oil flow. A set of 2D fractal patterns is generated by the DLA algorithm to represent the branching wormhole network in the reservoir. Each fractal pattern used in a simulation is discretized with a locally-refined mesh. It is updated dynamically by coupling a three-phase multi-component flow simulation with a sand arch failure criterion: the wormhole network would expand following the fractal pattern only if the pressure gradient at the tip exceeded a threshold specified in the sand arch failure criterion.

However, in the study by Yu and Leung (2020), the gas exsolution model did not capture the characteristics of foamy oil behaviour adequately. Their model did not simulate an increasing producing GOR, a typical characteristic of CHOPS wells. Also, their model did not capture all of the trends or characteristics associated with the oil and sand production profiles in the CHOPS well presented in their study. These discrepancies indicate the need for further examination and tuning of parameters affecting the wormhole network advancement rate and sand transport through the network. To simulate the performance of potential post-CHOPS processes, it is important to generate a representation of the conditions at the end of CHOPS that are as accurate as possible, since they are the initial conditions for post-CHOPS.

A few modifications and novel aspects are introduced in this thesis: (1) The foamy oil model used by Yu and Leung (2020) was refined. Two kinetic reactions were used to simulate the nucleation and coalescence processes, to allow more flexibility in capturing the variability in

foamy oil behaviour. (2) The wormhole network growth rate was controlled by adjusting the maximum time step size during different periods of CHOPS production (a smaller maximum timestep size can be used to simulate a more rapid growth). The sand production model used by Yu and Leung (2020) was also refined slightly to better control the rate of sand production during the initial period of CHOPS up to the peak of sand production and to better maintain persistent sand production after that. The results of the modifications to the model indicate that the modifications enhance the model flexibility and facilitate more control over matching production behaviour, particularly the rate of sand production and producing GOR. (3) Sensitivity to the reservoir grid size was tested. A smaller grid (250 m by 250 m) was found to be adequate to represent the behaviour of the CHOPS well that was simulated by Yu and Leung (2020). (4) The effect of multiple layers containing a wormhole network on production performance was investigated.

To match against the field performance more effectively, the historical oil and sand production rates were used for operating constraints in the history matching process. One option that was explored was to assign a constant rate (i.e., the reported monthly average) as the operating constraint for the entire month. The other option that was explored was to smooth the field data with a moving average over a window of three months. The simulation results between these two options showed some differences. Overall, the simulation results for the case with the constraint of a moving average appear to be smoother, with fewer fluctuations. The development of the wormhole network in the two cases was very similar. A reasonable match to sand production was achieved in both cases, together with a reasonable representation of the trends in BHP and producing GOR. Water production was matched well during the initial period of CHOPS, but not as well subsequently. This has also been the case for other studies (e.g., Istchenko and Gates,

2012), and is likely caused by the presence of higher water saturation in regions relatively far from the well.

The sensitivity tests of domain size suggest that a smaller domain was enough to represent the drainage area for the current CHOPS well. The simulation results for multiple layers containing wormhole networks indicate that a single-layered system is likely sufficient for representing the impact of the wormhole network on simulated production behaviour.

Aiming to further investigate the robustness of the improved CHOPS model for simulating a variety of production and flow behaviours associated with CHOPS wells, three CHOPS wells with different production profiles were selected to demonstrate how the refined model in this study can be used to simulate production behaviour from other CHOPS wells with different production profiles. A time-dependent division factor was employed in the sand production model to offer additional flexibility in representing sand transport during different periods of CHOPS production. This factor can be used to tailor the rate of sand transport depending on the conditions in the wormhole network (i.e., the effective porosity and oil flow rate). The improved model in this study also allows for a broader set of realizations to be implemented as wormhole fractal patterns. Typically, denser fractal patterns are more suitable for cases with more sand and oil production. The simulated results showed that CHOPS wells with more oil and sand production could generate a more extensive wormhole network.

Post-CHOPS CSI simulations were performed for the three CHOPS wells simulated in Chapter 6. The initial conditions for the CSI simulations were determined by the simulated reservoir conditions at the end of CHOPS in each of these three wells. The solvent selected for the

CSI simulations was 100% CO_2. In the CSI simulations, the wormhole network was assumed to be stable; i.e., no sand production occurred during the CSI process.

Nonequilibrium processes play a critical role in the dissolution of CO_2 into the live heavy oil, and in the exsolution of CO_2 from the live heavy oil (i.e., via both bubble nucleation and coalescence). The reaction frequency factors (*rrf*s) control the nonequilibrium processes of solvent dissolution and exsolution. This determines the effectiveness of the solvent in mixing with the heavy oil during the injection period and developing foamy oil flow during the production period. The values of the frequency factor for CO_2 dissolution *rrf* (r_{CO2s}) and the values of the dispersion parameters for gas/oil mixing were used from the study by Chang and Ivory (2013). The exsolution *rrf* (for bubble nucleation) for CO_2 was higher in this study than the one in the study conducted by Chang and Ivory (2013). This decision was based on the viscosity of the dead oil in this study compared to the viscosity of the dead oil in the study by Chang and Ivory (2013); the oil viscosity was lower in this study, implying that bubble nucleation would occur more rapidly. Note that the nonequilibrium exsolution model used by Chang and Ivory (2013) did not include a reaction representing bubble coalescence.

In the base case, bubble coalescence during exsolution was slower, leading to a longer lifespan of dispersed bubbles. When bubble coalescence occurred more rapidly, oil production from CSI decreased significantly. This difference in oil production performance indicates that foamy oil flow, in the form of a longer lifespan of dispersed bubbles, is beneficial to oil recovery.

When the rate of CO_2 dissolution is faster, the penetration of CO_2 into the matrix beyond the wormhole network is reduced. Most of the injected CO_2 dissolves into the heavy oil that is in

the wormhole network. This results in a decrease in oil production, compared to the case when the rate of CO_2 dissolution is slower.

If the rate of bubble nucleation and coalescence is increased from the base case, oil production decreases. Similarly, if the rate of bubble nucleation and coalescence is reduced from the base case, oil production decreases. In both cases, the lifespan of dispersed bubbles is most likely somewhat shorter than in the base case. This provides additional support for the interpretation of the simulation results presented above that foamy oil flow (in the form of dispersed bubbles) is beneficial to oil production.

8.2 Contributions

The primary contributions of this thesis are listed as follows:

(1) The CHOPS model developed by Yu and Leung (2020) was extended to better capture the broad range of production behaviour observed in CHOPS wells. For example, the sand production model was adjusted to capture the characteristics typical of sand production from CHOPS wells: i.e., a rapid increase in the rate of sand production to a peak, and subsequent decline to a low but persistent level. Similarly, the foamy oil model was refined in order to capture the characteristics typical of gas production from CHOPS wells: a period of relatively low but constant producing GOR followed by a sharp increase in producing GOR as a well ages. These modifications to the CHOPS model developed by Yu and Leung (2020) was to better represent the reservoir conditions at the end of CHOPS. This improvement facilitates the modelling of initial conditions for simulations of a post-CHOPS process, particularly cyclic solvent processes.

(2) Specifically, the simulations by Yu and Leung (2020) did not capture the rate of sand production adequately. The simulated peak rate was too high, and the following simulated decline in sand production was too rapid. In this study, the sand production model was adjusted to match the entire period of sand production much better.

(3) Further, the simulations by Yu and Leung (2020) did not capture the behaviour of producing GOR adequately. The simulated producing GOR did not increase rapidly as the CHOPS well aged. In this study, the foamy oil model was refined to match the trend in the entire period of gas production much better.

(4) Some aspects of the representation of wormhole layers in the model by Yu and Leung (2020) were reviewed and revised. The representation of wormholes confined to a horizontal layer was retained. However, the effect of multiple layers containing a wormhole network on production performance was investigated. It was found that simulated production was not very sensitive to whether wormholes were represented by a single layer or several layers.

(5) The robustness of the improved CHOPS model for simulating a variety of production and flow behaviours associated with CHOPS wells was investigated. Three CHOPS wells with different production profiles were selected to demonstrate how the modified model in this study can be used to simulate production behaviour from CHOPS wells with different production profiles. It was found that one of the factors necessary to simulate different production profiles was to introduce customized wormhole fractal patterns for different wells. The improved model in this study allowed for a broader set of realizations to be implemented as wormhole fractal patterns. Typically, denser fractal patterns were more suitable for cases with more sand and oil production. The results of the simulations showed that CHOPS wells with more oil and sand production could generate more extensive wormhole networks.

(6) In this study, simulations of a CO_2-based CSI process were performed as a follow-up to CHOPS. The simulations explored various mechanisms involved in the dissolution of CO_2 into heavy oil during injection and exsolution of CO_2 from heavy oil during production. In particular, these simulations focused on the nonequilibrium aspects of CO_2 dissolution and exsolution. The simulation results indicated that foamy oil flow (in the form of dispersed bubbles) is beneficial to oil production.

8.3 Limitations and Recommendations for Future Work

(1) The model treats the reservoir as homogeneous. The impact of reservoir heterogeneity should be investigated.

(2) A better understanding of the relationship between the production behaviour in CHOPS wells and the structure of the wormhole network (i.e., the rate of advancement and network density) should be developed.

(3) The ability of the CHOPS model presented in this study to represent an even wider range of production behaviour from CHOPS wells should be examined, and if necessary, further refinements to the sand production model and the foamy oil model should be introduced.

(4) The impact of other solvents or solvent mixtures on CSI processes should be investigated. Among other things, this would require appropriate modifications to the pseudo kinetic models for solvent dissolution and exsolution. The mutual interference between solvents should also be taken into account. The purpose of simulating the performance of other solvents would be to explore whether they could offer a better performance than CO_2 does.

BIBLIOGRAPHY

Adams, D.M. 1982. Experiences with Waterflooding Lloydminster Heavy-Oil Reservoirs. *J Pet Technol.* 34 (08): 1643–1650. SPE-10196-PA. https://doi.org/10.2118/10196-PA.

Alshmakhy, A., and Maini, B. B. 2012. Effects of Gravity, Foaminess, and Pressure Drawdown on Primary-Depletion Recovery Factor in Heavy-Oil Systems. *J Can Pet Technol* 51 (6): 449–456. SPE-163067-PA. https://doi.org/10.2118/163067-PA.

Bamzad, S., Abdi, M., BinDahbag, M. et al. 2023. Experimental Measurement and Thermodynamic Modeling of Vapor–Liquid Equilibrium Data of C1/Bitumen, CO_2/Bitumen, C1/CO_2/Bitumen, C1/Diluent/Bitumen, and C1/CO_2/Diluent/Bitumen Systems. *Ind. Eng. Chem. Res*. 62 (3): 1571–1595. https://doi.org/10.1021/acs.iecr.2c02010.

Bjorndalen, N., Jiang, H., and Jossy, E. 2023. Solvent Gas Uptake of CO_2 and Propane in Heavy Oil for Enhanced Oil Recovery. Paper presented at the SPE Canadian Energy Technology Conference and Exhibition, Calgary, Alberta, Canada, 10 March. SPE-212777-MS. https://doi.org/10.2118/212777-MS.

Bjorndalen, N., Jossy, E., and Alvarez, J. 2012. Foamy Oil Behaviour in Solvent Based Production Processes. Paper presented at the SPE Heavy Oil Conference Canada, Calgary, Alberta, Canada, 12–14 June. SPE-157905-MS. https://doi.org/10.2118/157905-MS.

Bowers, B., and Drummond, K. J. 1997. Drummond. Conventional Crude Oil Resources of the Western Canada Sedimentary Basin. *J Can Pet Technol* 36 (02). PETSOC-97-02-05. https://doi.org/10.2118/97-02-05.

Bratli, R. K. and Risnes, R. 1981. Stability and Failure of Sand Arches. *SPE J.* 21 (2): 236–248. SPE-8427-PA. https://doi.org/10.2118/8427-PA.

Bryan, J., Butron, J., Nickel, E. et al. 2018. Measurement of Non-Equilibrium Solvent Release from Heavy Oil during Pressure Depletion. Paper presented at the SPE Canada Heavy Oil Technical Conference, Calgary, Alberta, Canada, 13–14 March. SPE-189729-MS. https://doi.org/10.2118/189729-MS.

Busahmin, B., Maini, B., Karri, R. R. et al. 2017. Studies on The Stability of The Foamy Oil in Developing Heavy Oil Reservoirs. *Defect and Diffusion Forum*. 371: 111-116. https://doi.org/10.4028/www.scientific.net/DDF.371.111.

Chang, J., and Ivory, J. 2013. Field-Scale Simulation of Cyclic Solvent Injection (CSI). *J Can Pet Technol.* 52 (04): 251–265. SPE-157804-PA. https://doi.org/10.2118/157804-PA.

Chang, J., and Ivory, J. 2015. History Match and Strategy Evaluation for CSI Pilot. Paper presented at the SPE Canada Heavy Oil Technical Conference, Calgary, Alberta, Canada, 9 June. SPE-174467-MS. https://doi.org/10.2118/174467-MS.

Chang, J., Ivory, J., and London, M. 2015. History Matches and Interpretation of CHOPS Performance for CSI Field Pilot. Paper presented at the SPE Canada Heavy Oil Technical Conference, Calgary, Alberta, Canada, 9–11 June. SPE-174466-MS. https://doi.org/10.2118/174466-MS.

Chang, Y. B., Coats, B. K., and Nolen, J. S. 1996. A Compositional Model for CO_2 Floods Including CO_2 Solubility in Water. Paper presented at the Permian Basin Oil and Gas Recovery Conference, Midland, Texas, 27 March. SPE-35164-MS. https://doi.org/10.2118/35164-MS.

Chen, J. Z. and Maini, B. 2005. Numerical Simulation of Foamy Oil Depletion Tests. Paper presented at the Canadian International Petroleum Conference, Calgary, Alberta, Canada, 7–9 June. PETSOC-2005-073. https://doi.org/10.2118/2005-073.

Chen, T., and Leung, J. Y. 2021. Numerical Simulation of Nonequilibrium Foamy Oil for Cyclic Solvent Injection in Reservoirs after Cold Heavy Oil Production with Sand. *SPE Res Eval & Eng*. 24 : 675–691. SPE-205504-PA. https ://doi.org/10.2118/205504-PA.

Chen, T., Leung, J. Y., Bryan, J. et al. 2020. Analysis of Non-Equilibrium Foamy Oil Flow in Cyclic Solvent Injection Processes. *J Pet Sci Eng*. 195: 107857. https://doi.org/10.1016/j.petrol.2020.107857.

Coskuner, G., and Huang, H. 2020a. Enhanced Oil Recovery in Post-CHOPS Cold Heavy Oil Production with Sand Heavy Oil Reservoirs of Alberta and Saskatchewan Part 1: Field Piloting of Mild Heating Technologies. Paper presented at the SPE Canada Heavy Oil Conference, Virtual, 24 September. SPE-199964-MS. https://doi.org/10.2118/199964-MS.

Coskuner, G., and Huang, H. 2020b. Enhanced Oil Recovery in Post-CHOPS Cold Heavy Oil Production with Sand Heavy Oil Reservoirs of Alberta and Saskatchewan Part 2: Field Piloting of Cycling Solvent Injection. Paper presented at the SPE Canada Heavy Oil Conference, Virtual, 24 September. SPE-199947-MS. https://doi.org/10.2118/199947-MS.

Coskuner, G., Khosrow, N., and Babadagli, T. 2013. An Enhanced Oil Recovery Technology as a Follow Up to Cold Heavy Oil Production with Sand. Paper presented at the SPE Heavy Oil Conference-Canada, Calgary, Alberta, Canada, 11 June. SPE-165385-MS. https://doi.org/10.2118/165385-MS.

Coskuner, G., Khosrow, N., and Babadagli, T. 2015. An Enhanced Oil Recovery Technology as a Follow Up to Cold Heavy Oil Production with Sand. *J Pet Sci Eng*. 133: 475–482. https://doi.org/10.1016/j.petrol.2015.06.030.

Dong, M., Huang, S., and Hutchence, K. 2006. Methane Pressure-Cycling Process with Horizontal Wells for Thin Heavy-Oil Reservoirs. *SPE Res Eval & Eng*. 9 (2): 154–164. SPE-88500-PA. https://doi.org/10.2118/88500-PA.

Dusseault, M. B. 2001. Comparing Venezuelan and Canadian Heavy Oil and Tar Sands. Paper presented at the Canadian International Petroleum Conference, Calgary, Alberta, 12 June. PETSOC-2001-061. https://doi.org/10.2118/2001-061.

Dusseault, M. B. 2006. Sequencing Technologies to Maximize Recovery. Paper presented at the Canadian International Petroleum Conference, Calgary, Alberta, 13 June. PETSOC-2006-135. https://doi.org/10.2118/2006-135.

Dusseault, M. B. and El-Sayed, S. 2000. Heavy-Oil Production Enhancement by Encouraging Sand Production. Paper presented at the SPE/DOE Improved Oil Recovery Symposium, Tulsa, Oklahoma, USA, 3–5 April. SPE-59276-MS. https ://doi.org/10.2118/59276-MS.

Dusseault, M. B., Liang, C. X., Ma, Y., Gu, W., and Xu, B. 2002. CHOPS in Jilin Province, China. Paper presented at the SPE International Thermal Operations and Heavy Oil Symposium and International Horizontal Well Technology Conference, Calgary, Alberta, Canada, 4 November. SPE-79032-MS. https://doi.org/10.2118/79032-MS.

Falconer, K. 2004. Fractal Geometry: Mathematical Foundations and Applications. *John Wiley & Sons*.

Fan, Z. and Yang D. 2016. Characterization of Wormhole Growth and Its Applications for CHOPS Wells Using History Matching. Paper presented at the SPE Improved Oil Recovery Conference, Tulsa, Oklahoma, USA, 11–13 April. SPE-179617-MS. https://doi.org/10.2118/179617-MS.

Fan, Z., Yang, D., and Li, X. 2019. Quantification of Sand Production Using a Pressure-Gradient-Based Sand-Failure Criterion. *SPE J.* 24 (3) : 988–1001. SPE-185009-PA. https ://doi.org/10.2118/185009-PA.

Fernández-Martínez, M. 2016. A survey on fractal dimension for fractal structures. *Applied Mathematics and Nonlinear Sciences*. 1 (2): 437-472. eISSN: 2444-8656. https://doi.org/10.21042/AMNS.2016.2.00037.

Freitag, N. P. 2018. Similarity of the Effect of Different Dissolved Gases on Heavy-Oil Viscosity. *SPE Res Eval & Eng*. 21 (03): 747-756. SPE-189456-PA. https://doi.org/10.2118/189456-PA.

Fried, J. J., and Combarnous, M. A. 1971. Dispersion in Porous Media. *Advances in Hydroscience*. 7, 169-282. https://doi.org/10.1016/B978-0-12-021807-3.50008-4.

Ganapathi, R., Henni, A., and Shirif, E. 2022. Solubility of carbon dioxide and ethane in Lloydminster heavy oil: Experimental study and modelling. *The Canadian Journal of Chemical Engineering*. 100 (6): 1235-1243. https://doi.org/10.1002/cjce.24327.

Geilikman, M. B. and Dusseault, M. B. 1997. Fluid Rate Enhancement from Massive Sand Production in Heavy-Oil Reservoirs. *J Pet Sci Eng*. 17 (1–2): 5–18. https://doi.org/10.1016/S0920-4105(96)00052-6.

Guo, B., Gao, D., Ai, C., and Qu, J. 2012. Critical Oil Rate and Well Productivity in Cold Production from Heavy-Oil Reservoirs. *SPE Prod & Oper*. 27 (01): 87-93. SPE-133172-PA. https://doi.org/10.2118/133172-PA.

Haddad, A. S., and Gates, I. 2015. Modelling of Cold Heavy Oil Production with Sand (CHOPS) Using a Fluidized Sand Algorithm. *Fuel*. 158: 937–947. https://doi.org/10.1016/j.fuel.2015.06.032.

Huang, W., Marcum, B., Chase, M. et al. 1998. Cold Production of Heavy Oil from Horizontal Wells in the Frog Lake Field. *SPE J.* 6 (1): 551–555. SPE-52636-PA. https://doi.org/10.2118/52636-PA.

Husky Energy. 2011. Husky Oil's Mervin Cold Solvent EOR Pilot. Final Technical report for the SPRI Program. Saskatchewan Petroleum Research Incentive, Regina, Saskatchewan, Canada, November.

Istchenko, C. M. and Gates, I. D. 2012. The Well-Wormhole Model of CHOPS: History Match and Validation. Paper presented at the SPE Heavy Oil Conference Canada, Calgary, Alberta, Canada, 12–14 June. SPE-157795-MS. https://doi.org/10.2118/157795-MS.

Istchenko, C. M. and Gates, I. D. 2014. Well/Wormhole Model of Cold Heavy-Oil Production with Sand. *SPE J.* 19 (2): 260–269. SPE-150633-PA. https://doi.org/10.2118/150633-PA.

Ivory, J., Chang, J., Coates, R. et al. 2010. Investigation of Cyclic Solvent Injection Process for Heavy Oil Recovery. *J Can Pet Technol.* 49 (9): 22–33. SPE-140662-PA. https://doi.org/10.2118/140662-PA.

Jamaloei, B.Y., Dong, M., Mahinpey, N. et al. 2012. Enhanced Cyclic Solvent Process (ECSP) for Heavy Oil and Bitumen Recovery in Thin Reservoirs. *Energy Fuels*. 26 (5): 2865–2874. https://doi.org/10.1021/ef300152b.

Jiang, T., Jia, X., Zeng, F. et al. 2013. A Novel Solvent Injection Technique for Enhanced Heavy Oil Recovery: Cyclic Production with Continuous Solvent Injection. Paper presented at the SPE Heavy Oil Conference-Canada, Calgary, Alberta, Canada, 11 June. SPE-165455-MS. https://doi.org/10.2118/165455-MS.

Kumar, R., Pooladi-Darvish, M., and Okazawa, T. 2002. Effect of Depletion Rate on Gas Mobility and Solution Gas Drive in Heavy Oil. *SPE J.* 7(02): 213-220. SPE-78438-PA. https://doi.org/10.2118/78438-PA.

Lebel, P. 1994. Performance Implications of Various Reservoir Access Geometries. Paper presented at the 11th Annual Heavy Oil and Oil Sands Technical Symposium, Calgary, Alberta, Canada, 2 March.

Lillico, D. A., Babchin, A. J., Jossy, W. E. et al. 2001. Gas Bubble Nucleation Kinetics in a Live Heavy Oil. *Colloids Surf A*. 192 (1–3): 25–38. https://doi.org/10.1016/S0927-7757(01)00714-2.

Lim, G. B., Kry, R. P., Harker, B. C. et al. 1996. Three-dimensional Scaled Physical Modeling of Solvent Vapour Extraction of Cold Lake Bitumen. *J Can Pet Technol*. 35 (4): 32–40. PETSOC-96-04-03. https://doi.org/10.2118/96-04-03.

Liu, P., Li, W., Hao, M. et al. 2016. Quantitative Evaluation of Factors Affecting Foamy Oil Recovery in the Development of Heavy Hydrocarbon Reservoirs. *Int J Hydrogen Energy*. 41 (35): 15624–15631. https://doi.org/10.1016/j.ijhydene.2016.04.031.

Liu, X. and Zhao, G. 2005. A Fractal Wormhole Model for Cold Heavy Oil Production. *J Can Pet Technol*. 44 (9): 31–36. PETSOC-05-09-03. https://doi.org/10.2118/05-09-03.

Loughead, D. J. and Saltuklaroglu, M. 1992. Lloydminster Heavy Oil Production: Why So Unusual? Paper presented at the 9th Annual Heavy Oil and Oil Sands Technology Symposium, Calgary, Alberta, Canada, 11 March.

Ma, H., Huang, D., Yu, G., She, Y., and Gu, Y. 2017. Combined Cyclic Solvent Injection and Waterflooding in the Post-Cold Heavy Oil Production with Sand Reservoirs. *Energy Fuels*. 31 (1): 418-428. https://doi.org/10.1021/acs.energyfuels.6b02596.

Maini, B. B. 1996. Foamy Oil Flow in Heavy Oil Production. *J Can Pet Technol*. 35 (6). PETSOC-96-06-01. https://doi.org/10.2118/96-06-01.

Maini, B. B. 1999. Laboratory Evaluation of Solution Gas Drive Recovery Factors in Foamy Heavy Oil Reservoirs. Paper presented at the Annual Technical Meeting, Calgary, Alberta, Canada, 14–18 June. PETSOC99-44. http://dx.doi.org/10.2118/99-44.

Maini, B. B. 2001. Foamy-Oil Flow. *J Pet Technol*. 53 (10): 54–64. SPE-68885-JPT. https://doi.org/10.2118/68885-JPT.

Maini, B. B., Sarma, H. K., and George, A. E. 1993. Significance of Foamy Oil Behaviour in Primary Production of Heavy Oils. *J Can Pet Technol*. 32 (9): 50–54. PETSOC-93-09-07. https://doi.org/10.2118/93-09-07.

Martinez Gamboa, J. J., and Leung, J. Y. 2019. Design of Field - Scale Cyclic Solvent Injection Processes for Post - CHOPS Applications. *The Canadian Journal of Chemical Engineering*. 97 (1): 123-132. https://doi.org/10.1002/cjce.23261.

McCaffrey, W. J. and Bowman, R. D. 1991. Recent Successes in Primary Bitumen Production. Paper presented at the 8th Annual Heavy Oil and Oil Sands Technical Symposium, Calgary, Alberta, Canada, 14 March.

Meza-Díaz, B., Sawatzky, R., and Kuru, E. 2012. Sand on Demand: A Laboratory Investigation on Improving Productivity in Horizontal Wells Under Heavy-Oil Primary Production—Part II. *SPE J.* 17 (04): 1012-1028. SPE-133500-PA. https://doi.org/10.2118/133500-PA.

Meza-Díaz, B., Sawatzky, R., Kuru, E., and Oldakowski, K. 2011. Sand on Demand: A Laboratory Investigation on Improving Productivity in Horizontal Wells Under Heavy-Oil Primary Production. *SPE Prod & Oper*. 26 (03): 240-252. SPE-115625-PA. https://doi.org/10.2118/115625-PA.

Okazawa, T. 2009. Impact of Concentration-Dependence of Diffusion Coefficient on VAPEX Drainage Rates. *J Can Pet Technol*. 48 (02): 47-53. PETSOC-09-02-47. https://doi.org/10.2118/09-02-47.

Oldakowski, K., and Sawatzky, R. P. 2018. Wormhole Stability Under Post Chops Conditions. Paper presented at the SPE Canada Heavy Oil Technical Conference, Calgary, Alberta, Canada, 13 March. SPE-189749-MS. https ://doi.org/10.2118/189749-MS.

Or, C., Sasaki, Y., Sugai, Y. et al. 2014. Numerical Simulation of CO_2 Gas Microbubble of Foamy Oil. *Energy Procedia*. 63 (2014): 7821–7829. https://doi.org/10.1016/j.egypro.2014.11.816.

Palmer, I. D., McLennan, J. D., and Vaziri, H. H. 2000. Cavity-Like Completions in Weak Sands. Paper presented at the SPE International Symposium on Formation Damage Control, Lafayette, Louisiana, 23 February. SPE-58719-MS. https://doi.org/10.2118/58719-MS.

Peters, E. J. 2012. Advanced Petrophysics Volume 2: Dispersion, Interfacial Phenomena/Wettability, Capillarity/Capillary Pressure, Relative Permeability. *Greenleaf Book Group*. ISBN 978-1-936909-46-9.

Qin, W. and Wojtanowicz, A. K. 2009. Water Problems and Control Techniques in Heavy Oils with Bottom Aquifers. Paper presented at the SPE Americas E&P Environmental and Safety Conference, San Antonio, Texas, 23 March. SPE-125414-MS. https://doi.org/10.2118/125414-MS.

Quail, B., Hill, G. A., and Jha, K. N. 1988. Correlations of viscosity, gas solubility, and density for Saskatchewan heavy oils. *Industrial & engineering chemistry research*. 27 (3): 519-523.

Rangriz Shokri, A., and Babadagli, T. 2012a. Evaluation of Thermal/Solvent Applications with and without Cold Heavy Oil Production with Sand (CHOPS). Paper presented at the SPETT 2012 Energy Conference and Exhibition, Port-of-Spain, Trinidad, 11–13 June. SPE-158934-MS. https://doi.org/10.2118/158934-MS.

Rangriz Shokri, A. and Babadagli, T. 2012b. An Approach to Model CHOPS (Cold Heavy Oil Production with Sand) and Post-CHOPS Applications. Paper presented at the SPE Annual Technical Conference and Exhibition, San Antonio, Texas, USA, 8–10 October. SPE-159437-MS. https://doi.org/10.2118/159437-MS.

Riazi, N., Lines, L., and Russell, B. 2014. Cold Heavy Oil Reservoir Characterization by Time-Lapse Seismic Inversion, a Case Study. Paper presented at the SPE Heavy Oil Conference-Canada, Calgary, Alberta, Canada, 10 June. SPE-170127-MS. https://doi.org/10.2118/170127-MS.

Riazi, N., Lines, L., and Russell, B. 2014. Cold heavy oil reservoir characterization by time-lapse seismic inversion, a case study. Paper presented at the SPE Heavy Oil Conference-Canada, Calgary, Alberta, Canada, 10 June. SPE-170127-MS. https ://doi.org/10.2118/170127-MS.

Rivero, J. A., Coskuner, G., Asghari, K. et al. 2010. Modeling CHOPS Using a Coupled Flow-Geomechanics Simulator With Nonequilibrium Foamy-Oil Reactions: A Multiwell History Matching Study. Paper presented at the SPE Annual Technical Conference and Exhibition, Florence, Italy, 19–22 September. SPE-135490-MS. https://doi.org/10.2118/135490-MS.

Sander, L. M. 1986. Fractal Growth Processes. *Nature*. 322: 789-793. https://doi.org/10.1038/322789a0.

Sawatzky, R. P., Lillico, D. A., London, M. J. et al. 2002. Tracking Cold Production Footprints. Paper presented at the Canadian International Petroleum Conference, Calgary, Alberta, Canada, 11–13 June. PETSOC-2002-086. https://doi.org/10.2118/2002-086.

Shafiei, A., and Dusseault, M. B. 2013. Geomechanics of Thermal Viscous Oil Production in Sandstones. *J Pet Sci Eng*. 103: 121-139. https://doi.org/10.1016/j.petrol.2013.02.001.

Shelberg, M.C., Lam, N., and Moellering, H. 1983. Measuring the Fractal Dimensions of Surfaces. Defense mapping agency aerospace center St Louis AFS MO.

Sheng, J. J., Maini, B. B., Hayes, R. E. et al. 1999. Critical Review of Foamy Oil Flow. *Transport in Porous Media*. 35: 157–187. https://doi.org/10.1023/A:1006575510872.

Shi, R., Schnitzler, J., and Kantzas, A. 2008. Preliminary Results of Enhanced Oil Recovery by CO_2 Cyclic Injection. Paper presented at the World Heavy Oil Congress, Edmonton, AB, Canada, 10-12 March.

Smith, G. E. 1988. Fluid Flow and Sand Production in Heavy-Oil Reservoirs Under Solution-Gas Drive. *SPE Prod Eng*. 3 (2): 169–180. SPE-15094-PA. https://doi.org/10.2118/15094-PA.

Squires, A. 1993. Inter-well tracer results and gel blocking program. Paper presented at the 10th Annual Heavy Oil and Oil Sands Technical Symposium, Calgary, Alberta, Canada, 9 March.

Stanley, H. E. 1986. Form: An Introduction to Self-Similarity and Fractal Behaviour. *On growth and form: fractal and non-fractal patterns in physics*. 21-53.

Tharanivasan, A. K., Yang, C., and Gu, Y. 2006. Measurements of Molecular Diffusion Coefficients of Carbon Dioxide, Methane, and Propane in Heavy Oil under Reservoir Conditions. *Energy Fuels*. 20 (6): 2509-2517. https://doi.org/10.1021/ef060080d.

Tremblay, B. 2005. Modelling of Sand Transport Through Wormholes. *J Can Pet Technol*. 44 (4): 51–58. PETSOC-05-04-06. https://doi.org/10.2118/05-04-06.

Tremblay, B. and Oldakowski, K. 2003. Modeling of Wormhole Growth in Cold Production. *Transp Porous Med*. 53: 197–214. https://doi.org/10.1023/A:1024017622009.

Tremblay, B., and Oldakowski, K. 2002. Wormhole Growth and Interaction in a Large Sand Pack. *J Pet Sci Eng*. 34 (1–4): 13–34. ISSN 0920-4105. https://doi.org/10.1016/S0920-4105(02)00150-X.

Tremblay, B., Sedgwick, G., and Forshner, K. 1997. Simulation of Cold Production of Heavy Oil Reservoirs: Wormhole Dynamics. *SPE Res Eng*. 12 (2): 110–117. SPE-35387-PA. https://doi.org/10.2118/35387-PA.

Tremblay, B., Sedgwick, G., and Forshner, K. 1998. Modelling of Sand Production from Wells on Primary Recovery. *J Can Pet Technol*. 37 (3): 41–50. PETSOC-98-03-03. https://doi.org/10.2118/98-03-03.

Tremblay, B., Sedgwick, G., and Vu, D. 1999. A Review of Cold Production in Heavy Oil Reservoirs. Paper presented at the EAGE – 10th European Symposium on Improved Oil Recovery, Brighton, UK, 18-20 August.

Uddin, M. 2005. Numerical Studies of Gas Exsolution in a Live Heavy Oil Reservoir. Paper presented at the SPE International Thermal Operations and Heavy Oil Symposium, Calgary, Alberta, Canada, 1–3 November. SPE-97739-MS. https://doi.org/10.2118/97739-MS.

Walin, C., Dusseault, M. B., Hayes, K., and Kremer, M. 2000. Approaches to Cold Heavy Oil Production Workover Practices and Strategies. Paper presented at the Canadian International Petroleum Conference, Calgary, Alberta, 4 June. PETSOC-2000-069. https://doi.org/10.2118/2000-069.

Wang, H., Torabi, F., and Zeng, F. 2023. Investigation of Non-Equilibrium Solvent Exsolution Dynamics and Bubble Formation and Growth of a CO2/C3H8/Heavy-Oil System by Micro-Optical Visualizations: Experimental and Continuum-Scale Numerical Studies. *Fuel*. 332: 126188. https://doi.org/10.1016/j.fuel.2022.126188.

Wang, H., Torabi, F., Zeng, F. et al. 2020. Experimental and Numerical Study of Non-Equilibrium Dissolution and Exsolution Behavior of CO_2 in a Heavy Oil System Utilizing Hele-Shaw-like Visual Cell. *Fuel.* 270: 117501. https://doi.org/10.1016/j.fuel.2020.117501.

Wang, H., Torabi, F., Zeng, F. et al. 2022. Experimental and Numerical Studies on Non-Equilibrium Gaseous Solvent Dissolution in Heavy Oil: A Continuum-Scale Approach Based on Bubble-Scale Dissolution Behaviors. *Fuel.* 307: 121851. https://doi.org/10.1016/j.fuel.2021.121851.

Wang, X., Zou, H., Li, G., Nie, C., and Chen, J. 2005. Integrated Well Completion Strategies with CHOPS to Enhance Heavy Oil Production: A Case Study in Fula Oil Field. Paper presented at the SPE International Thermal Operations and Heavy Oil Symposium, Calgary, Alberta, Canada, 1 November. SPE-97885-MS. https://doi.org/10.2118/97885-MS.

Wong, F. Y. F., Anderson, D. B., O'Rourke, J. C. et al. 2001. Meeting the Challenge to Extend Success at the Pikes Peak Steam Project to Areas with Bottom Water. Paper presented at the SPE Annual Technical Conference and Exhibition, New Orleans, Louisiana, 30 September. SPE-71630-MS. https://doi.org/10.2118/71630-MS.

Wong, F. Y., Neda, J. E., Sawatzky, R. P. et al. 2005. A Mechanistic Simulation Analysis of Cold Production Field Performance. Paper presented at the Canadian International Petroleum Conference, Calgary, 7 June.

Wong, R.C.K., Samieh, A.M., and Kuhlmeyer, R.L. 1994. Oil Sand Strength Parameters at Low Effective Stress: Its Effects on Sand Production. *J Can Pet Technol.* 33 (5): 44–49. PETSOC-94-05-04. https://doi.org/10.2118/94-05-04.

Xu, T., Moore, I. D., and Gallant, J. C. 1993. Fractals, Fractal Dimensions and Landscapes—a Review. *Geomorphology*. 8 (4): 245-262. https://doi.org/10.1016/0169-555X(93)90022-T.

Yeung, K. C. 1995. Cold Flow Production of Crude Bitumen at the Burnt Lake Project, Northeastern Alberta. Paper presented at the 6th UNITAR International Conference on Heavy Crude and Tar Sands, Houston, Texas, USA, 12–17 February. CONF-9502114-Vol.1. https://www.osti.gov/biblio/269562.

Young, L. C., and Stephenson, R. E. 1983. A Generalized Compositional Approach for Reservoir Simulation. *SPE J.* 23 (05): 727-742. SPE-10516-PA. https://doi.org/10.2118/10516-PA.

Yrigoyen, A., and Carvajal, G. 2001. Performance of a Foamy Oil Reservoir in Pseudo-Undersaturated State with Associated Aquifer. Paper presented at the SPE Latin American and Caribbean Petroleum Engineering Conference, Buenos Aires, Argentina, 25–28 March. SPE-69508-MS. http://dx.doi.org/10.2118/69508-MS.

Yu, H. and Leung, J. Y. 2020. A Sand-Arch Stability Constrained Dynamic Fractal Wormhole Growth Model for Simulating Cold Heavy-Oil Production with Sand. *SPE J.* 25 (06): 3440–3456. SPE-193893-PA. https://doi.org/10.2118/193893-PA.

Yuan, J. Y., Tremblay, B., and Babchin, A. 1999. A Wormhole Network Model of Cold Production in Heavy Oil. Paper presented at the International Thermal Operations/Heavy Oil Symposium, Bakersfield, California, 17 March. SPE-54097-MS. https ://doi.org/10.2118/54097-MS.

Zhou, X., Yuan, Q., Peng, X. et al. 2018. A Critical Review of the CO_2 Huff-N-Puff Process for Enhanced Heavy Oil Recovery. *Fuel*. 215: 813–824. https://doi.org/10.1016/j.fuel.2017.11.092.

Zhou, X., Yuan, Q., Rui, Z. et al. 2019. Feasibility Study of CO2 Huff 'n' puff Process to Enhance Heavy Oil Recovery via Long Core Experiments. *Applied Energy*. 236: 526-539. https://doi.org/10.1016/j.apenergy.2018.12.007.